In-Situ Monitoring and Simulations of the Non-Isothermal Crystallization of FFF Printed Materials

By

David Anderegg

Thesis submitted to the Faculty of
Virginia Polytechnic Institute and State University
in partial fulfillment of the requirements for the degree of

MASTERS OF SCIENCE

In

Materials Science and Engineering

Michael J. Bortner, Chairman
Steven H. McKnight
Steve M. Martin

November 16, 2018
Blacksburg, VA

Keywords: Additive manufacturing, in-situ, temperature, pressure, extrusion semi-crystalline, non-isothermal crystallization, healing

In-Situ Monitoring and Simulations of the Non-Isothermal Crystallization of FFF Printed Materials

David Anderegg

(ABSTRACT)

This thesis is concerned with the development of methods and models to aid in optimization and development of new materials for Fused Filament Fabrication (FFF). We demonstrate a novel FFF nozzle design to enable the first measurements of in-situ rheology inside FFF nozzles, which is critical for part performance by ensuring that the polymer extrudate is flowing at an appropriate temperature and flow rate during the part build process. Testing was performed using Acrylonitrile butadiene styrene filament and a modified Monoprice Maker Select 3D printer. Tests using the default temperature control settings of the printer showed an 11 °C drop in temperature and significant fluctuations in pressure, during printing and while idle, of ± 2 °C and +/-14 kPa. These deviations were eliminated at lower flow rates with a properly calibrated proportional–integral–derivative (PID) system. At high flow rates, drops in temperature as high as 6.5 °C were observed even with a properly calibrated PID, providing critical input to the impact of flow rate and PID calibration on polymer melt temperature inside FFF nozzles. Pressure readings ranging from 140-6900 kPa were measured over the range of filament feed rates and corresponding extrusion flow rates. Theoretical predictions of pressure profiles, assuming a power-law fluid model, matched well with experimental results. Our nozzle prototype succeeded in measuring internal conditions of FFF nozzles for the first time, thereby providing several important insights into the printing process which are vital for monitoring and improving FFF printed parts.

Furthermore, finite difference simulations based on first principles analysis are presented which are capable of quantifying the effect of processing conditions on the properties of semi-crystalline parts made by FFF. Each layer was modelled as a rectangular cross section which was

broken down into smaller elements for modelling. Crystallinity of each element was calculated using a parallel Avrami model which accounts for changes in crystallization rate due to temperature and multiple crystallization mechanisms. The amount of polymer diffusion, also referred to as the degree of healing, was calculated using a novel incremental diffusion model which accounted for not only changes in reptation time due to temperature but also restrictions to healing due to crystallinity. To the authors knowledge, this is the first healing model capable of accounting for the effect of crystallinity on healing and is relevant to any process involving healing of crystalline interfaces; not just FFF. Cumulative shear stresses between each layer and at the bottom of the part were also calculated for the first time using a force balance model by assuming constant shear strain throughout each layer. Simulations were performed using typical printing conditions for polyether ether ketone. In the first layer of a 24 layer part, the average degree of crystallinity, healing, and shear stress were 25.0%, 53.8% and 19.4 MPa respectively. The degree of crystallinity and healing at layer 22 (which represented the steady state values) were 18.4-25.0% and 51.4% respectively. When crystallinity was not accounted for, varying the printing parameters and material properties supported the use of high temperatures and specific heat in addition to a low printing speed, heat transfer coefficient, and thermal conductivity to maximize part properties. These conditions also supported crystallization, however, which led to a simultaneous reduction in the part properties when crystallinity was taken into account. These contradictory effects will need to be considered when optimizing the printing parameters, though the optimal balance will be highly dependent on the material used and the limitations of the printer.

Experimental validation of the accuracy of the heat transfer and polymer diffusion models was performed using an amorphous polymer (polyether imide). Single road wide parts were printed at various nozzle temperatures, bed temperatures, and printing speeds and the results were compared to the simulated results. The predicted shear stress in the bottom of the part ranged from 2.3-3.8 MPa and correlated to warpages at the corners of each part of 1.2-2.4 mm. A linear increase in warpage with predicted shear stress was observed supporting the shear stress model. Predicted degrees of healing ranged from 2-90% but the experimental results ranged from 15-36%. Results of the healing model underpredicted strength at low printing speeds and over predicted strength at high printing speeds. The experimental validations showed the capabilities of the models, but the effect of printing speed will need to be investigated further to improve the accuracy of the healing model.

In-Situ Monitoring and Simulations of the Non-Isothermal Crystallization of FFF Printed Materials

David Anderegg

(GENERAL AUDIENCE ABSTRACT)

This thesis is concerned with the development of methods and models to aid in optimizing a type of 3D printing known as Fused Filament Fabrication (FFF). We demonstrate a novel FFF nozzle design to enable the first measurements of the temperature and pressure within FFF nozzles, which is critical for ensuring that the printer is printing at the appropriate temperature and flow rate. Testing was performed using a material known as Acrylonitrile butadiene styrene and a modified Monoprice Maker Select 3D printer. Tests using the default temperature control settings of the printer showed an 11 °C drop in temperature and significant fluctuations in pressure, during printing and while idle, of ± 2 °C and +/-14 kPa. These deviations were eliminated at lower flow rates with a properly calibrated temperature control system. At high flow rates, drops in temperature as high as 6.5 °C were observed even with a properly calibrated temperature control system, providing critical input to the impact of flow rate and temperature control calibration on the temperature of the polymer melt inside FFF nozzles. Pressure readings ranging from 140-6900 kPa were measured over the range of extrusion flow rates tested. Theoretical predictions of the pressure within the nozzles matched well with the experimental results. Our nozzle prototype succeeded in measuring internal conditions of FFF nozzles for the first time, thereby providing several important insights into the printing process which are vital for monitoring and improving FFF printed parts.

Furthermore, simulations of the FFF process are presented which can quantify the effect of processing conditions on the properties of FFF parts made from materials which can crystallize. Each layer was modelled as a rectangular cross section which was broken down into smaller

elements for modelling. Crystallinity of each element was calculated using a model which can account for changes in the rate of crystallization due to temperature as well as multiple types of crystallization. The strength of the interlayer bonds was calculated using a novel model which accounts for the effects of temperature and crystallinity. To the authors knowledge, this is the first bonding model capable of accounting for the effect of crystallinity on bonding and is relevant to any process involving bonding of crystalline materials; not just FFF. The shear stress between each layer and at the bottom of the part was also calculated for the first time by balancing thermal and shear stresses of each layer. Simulations were performed using typical printing conditions for a high performance polymer (polyether ether ketone). In the first layer of a 24 layer part, the average amount of crystallinity, bonding, and shear stress were 25.0%, 53.8% and 19.4 MPa respectively. The degree of crystallinity and healing at layer 22 (which represented the majority of the part) were 18.4-25.0% and 51.4% respectively. When crystallinity was not accounted for, varying the printing parameters and material properties supported the use of high temperatures and specific heat in addition to a low printing speed, heat transfer coefficient, and thermal conductivity to maximize part properties. These conditions also supported crystallization, however, which led to a simultaneous reduction in the part properties when crystallinity was considered. These contradictory effects will need to be considered when optimizing the printing parameters, though the optimal balance will be highly dependent on the material used and the limitations of the printer.

Experimental validation of the accuracy of the heat transfer and bonding models was performed using an amorphous polymer (polyether imide). Single road wide parts were printed at various nozzle temperatures, bed temperatures, and printing speeds and the results were compared to the simulated results. The predicted shear stress in the bottom of the part ranged from 2.3-3.8 MPa and correlated to the corners of each part peeling 1.2-2.4 mm from the printer. A linear increase in the experimental peeling with predicted shear stress was observed, supporting the shear stress model. Predicted bonding ranged from 2-90% of the strength of the material, but the experimental results ranged from 15-36%. Results of the bonding model underpredicted strength at low printing speeds and over predicted strength at high printing speeds. The experimental validations showed the capabilities of the models, but the effect of printing speed will need to be investigated further to improve the accuracy of the bonding model.

Acknowledgements

The author would like to acknowledge his mentor Dr. Michael J. Bortner for all his guidance over the years, both academic and professional. Additionally, he would like to recognize Dr. Mia Siochi, Dr. Kris Wise, and Chris Stelter for their considerable help with the experimental validation of my work. The author would also like to thank Dr. Steven McKnight and Dr. Steven Martin for serving on his research committee.

The author would like to further thank the following groups and individuals:

- First and foremost, God Almighty for his blessings of wisdom, knowledge, and the strength to persevere through the most troubling time.
- His friends and family in Chi Alpha for comfort over the years.
- The members of the Polymer Composite and Materials lab for all their extensive assistance and advice at every stage of the work. He would like to extend a special thanks to Jake Fallon, Eric Gilmer, and Cailean Pritchard.
- Members of the departmental staff who helped guide him through this process: Kim Grandstaff, Michelle Czamanske, and Christine B. Burgoyne.

Table of Contents

Chapter 1: Introduction 1

1.1 Introduction to FFF 1

1.2 Research Objectives 3

References 4

Chapter 2: Literature Review 6

2.1 Interlayer Mechanical Strength 6

2.2 Dimensional Tolerance, Warping and Residual Stress 12

2.3 Semi-Crystalline Polymers for FFF 16

2.4 Modelling Crystallization 18

2.5 Effect of Crystallinity on Healing 26

2.6 Temperature Measurements 27

2.7 Pressure Measurements and Theory 28

References 30

Chapter 3: In-Situ Monitoring of Polymer Flow Temperature and Pressure in Extrusion Based Additive Manufacturing 37

3.1 Experimental 38

3.1.1 Filament Characterization 38

3.1.2 Equipment Selection and Sensor Testing Procedure 38

3.1.3 Nozzle Design 40

3.2 Results and Discussion 40

3.2.1 Rheology Measurements ... 40

3.2.2 In-situ Temperature and Pressure Measurement of the Polymer Melt in the Nozzle ... 42

3.2.3 Comparison of Predicted vs. Measured Conditions for Modified Nozzle Configurations ... 44

3.3 Summary and Conclusions ... 48

References ... 49

Chapter 4: Simulations of the Non-Isothermal Crystallization, Polymer Diffusion and Heat Transfer of FFF Printed Materials, and the Effect on Part Properties ... 50

4.1 Models for Multiphysics Analysis ... 50

4.1.1 Heat Transfer ... 50

4.1.2 Crystallization ... 54

4.1.3 Degree of Healing ... 56

4.1.4 Stress Strain Behavior ... 58

4.2 Simulation Settings ... 62

4.2.1 Material and Process Parameters ... 62

4.2.2 Build Height Analysis ... 65

4.2.3 Analysis of Maximum Element Size and Time Step ... 68

4.3 Simulation Results for Typical Printing Parameters ... 69

4.3.1 Temperature Results ... 69

4.3.2 Crystallinity Results ... 73

4.3.3 Degree of Healing Results 75

4.3.4 Residual Stress Results 77

4.4 Sensitivity Analysis of Printing Parameters 79

4.4.1 Effect of Printing Parameters on Crystallinity 80

4.4.1 Effect of Printing Parameters on Degree of Healing 91

4.4.1 Effect of Printing Parameters on Residual Stress 96

4.5 Sensitivity Analysis of Material Properties 101

4.6 Summary and Conclusion 110

References 111

Chapter 5: Experimental Validation of FFF Models 113

5.1 Experimental Procedure 113

5.2 Experimental Determination of Model Parameters 114

5.3 Model Parameters 119

5.4 Results and Discussion 119

5.5 Summary and Conclusion 123

References 124

Chapter 6: Recommendations 125

Appendix 127

Appendix A: Nozzle Design 127

Appendix B: Nozzle Design Calculations 128

Appendix C: Two-dimensional Assumption Validation 130

Appendix D: Effect of Crystallinity on Interlayer Healing 131

Appendix E: Table of Experimental and Predicted Part Properties 133

References 134

List of Figures

Fig. 1.1: Diagram of the FFF process. 1

Fig. 3.1: Viscosity as a function of shear rate and temperature. 42

Fig. 3.2: Temperature and pressure measurements during printing and idle with two extrusion events using a poorly set deadtime temperature control system. 44

Fig. 3.3: Expanded view of idle conditions from Fig. 3.2, highlighting pressure fluctuations as the control system oscillates temperature. 44

Fig. 3.4: Pressure during extrusion at 230 °C. 46

Fig. 3.5: Difference between the minimum temperature during extrusion and the steady state temperature as a function of flow rate. 48

Fig. 4.1: Model of FFF cross section. 51

Fig. 4.2: Diagram of the cross section of a road used for stress analysis. 60

Fig. 4.3: Crystallization of ICI 450 PEEK at various cooling rates with best fit model. 65

Fig. 4.4: Locations tested within each road. 67

Fig. 4.5: Variation of crystallinity across layers at various locations within a road as described by Fig. 4.4. 67

Fig. 4.6: Variation in degree of healing across layers. 68

Fig. 4.7: Temperature vs time profile of layer 1 at various locations within a road as described by Fig. 4.4. 70

Fig. 4.8: Temperature vs time profile of layer 22 at various locations within a road as described by Fig. 4.4. 71

Fig. 4.9: Maximum temperature during extrusion of next layer vs layer at various locations within a road as described by Fig. 4.4. 72

Fig. 4.10: Minimum temperature during extrusion of layer vs layer at various locations within a road as described by Fig. 4.4. 73

Fig. 4.11: Crystallinity vs time profile of layer 1 at various locations within a road as described by Fig. 4.4. 74

Fig. 4.12: Crystallinity vs time profile of layer 22 at various locations within a road as described by Fig. 4.4. 75

Fig. 4.13: Degree of healing vs time profile of layers 1 and 22. 76

Fig. 4.14: Degree of healing vs time profile of layers 1 and 22 assuming no crystallization. 77

Fig. 4.15: Shear stress at the bottom of each layer after printing. 78

Fig. 4.16: Stress vs time profile of layer 1. 79

Fig. 4.17: Crystallinity throughout layer 1 as a function of heat transfer coefficient at various locations within a road as described by Fig. 4.4. 81

Fig. 4.18: Crystallinity throughout layer 1 as a function of environment temperature at various locations within a road as described by Fig. 4.4. 82

Fig. 4.19: Crystallinity throughout layer 1 as a function of bed temperature at various locations within a road as described by Fig. 4.4. 83

Fig. 4.20: Crystallinity throughout layer 1 as a function of deposition temperature at various locations within a road as described by Fig. 4.4. 84

Fig. 4.21: Crystallinity throughout layer 1 as a function of layer time at various locations within a road as described by Fig. 4.4. 85

Fig. 4.22: Crystallinity throughout layer 22 as a function of heat transfer coefficient at various locations within a road as described by Fig. 4.4. 87

Fig. 4.23: Crystallinity throughout layer 22 as a function of environment temperature at various locations within a road as described by Fig. 4.4. 88

Fig. 4.24: Crystallinity throughout layer 22 as a function of bed temperature at various locations within a road as described by Fig. 4.4. 89

Fig. 4.25: Crystallinity throughout layer 22 as a function of deposition temperature at various locations within a road as described by Fig. 4.4. 90

Fig. 4.26: Crystallinity throughout layer 22 as a function of layer time at various locations within a road as described by Fig. 4.4. 91

Fig. 4.27: Degree of healing of layers 1 and 22 as a function of heat transfer. 92

Fig. 4.28: Degree of healing of layers 1 and 22 as a function of environment temperature. 93

Fig. 4.29: Degree of healing of layers 1 and 22 as a function of bed temperature. 94

Fig. 4.30: Degree of healing of layers 1 and 22 as a function of deposition temperature. 95

Fig. 4.31: Degree of healing of layers 1 and 22 as a function of layer time. 96

Fig. 4.32: Shear stress at the bottom of layer 1 as a function of heat transfer coefficient. 97

Fig. 4.33: Shear stress at the bottom of layer 1 as a function of environment temperature. 98

Fig. 4.34: Shear stress at the bottom of layer 1 as a function of bed temperature. 99

Fig. 4.35: Shear stress at the bottom of layer 1 as a function of deposition temperature. 100

Fig. 4.36: Shear stress at the bottom of layer 1 as a function of layer time. 101

Fig. 4.37: Crystallinity throughout layer 1 as a function of thermal conductivity at various locations within a road as described by Fig. 4.4. 102

Fig. 4.38: Crystallinity throughout layer 1 as a function of specific heat at various locations within a road as described by Fig. 4.4. 103

Fig. 4.39: Crystallinity throughout layer 22 as a function of thermal conductivity at various locations within a road as described by Fig. 4.4. 104

Fig. 4.40: Crystallinity throughout layer 22 as a function of specific heat at various locations within a road as described by Fig. 4.4. 105

Fig. 4.41: Degree of healing of layers 1 and 22 as a function of thermal conductivity. 106

Fig. 4.42: Degree of healing of layers 1 and 22 as a function of specific heat. 107

Fig. 4.43: Shear stress at the bottom of layer 1 as a function of thermal conductivity. 108

Fig. 4.44: Shear stress at the bottom of layer 1 as a function of specific heat. 109

Fig. 4.45: Shear stress at the bottom of layer 1 as a function of G/E. 110

Fig. 5.1: Diagram of tear test samples. 114

Fig. 5.2: Average tear force of pressed films as a function of film thickness. 115

Fig. 5.3: SEM image of interlayer bond after tearing. 116

Fig. 5.4: Experimental setup for determination of environment temperature (A) and bed temperature (B) as a function of bed temperature. 117

Fig. 5.5: Experimental (solid orange) and theoretical (dashed blue) cooling assuming a heat transfer coefficient of 29 W/m^{2}K. 119

Fig. 5.6: Representative plot of trouser tear test results. 120

Fig. 5.7: Experimental versus predicted degree of healing. 122

Fig. 5.8: Average warpage at the corners of each part vs predicted shear stress at the bottom of layer 1. 123

List of Tables

Table 3.1: Pressure and flow rate results. 46

Table 4.1: Default printing parameters for PEEK simulations. 63

Table 4.2: PEEK properties. 63

Table 4.3: Crystalline properties of PEEK.. 64

Table 4.4: Variables and levels used to analyze sensitivity of model results. 80

Table 4.5: Variables and levels used to analyze sensitivity of model results. 101

Table 5.1: Printing parameters for PEI simulations. 119

Table 5.2: Ultem 1010 properties. 119

Table 7.1: Predicted and experimental shear stress and degree of healing for each set of printing parameters. 133

Chapter 1: Introduction

1.1 Introduction to FFF

Additive manufacturing (AM) has gained great popularity in both the academic and industrial spheres due to the low amount of material wasted during processing and the ability to create complicated geometries [1-3]. Fused Filament Fabrication (FFF), one of the most prevalent modalities of additive manufacturing [4], is a process in which a three-dimensional object is produced by extruding a filament in layers until a three-dimensional structure is formed. As the filament is extruded, it bonds to the print bed or previously printed filament to create a solid structure. While a number of additive manufacturing techniques exist, FFF distinguishes itself from the others by using a filament feedstock rather than liquid resins or powders. FFF has a number of advantages over these other methods including the simplicity and low cost of its fabrication system and its capability of producing parts with multiple materials [5].

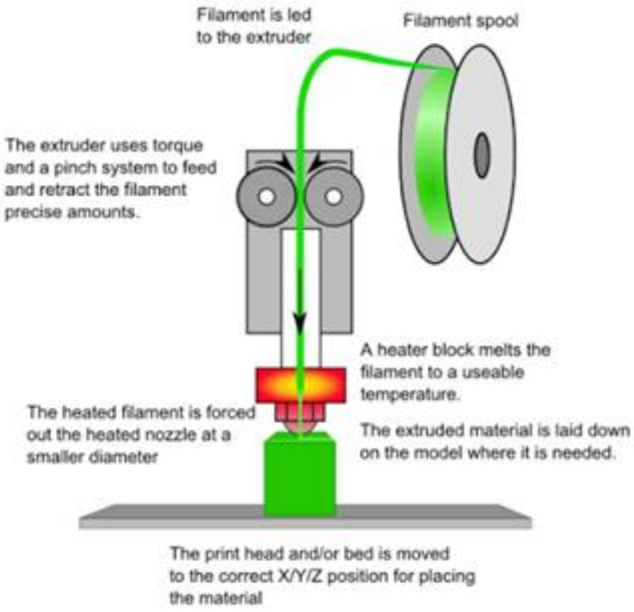

Fig. 1.1: Diagram of the FFF process [6].

Despite its vast potential, applications of FFF have been limited due to issues caused by non-optimized printing parameters. To produce a part with end use capabilities, numerous parameters must be optimized including layer thickness, part orientation, raster angle, raster width, air gap, and deposition temperature [7]. Determining the optimal parameters for each part is challenging due to the enormous number of variables which interact with each other. Furthermore, each parameter must be optimized for every new material because there is a strong material dependence on the optimal values. Currently, the values of these parameters are found primarily through empirical methods which can be very time consuming. Models have been developed to predict the optimal values, however, the complexity of the thermal and transport processes has limited their effectiveness. In particular, many of these models utilize unrealistic approximations such as constant temperature and filament velocity due to insufficient research on the actual conditions within FFF nozzles [8-13]. A more thorough understanding of the conditions within FFF nozzles would contribute greatly to these models thereby aiding in the optimization of process parameters.

Additionally, many models do not adequately account for a number of phenomena critical to FFF including interlayer diffusion, deformation between the printing of layers, and crystallization. The effects of crystallization in particular have not been accounted for as much of the work done to date in the field of FFF has been done with amorphous materials which experience less shrinkage upon cooling. Nevertheless, in order to develop parts that can be used for high performance applications such as the aerospace industry, the use of semi-crystalline materials needs to become possible as these materials offer a wide variety of advantages over amorphous materials including higher temperature limits, strength, fatigue resistance, and chemical resistance [14]. For this to happen, a better understanding of the crystallization behavior of materials printed by FFF needs to be gained as well as the effect of crystallinity on the final properties. This will greatly aid in the process of developing semi-crystalline filaments and could lead to the development of the next generation of FFF materials [15].

1.2 Research Objectives

The overall objective of this thesis is to significantly improve the understanding of the physics associated with the FFF process. To this end we two research objectives are presented.

Research objective 1: Analyze the in-situ conditions of FFF nozzles to improve understanding of the polymer flow behavior and enable process monitoring.

Herein, we describe the first reported method of measuring both temperature and pressure within the polymer flow field in the hot end of an FFF printer. We have identified a system design and components to directly measure the temperature of the flow field at multiple locations within the nozzle, as well as directly measuring pressure drop without significantly impacting the flow field. By using a piezoresistive pressure transducer along with a custom designed thermocouple insertion device, we successfully measured and analyzed the internal conditions of FFF nozzles as a function of filament feed rate and deposition temperature to determine the in-situ rheology of the polymer melt as a function of system geometry.

Research objective 2: Develop first principle models which account for crystallization, heat transfer and polymer diffusion in an effort to model the complex multiphysics of the FFF process.

Models for predicting the properties of FFF parts and the effect of crystallization on those properties are herein presented. A simple heat transfer model was applied to a 2D cross section of an FFF print to determine the temperature distribution throughout the print over the entirety of the printing process. Using the temperature information, a non-isothermal crystallization model was applied to determine the crystallinity throughout the part at all times in the deposition process. The temperature and crystallization data were then applied to novel models for the degree of healing and residual stress at each layer; which are the first reported models which account for the effect of crystallinity on healing and cumulative buildup of stress during FFF processes. This was done at various printing conditions to assess the effect of each printing parameter on the crystallinity and material properties. Several material properties were also changed to determine their effect on part properties as well. Finally, the initial experimental validation of the models using amorphous polyether imide (PEI) is presented. The tear strength and warpage of parts printed over a range of deposition temperatures, bed temperatures, and print speed were measured and compared to model predictions.

References

[1] S. Ford and M. Despeisse, "Additive manufacturing and sustainability: an exploratory study of the advantages and challenges," *Journal of Cleaner Production,* vol. 137, pp. 1573-1587, 2016/11/20/ 2016.

[2] B. Berman, "3-D printing: The new industrial revolution," *Business Horizons,* vol. 55, no. 2, pp. 155-162, 2012/03/01/ 2012.

[3] Y. Huang, M. C. Leu, J. Mazumder, and A. Donmez, "Additive Manufacturing: Current State, Future Potential, Gaps and Needs, and Recommendations," *Journal of Manufacturing Science and Engineering,* vol. 137, no. 1, pp. 014001-014001-10, 2015.

[4] T. Wohlers. (2016, May 2016) Additive Manufacturing: The State of the Industry. *Manufactuing Engineering*.

[5] A. Ghazanfari, W. Li, M. C. Leu, and G. E. Hilmas, "A novel freeform extrusion fabrication process for producing solid ceramic components with uniform layered radiation drying," *Additive Manufacturing,* vol. 15, pp. 102-112, 2017.

[6] D. Feeney. (2013, September 22 2016). *FFF vs. SLA vs. SLS - 3D Printing*. Available: https://www.sd3d.com/fff-vs-sla-vs-sls/

[7] G. C. Onwubolu and F. Rayegani, "Characterization and Optimization of Mechanical Properties of ABS Parts Manufactured by the Fused Deposition Modelling Process," *International Journal of Manufacturing Engineering,* vol. 2014, p. 13, 2014, Art. no. 598531.

[8] M. Firoz, "Physics based modeling of filaments melting in fused deposition modeling for 3D printing," State University of New York at Buffalo, 2016.

[9] H. S. Ramanath, C. K. Chua, K. F. Leong, and K. D. Shah, "Melt flow behaviour of poly-ε-caprolactone in fused deposition modelling," *Journal of Materials Science: Materials in Medicine,* journal article vol. 19, no. 7, pp. 2541-2550, 2007.

[10] N. Mostafa, H. M. Syed, S. Igor, and G. Andrew, "A study of melt flow analysis of an ABS-Iron composite in fused deposition modelling process," *Tsinghua Science and Technology,* vol. 14, no. S1, pp. 29-37, 2009.

[11] B. N. Turner, R. Strong, and S. A. Gold, "A review of melt extrusion additive manufacturing processes: I. Process design and modeling," *Rapid Prototyping Journal,* vol. 20, no. 3, pp. 192-204, 2014.

[12] T. P. Hofstätter, Rodrigo; Pedersen, David Bue; Mischkot, Michael; Hansen, Hans and Nørgaard, "Simulation of a Downsized FDM Nozzle," in *Proceedings. COMSOL conference 2015*, 2015.

[13] A. Bellini, S. I. Güceri, U. Drexel, and E. College of, "Fused deposition of ceramics: a comprehensive experimental, analytical and computational study of material behavior, fabrication process and equipment design," Drexel University, Philadelphia, 2002.

[14] N. K. MacVarish. (2017, 9/27/2017). *The Difference Between Amorphous & Semi-crystalline Polymers*. Available: http://blog.impactplastics-ct.com/blog/the-difference-between-amorphous-semi-crystalline-polymers

[15] E. L. Gilmer *et al.*, "Model analysis of feedstock behavior in fused filament fabrication: Enabling rapid materials screening," *Polymer,* vol. 152, pp. 51-61, 2018.

Chapter 2: Literature Review

In this chapter, previous studies pertinent to my research objectives are explored. Sections 2.1-2 address the main challenges faced by FFF applications as well as the current models which explore these problems. Sections 2.3-5 address the current uses and limitations of semi-crystalline materials in FFF applications, the prevailing nonisothermal crystallization models, and the existing understanding of how crystallinity affects interfacial healing in polymeric materials. Finally, Sections 2.6-7 address prior experimental methods and theoretical models for measuring and predicating the in-situ rheology of FFF nozzles.

2.1 Interlayer Mechanical Strength

One of the main challenges which limits FFF from being used in end use parts is the low mechanical strength perpendicular to the direction of print. In the case of polymeric filaments, this issue is due to insufficient healing between adjacent roads. Healing describes the process in which the polymer chains of both roads diffuse into the adjacent road and re-entangle, thereby forming a physical connection. It is assumed that when the chains have had time to fully move into the adjacent road and relax, the strength of the bond will be equal to the bulk material strength. For time scales less than the reptation time, the strength of welded polymer interfaces has been shown to vary with $t^{1/4}$ until reaching bulk properties at about τ_r (Eq. 2.1) [1, 2].

$$D_h(t) = \frac{\sigma}{\sigma_\infty} = \left(\frac{t}{\tau_r}\right)^{\frac{1}{4}} \tag{2.1}$$

where τ_r is the reptation time and σ_∞ is the bulk strength. Similarly, fracture energy has been shown to vary with $t^{1/2}$ (Eq. 2.2).

$$\frac{G_{ic}}{G_{ic\infty}} = \left(\frac{t}{\tau_r}\right)^{\frac{1}{2}} \tag{2.2}$$

Eq. 2.1 applies to isothermal conditions but was extended to a discretized form by Bastien and Gillespie [3] so that it could be applied to non-isothermal conditions (Eqs. 2.3-4).

$$D_h(t_h) = \frac{1}{\tau_r^{*\frac{1}{4}}} \sum_{j=1}^{\frac{t_h}{dt}} \frac{(t_j)^{\frac{1}{4}} - (t_{j-1})^{\frac{1}{4}}}{(a_T\left(T_{avg}(t_j)\right)^{\frac{1}{4}}} \tag{2.3}$$

$$a_T(T) = exp\left[\frac{E_a}{R}\left(\frac{1}{T_{avg}} - \frac{1}{T_{ref}}\right)\right] \tag{2.4}$$

where t_h is the total time of healing, dt is the time step used, t_j is equal to dt·j, $T_{avg}(t_j)$ is the temperature at time j, τ_r^* is the reptation time at the reference temperature, T_{ref} is the reference temperature, R is the ideal gas constant, and D_h is the degree of healing or ratio of the strength to the bulk strength [4]. Reptation time can be found from oscillatory shear measurements as the intersection of G' and G" (Maxwell's relaxation time) [5].

This model includes absolute time making it sensitive to time spent outside the diffusion range and later temperatures more significant than earlier temperatures. To address this, another model (Eq. 2.5) was proposed by Yang et al.[6] and successfully applied by Sun [7].

$$Degree\ of\ Healing = \left(\int_0^t \frac{1}{\tau_r(T)} dt\right)^{\frac{1}{4}} \tag{2.5}$$

According to these models, sufficient time must be spent at temperatures high enough for molecular mobility in order for diffusion to take place. This can be difficult to achieve in FFF as deposited roads often cool rapidly through the diffusion region. Adjusting the printing parameters of the FFF process can affect the cooling behavior of each layer thereby affecting the strength of the bond. Unfortunately, current methods for measuring or predicting the temperature distribution in FFF parts during printing are limited due to the complexity of the process and dependence on numerous printing parameters. As each layer is deposited, it heats the previously printed material.

Since the polymer chains must move into this adjacent material, the temperature at the surface of adjacent material must be high enough for diffusion. Therefore, significant heating must take place upon deposition of each new road. Models for predicting healing must be able to accurately account for the heating of the next layer as well any subsequent layers as it has been shown that noticeable fluctuations in temperature can be seen for as many as 15 layers in FFF parts [8].

The simplest models to predict the temperature in FFF parts which have been used are transient heat transfer models. These models fail to properly account for the heating of lower layers, however, showing no significant heating of a layer with subsequent printing [9] or for only the very next layer [10]. Another commonly employed model for heat transfer in FFF parts is finite element analysis (FEA). This method is attractive as it allows for accurate 3D data on heat transfer as well as other phenomena important to FFF; such as deformation of the layers. As such, it has been used to optimize a number of applications including scaffold structures [11-15]. The main disadvantage of FEA analysis is that it is very computationally intensive. Even when working with 2D simulations, these simulations need to be run for days on high performance computers to get detailed results [16]. Additionally, despite the processing time used in these simulations, current models fail to account for deformations that happen as roads are deposited making the ability of FEA to predict the properties of parts prior to printing limited [17, 18].

Another method to model temperature is to use a finite difference model. This method is similar to FEA but uses rectangular elements to greatly simplify the equations. Using Gaussian divergence theorem, the three-dimensional heat equation for pure conduction assuming constant density, heat capacity, and thermal conductivity can be derived according to Eq. 2.6 [19].

$$\mu\rho\frac{\partial T}{\partial t} = K\left(\frac{\partial^2 T}{\partial x^2} + \frac{\partial^2 T}{\partial y^2} + \frac{\partial^2 T}{\partial z^2}\right) \tag{2.6}$$

This equation can be discretized to apply to a three-dimensional element of size dx by dy by dz over a time step dt according to Eqs. 2.7-9.

$$\frac{dT}{dt}=\frac{K}{\mu\rho}\left(\frac{\frac{\partial T}{\partial x_r}-\frac{\partial T}{\partial x_l}}{dx}+\frac{\frac{\partial T}{\partial y_t}-\frac{\partial T}{\partial y_b}}{dy}+\frac{\frac{\partial T}{\partial z_b}-\frac{\partial T}{\partial z_f}}{dz}\right) \tag{2.7}$$

$$\frac{dT}{dt}=\frac{K}{\mu\rho}\left(\frac{(T_r-T)-(T-T_l)}{dx^2}+\frac{(T_t-T)-(T-T_b)}{dy^2}+\frac{(T_b-T)-(T-T_f)}{dz^2}\right) \tag{2.8}$$

$$\frac{dT}{dt}=\frac{K}{\mu\rho}\left(\frac{T_r+T_l-2T}{dx^2}+\frac{T_t+T_b-2T}{dy^2}+\frac{T_b+T_f-2T}{dz^2}\right) \tag{2.9}$$

For the case of elements exposed to air, there is an additional heat loss due to convection. Because the convection surface is not closed, divergence theorem does not apply but the heat transfer for the specific case of a volume element of temperature T can still be found using the basic heat transfer by convection relationship (Eq. 2.10).

$$\dot{Q}=h(T_{env}-T)\mathrm{A} \tag{2.10}$$

where A is the area of the element exposed to air, h is the heat transfer coefficient, and T_{air} is the temperature of the air. This expression can be rewritten as Eq. 2.11 or 2.12.

$$\frac{\mu\rho dTdxdydz}{dt}=h(T_{env}-T)A \tag{2.11}$$

$$\frac{dT}{dt}=\frac{hA}{\mu\rho dxdydz}(T_{env}-T) \tag{2.12}$$

Adding Eq. 2.12 to Eq. 2.9 yields Eq. 2.13

$$\frac{dT}{dt}=\frac{K}{\mu\rho}\left(\frac{T_r+T_l-2T}{dx^2}+\frac{T_t+T_b-2T}{dy^2}+\frac{T_b+T_f-2T}{dz^2}\right)+\frac{hA}{\mu\rho dxdydz}(T_{env}-T) \tag{2.13}$$

When using a finite difference model for heat transfer, it is necessary that the amount of thermal energy leaving the element over a time step does not exceed the thermal energy in the element. If it does, the temperature will oscillate with increasing amplitude and the system will be unstable [20]. The temperature of an element using the finite difference model is expressed by Eq. 2.14.

$$T_{x,y,t+1} = T_{x,y,t} + \Delta T_{x-1,y,t} + \Delta T_{x+1,y,t} + \Delta T_{x,y-1,t} + \Delta T_{x,y+1,t} \tag{2.14}$$

For the case of internal elements, left edge elements, and top left corner elements respectively, this yields Eqs. 2.15-17.

$$\begin{aligned} T_{x,y,t+1,internal} = T_{x,y,t}&\left(1 - \frac{kdt}{\rho c_p}\left(\frac{2}{dx^2} + \frac{2}{dy^2}\right)\right) \\ &+ \frac{kdt}{\rho c_p}\left(\frac{T_{x-1,y,t} + T_{x+1,y,t}}{dx^2} + \frac{T_{x,y-1,t} + T_{x,y+1,t}}{dy^2}\right) \end{aligned} \tag{2.15}$$

$$\begin{aligned} T_{x,y,t+1,edge} = T_{x,y,t}&\left(1 - \frac{kdt}{\rho c_p}\left(\frac{1}{dx^2} + \frac{2}{dy^2} + \frac{h}{dxk}\right)\right) \\ &+ \frac{kdt}{\rho c_p}\left(\frac{T_{x+1,y,t}}{dx^2} + \frac{T_{x,y-1,t} + T_{x,y+1,t}}{dy^2} + \frac{hT_{air}}{kdx}\right) \end{aligned} \tag{2.16}$$

$$\begin{aligned} T_{x,y,t+1,corner} = T_{x,y,t}&\left(1 - \frac{kdt}{\rho c_p}\left(\frac{1}{dx^2} + \frac{1}{dy^2} + \frac{h}{kdx} + \frac{h}{kdy}\right)\right) \\ &+ \frac{kdt}{\rho c_p}\left(\frac{T_{x+1,y,t}}{dx^2} + \frac{T_{x,y-1,t}}{dy^2} + \frac{hT_{air}}{kdx} + \frac{hT_{air}}{kdy}\right) \end{aligned} \tag{2.17}$$

In these equations the first term correlates to the previous thermal energy minus the energy that leaves to adjacent cells or the environment (expressed as temperature and change in temperature). If the energy loss cannot exceed the energy within the element, then the following restrictions apply to the system (Eq. 2.18-20)

$$1 - \frac{kdt}{\rho c_p}\left(\frac{2}{dx^2} + \frac{2}{dy^2}\right) \geq 0 \tag{2.18}$$

$$1 - \frac{kdt}{\rho c_p}\left(\frac{1}{dx^2} + \frac{2}{dy^2} + \frac{h}{dxk}\right) \geq 0 \tag{2.19}$$

$$1-\frac{kdt}{\rho c_p}\left(\frac{1}{dx^2}+\frac{1}{dy^2}+\frac{h}{kdx}+\frac{h}{kdy}\right)\geq 0 \tag{2.20}$$

It can be seen that the internal elements provide the greatest restriction on the maximum value of dt; provided that Eqs. 2.21-22 hold true.

$$\frac{h}{kdy}\leq\frac{1}{dy^2} \tag{2.21}$$

$$dy\leq\frac{k}{h} \tag{2.22}$$

While this method allows for a simple but flexible way to model FFF, no studies have used finite difference methods to model the FFF process. Due to the limitations of current temperature models, healing in FFF parts as a function of printing parameters is usually determined though experimental means. In work done by Ahn et al., they found that the tensile strength of FFF parts ranged from 10% of the strength of injected molded parts using a raster angle of 90° to 73% using a raster angle of 0° and using a negative air gap increased the strength at all orientations. No significant effect of bead width, color, or deposition temperature were found [21]. Very similar results were found by Dawoud et al. [22]. Sood et al. studied the tensile, flexural and impact strength of FFF as a function of thickness, orientation, raster angle, raster width and raster gap. Responses showed complicated interaction and that often multiple processes compete against each other. For instance, increased number of layers lead to better diffusion which increased strength but increased distortion which lowered the strength. Overall, the optimal parameters for tensile and flexural strength were found to be the highest values tested for layer thickness and raster width and lowest values of orientation, raster angle, and air gap [23]. Another important finding by Sun et al. was that the environment temperature and changes in convective conditions greatly impact the strength of parts, thereby creating a source for variation in part properties for different prints [8].

2.2 Dimensional Tolerance, Warping and Residual Stress

Another main limitation of FFF is achieving the necessary dimensional tolerances in a part. Insufficient dimensional tolerances arise from several phenomena including the size of the nozzle tip, inconsistent filament flow, inter-road interactions, predicting road dimensions, and changes in density during cooling.

Because the surface of FFF parts are made from pseudo-cylindrical roads, the surface roughness of FFF parts is inherently poorer than most machined parts [24]. Predicting this roughness is challenging, however, as the dimension of the roads are difficult to determine. As the roads are extruded, they are cylinders. When they come into contact with the part, they deform into a more ellipsoid shape and deform further while the road is still viscous due to gravity. Accounting for all these phenomena is very computationally intensive and limited to the printing parameters used; making exact predictions of geometry of the roads as a function of printing parameters impractical. Gleadall et al. worked to simplify the process by ignoring viscous effects and predicting that the filament will move to the closest free volume with reasonable results [17]. One important limitation of this model mentioned in the paper is that it requires constant filament deposition rate. While ideally this would hold true, due to effects like thermal fluctuations, inconsistent filament diameter, and nozzle blockages the flow rate experiences significant fluctuations during printing [25]. At minimum, changes in flow rate will lead to higher surface roughness. In cases of extreme underflow or overflow, however, they can lead to part failure as a critical section is missing or desired voids are filled. Ensuring the filament is as constant as possible will reduce this error though a method to effectively monitor fluctuations in flow rate is ultimately necessary to account for all sources of variation.

Another issue that affects part geometry is the decrease in the volume of the filament during processing. Most materials have positive thermal expansion coefficients which means they decrease in volume as they cool from the deposition temperature to room temperature. This has a drastic impact on the FFF process as the bottom layer is restricted from contracting due to bonding with the printing bed. Since the road is prevented from contracting, residual stresses build in the road. As additional roads are deposited, they add to the residual stress. This stress increases until the part is finished, or it is relieved through deformation. Initially, parts experience warpage where the extremities of the part lift off the build plate. Depending on the dimensional tolerances of the part, this alone may prevent the part from meeting the required dimensional accuracy. In severe cases, warpage can become severe enough that the top of the part is no longer flat, causing the next layers to print improperly. In the most extreme cases, contact with the bed (or a previous layer) can decrease such that the part no longer sticks to the bed (or previous layer) and the part detaches leading to failure [26]. It has been shown that this kind of deformation is often the most severe geometric error in FFF parts [27], though the degree of warpage is highly dependent on the printing parameters and material used [28]. Previous studies on the effect of material properties on part warpage have shown that CTE is strongly linked to warpage while thermal conductivity, heat capacity, and Young's modulus are not [29].

Materials with lower glass transition temperatures experience less warpage; as their processing temperature is lower [26]. For high performance applications, it is often necessary to use high grades of polymers which do not meet those requirements. As such, it is important to be able to adjust printing parameters to minimize warpage in even problematic materials. A common method to overcome warping is to use an adhesive to keep the part sticking to the bed [30]. While this method reduces peeling off the bed, it does not reduce the residual stress in the part and is only effective to a certain degree, especially in high performance applications where the adhesive alone is not enough to prevent warpage.

Several experimental studies have been done on the effect of printing properties on residual stress. The stress at different raster angles and layer thickness was investigated by Kantaros and Karalekas using a short fiber Bragg grating (FBG) embedded in an FDM part [28]. They found that for a layer thickness of 0.25 mm, the stress in the parts with a raster angle of 0° was lower than those with an angle of 90° or 45°. For a thickness of 0.5, however, the 0° and 45° orientations had the highest strains. Zhang and Chou found supporting results where the printing speed was the most critical parameter followed by layer thickness and its interaction with road width [31]. Another study using an FBG showed that the increase in strain for acrylonitrile butadiene styrene (ABS) when heating to its Tg was on the range of 7-8 mm/m and the increase in strain when heating past the Tg was negligible. This test showed that when given enough time, strain in FFF parts above the Tg will be reduced; though these specimens were given 15 min to equilibrate which is much faster than during printing [32]. Additionally, measurements of the residual stress in FFF parts using a hole-drilling method have shown residual stresses as high as 6 MPa [33]. Nazan et al. investigated the effect of printing temperature, fill density, first layer height, and layer height on the warp deformation at the corners of an unspecified material [34]. They found that deformation is positively related to temperature and fill density, negatively related to layer height, and not impacted by first layer height at the levels studied. Alsoufi and Elsayed studied the effect of printing speed and deposition temperature on the degree of warping at the corners of polylactic acid (PLA) parts [35]. They found that higher temperatures reduced the degree of warping from

8.85% to 4.55% when using an adhesive though no trend could be seen when no adhesive was used and when changing the printing speed.

In addition to causing warpage, shrinkage of FFF parts also causes a change in the dimensions of the part. The percentage change is often described as the accuracy of the print and has been studied as a function of processing parameters using a variety of different process optimization methods. Sood et al. studied the effect of layer thickness, part orientation, raster angle, air gap and raster width on accuracy using both Taguchi's parameter design and a fuzzy logic approach and found that part orientation was the most important parameter follows by its interactions with raster length, width, and gap [36, 37]. Unfortunately, they found that a positive air gap increased the accuracy of FFF parts, while previous studies found that a positive air gap reduces tensile strength [21].

Modeling of warpage in FFF parts has been mostly done using FEA. Zhang and Chou used FEA to model warpage and found that stress is very dependent on the tool path [38]. They found that the largest residual stresses were in the direction of the tool path. Experimental results show longer raster paths had greater degrees of warping, but the simulation results predicted lower degrees of warpage. This was suggested to be due to the boundary conditions but could also be due to the fact that the model did not deform between layers. This is a limitation of FEA analysis as including mechanical deformation between each layer greatly increase the computational intensity of the simulation. FEA was also used by Gleadall et al. to improve their predictions of road dimensions with a similar limitation of ignoring deformation between layers [17]. Work by Watanabe et al. using ANSYS modeled the warpage of polypropylene at different deposition temperatures, deposition speeds, and layer heights [39]. This study found that deposition temperature had little effect on the warpage, faster deposition speeds decreased warpage, and larger layer heights decreased warpage for the experimental results. Due to the computational time required for the simulations, only two 5 mm roads were deposited as opposed to the experimental results which had 5 20 mm roads. Nonetheless, by interpolating the experimental results, good agreement was found to the simulation data with the exception of the effect of layer height. As with the previous work, these simulations did not factor in warpage between the printing of layers.

Given the computational intensity of FEA, simpler methods of modeling the FFF process are necessary to run large numbers of simulations such as those necessary to optimize printing parameters. In their work on warp deformation, Wang et. al developed a mathematical model without the use of FEA using the following simplifications [26]. First, the contraction of the filaments only occurs between the Tg and the chamber temperature as when above the Tg the filament is unable to resist outside force. Second, deposited layers are equal to the chamber temperature as cooling in parts is much faster than the time required to deposit a layer. Finally, they assumed that each layer was deposited instantly and there are no voids between layers. Initially, the stress in the layer was assumed to be equal to the stress required to stretch the layer from the length in the unconstrained case to the deposition length. The part was then allowed to bend to reduce the stress in the top layer. A disadvantage of this model was that it did not calculate the cumulative warpage caused by warpage of each layer separately.

2.3 Semi-Crystalline Polymers for FFF

Another limitation of FFF is the limited number of structural materials available. While advances are continuing to be made, the process is slow due to limitations of many commercially available printers, the difficulty of printing materials with large changes in density, and the long development times needed to optimize printing parameters.

One major oversight in available materials is semi-crystalline materials. Semi-crystalline polymers have a number of advantages over amorphous polymers due to their difference in structure. In amorphous polymers, the polymer experiences significant softening at its glass transition temperature. This leads to a large decrease in the elastic modulus of the material that in many cases limits the maximum service temperature of the polymer to around the Tg. In crystalline polymers, however, the crystalline regions restrict movement of the polymer chains keeping the material stiff at temperatures up to the melting point of the crystalline regions. This gives semi-crystalline polymers greater service temperatures in many cases. Additionally, semi-crystalline polymers often have better chemical resistance because the dense crystalline regions can be difficult for chemicals to penetrate. Some downsides of semi-crystalline materials are they are often more brittle, due to the inflexible crystalline regions, and experience greater shrinkage from melt due to the crystallization process [29, 40]. Each of these properties are also highly dependent on chemical structure such that there are exceptions to these trends. Nevertheless, these trends are important as they show how one of the major challenges in FFF (large degrees of shrinkage as the part cools) discourages the use of semi-crystalline polymers. Because of this, there are very few commercially available filaments for FFF which crystallize. In many cases “semi-crystalline” materials are used, such as nylon 6, but these are often modified to hinder crystallization [41, 42]. There are some cases of genuinely semi-crystalline materials being used for FFF in literature such as PLA, polypropylene (PP), polyether ether ketone (PEEK), Polyetherketoneketone (PEKK), and polyphenylene sulfide (PPS) [43-47]. Use of these materials is limited, however, because these materials typically require high levels of reinforcement to overcome residual stresses and defects often negatively impact the local crystallization. Since the high temperature and chemical resistance of semi-crystalline materials is important in applications like aerospace, being able to overcome this limitation is critical.

Additionally, while printers exist which are capable of printing high performance materials, obtaining consistent and accurate prints with high performance materials has continued to be a challenge. Some examples of high-performance polymers include PEI and PEEK. To print these materials a printer must be able to go to at least 350 °C though higher temperatures may be needed to get better bonding between layers. Because of these extreme conditions, only a handful of printers are commercially available which can even extrude the materials. In addition to the deposition temperature, successful prints of these materials often require high temperature beds and chambers. Of the known commercially available printers, the maximum nozzle, bed, and chamber temperature are 520, 280, and 200 °C respectively; all on different printers [38].

One potential method to reduce the shrinkage of FFF parts is to add a filler to reduce the coefficient of thermal expansion or one of the other material properties [29, 42, 45, 48-57]. The addition of carbon fibers for instance has been shown to greatly increase the strength and stiffness of FFF parts and reduce the warpage [58]. Further study needs to be done to quantify how this effect depends on fiber concentration and alignment, as well as how changes in printing parameters affects fiber alignment [57].

2.4 Modelling Crystallization

Crystallinity in polymers can significantly increase mechanical performance over comparable amorphous polymers [59, 60]. Thus, it is imperative to ensure that the processing conditions of semi-crystalline polymers used in FFF allow for adequate crystallization. The most commonly used approach to model and predict crystallization in polymers deals with the formation of nuclei due to thermal gradients within the polymer melt and the subsequent growth of the nuclei till a stable crystalline framework is achieved; showing that polymer crystallization is governed by both the nucleation and growth kinetics [61, 62].

Early efforts at simulating the crystallization processes were limited to isothermal conditions which do not consider the complications associated with temperature gradients in the melt. The classical crystallization kinetics model was first developed independently by Avrami [63, 64] and Kolmogoroff [65] both of whom were working on metal crystallization. The Avrami equation (Eq. 2.23) has been widely used to predict the crystallization kinetics of polymers [66, 67].

$$X_c = X_{c\infty}(1 - exp[-k(T) * t^n]) \qquad (2.23)$$

where, X_c is the volume fraction crystallinity, $X_{c\infty}$ is the equilibrium volume fraction crystallinity, k is the crystallization rate constant that accounts for both nucleation and growth kinetics, and n is the Avrami exponent which is a characteristic of the mechanism of crystallization. This equation has a number of assumptions including constant volume, constant linear growth rate, continuous number of nuclei, and single stage crystallization [68]. While most of these assumptions are reasonable for FFF, the highly nonisothermal of the process means the linear growth rate is not constant. Several models have been developed over the years to incorporate deviations from isothermal conditions. Ozawa [69] modelled crystallization under nonisothermal conditions as an infinite series of steps under isothermal conditions. Using this assumption, the crystallinity at a constant cooling rate was expressed according to Eq. 2.24.

$$\alpha(t) = \frac{X_c(T)}{X_{c\infty}} = 1 - exp\left[\frac{-x(T)}{\varphi^m}\right] \qquad (2.24)$$

where, $X_c(T)$ is the relative crystallization fraction at temperature T, x(T) is the cooling or heating function, and m is the Ozawa exponent which is dependent on the dimension of the crystal growth and the mechanism of nucleation. This model was validated with polyethylene terephthalate (PET) at cooling rates of 1-4 °C/min. The Ozawa model does not take into account secondary crystallization and hence cannot be used to explain the non-isothermal kinetics of polymers like PEEK or polyethylene (PE) [70, 71]. Additionally, this equation is limited to constant cooling rates which are not representative of FFF. Finally, the value of m and the fold length are assumed to be independent of temperature which is not true over large temperature ranges. Hammami et al. showed that the Ozawa equation could be modified to Eqs. 2.25-26 [72].

$$\alpha = (1 - exp[-\psi(T) * t^n]) \tag{2.25}$$

where

$$\psi(T) = \frac{x(T)}{\Delta T^n} = c1 * exp\left[\frac{-3U^*}{R\left(T - T_g + 51.6\right)} - \frac{3c2}{T(T_m^\circ - T)f}\right] \tag{2.26}$$

and f = 2T/(T+T_m°) is a correction factor accounting for the reduction in the latent heat of fusion as the temperature is decreased. The equation for ψ was obtained by assuming ψ has the same temperature dependency as k, is thermal heterogeneous nucleation, and follows Hoffman-Lauritzen theory [73]. This model was applied to DSC data of isotactic polypropylene (iPP) at cooling rates from 2-40 °C/min. While this model extended the applicable temperature range, it suffers from some of the main problems of the Ozawa equation, mainly that it only applies to constant cooling rates and cannot factor in multiple crystallization mechanism. Another modified Avrami model was proposed by Kamal and Chu (Eq. 2.27) [74].

$$\frac{X_c}{X_{c\infty}} = 1 - exp\left[-\int_0^t k(T)nt^{n-1}dt\right] \tag{2.27}$$

This model was fit to crystallinity data of high-density polyethylene at cooling rates from 2.5-20 °C/min with 15% accuracy. An issue found in this model is that it is highly dependent on the temperature at which the process starts. This is due to the time term within the integral which increases and decrease depending on the starting temperature. This also affects the ability of the model to predict cooling behavior that is not constant as time spent at temperatures outside the crystallization range affects the model greatly.

Nakamura [75] and Ziabicki [76] modified the Avrami equation by employing the phase transformation theory based on isokinetic conditions to derive a non-isothermal kinetic equation (Eq. 2.28). This approach modeled the dynamic solidification process by taking into account the transient thermal and athermal effects [76]. The thermal nucleation process was assumed to control crystallization by affecting relaxations which can hinder crystallization.

$$\frac{X_c}{X_{c\infty}}(T) = 1 - exp\left[-\left(\int_0^t K(T)dt\right)^n\right] \qquad (2.28)$$

where $K = k^{1/n}$. The temperature dependency was given as Eq. 2.29.

$$k(T) = -c1 * exp\left[\frac{-c2 * T}{\left(T - T_g + 51.6\right)^2} - \frac{c3 * T_m}{T(T_m^\circ - T)}\right] \qquad (2.29)$$

The temperature dependency of k was obtained from Takayanagi and Kusumoto [77]. This model was originally applied to high density polyethylene at only very small cooling rates (<0.5 °C/min). A similar model first introduced by Patel and Sprueill can be obtained by deriving the Nakamura model. This is known as the Jonhson–Mehl–Avrami (JMA) equation or differential Nakamura model (Eqs. 2.30-32) [78]. This model was applied to nylon 6 cooled at rates from 2-40 °C/min.

$$\frac{d\alpha(t)}{dt} = nK(T)\left(1 - \alpha(t)\right)ln\left[\frac{1}{1 - \alpha(t)}\right]^{\frac{n-1}{n}} \qquad (2.30)$$

or

$$\frac{dY}{dt} = nK(T)Y^{\frac{n-1}{n}} \qquad (2.31)$$

where

$$Y = n\left[\frac{1}{1-\alpha(t)}\right] \tag{2.32}$$

While some of the previous models showed reasonable agreement with experimental data, one major limitation of them is that they do not consider the effects of secondary crystallization on the kinetics. The secondary crystallization process originates by nucleation on the already formed crystals during the primary stage [79, 80]. An additional term to account for the transition from spherulitic growth to secondary crystallization was developed by Dietz [81]. This term was added to a differential form of the Kamal model (Eq. 2.33).

$$\frac{dX_c}{dt} = nk(T)(1-X_c)t^{n-1}Exp\left[\frac{-aX_c}{1-X_c}\right] \tag{2.33}$$

Velisaris and Seferis [82] proposed a dual crystallization mechanism for isothermal and non-isothermal crystallization by introducing a linear combination of two Kamal and Chu equations (Eqs. 2.34-37).

$$\frac{X_{vc}}{X_{vc\infty}} = w1 * F_{vc1} + w2 * F_{vc1} \tag{2.34}$$

where

$$F_{vci} = 1 - exp\left(-\int_0^t ki(T) * ni * t^{ni-1} dt\right) \tag{2.35}$$

$$w1 + w2 = 1 \tag{2.36}$$

$$ki(T) = T * c1 * exp\left(\frac{-c2}{T - T_g + 51.6} - \frac{c3}{T(T_{mi} - T)^2}\right) \tag{2.37}$$

where: c1 is a constant coefficient of the temperature dependent preexponential factor, c2 is an empirical parameter associated with the temperature dependence of viscosity, and c3 is a parameter associated with the free enthalpy of nucleation. The temperature dependency of k for these models is notably different from that of Ozawa and other as it is based on homogenous nucleation rather than heterogeneous. The validity of this model was proven by applying the model to experiments on PEEK. Although the model was based upon thermodynamic principles, it ultimately was an empirical model that was fitted to a particular material and thermal history. Therefore, in order to apply the model universally for non-isothermal conditions, several modifications were suggested by Cebe [83] based upon the Hoffman-Lauritzen nucleation theory. These modifications include replacing the experimental T_m values with the equilibrium melting temperature and changing the temperature dependency of k to reflect heterogeneous nucleation. With these changes, k(T) was expressed according to Eq. 2.38.

$$k(T) = c1 * exp\left(\frac{-c2}{T - T_g + 51.6} - \frac{c3 * 2T}{T(T_m^\circ + T)(T_m^\circ - T)}\right) \tag{2.38}$$

It should be noted that this expression is incorrect as the correction factor f was misrepresented as $\frac{(T_m^\circ + T)}{2T}$ when according to Hoffman-Lauritzen nucleation theory it is $\frac{2T}{(T_m^\circ + T)}$ [73]. By means of the correct value, the temperature dependency of k is expressed in Eq. 2.39

$$k(T) = c1 * exp\left(\frac{-c2}{(T - T_g + 51.6)} - \frac{c3(T_m^\circ + T)}{T^2(T_m^\circ - T)}\right) \tag{2.39}$$

Another important note that should be made is that the Hoffman-Lauritzen nucleation theory was derived for flexible polymers like polyethylene and applications to rigid polymers like PEEK and polyimides are not fully justified [73, 84].

There are a few limitations to the Avrami model; most notably that it overestimates crystallinity at values much greater than about 30% [85-87]. Another model, known as the Tobin model (Eqs. 2.40-42), has been proposed based on traditional thermodynamic approach which took into account the nucleation and growth steps of both heterogeneous and homogeneous crystallization processes [88].

$$\dot{\alpha}(t) = \dot{\alpha}_1(t) + \dot{\alpha}_2(t) \tag{2.40}$$

$$\dot{\alpha}_1(t) = k_1\, exp\left[\frac{-3E_d}{RT}\right] exp\left[\frac{-3\psi_1 T_m^{\circ}}{T(T_m^{\circ} - T)}\right] t^2\big(1 - \alpha(t)\big)^2 \tag{2.41}$$

$$\dot{\alpha}_2(t) = k_2 exp\left[\frac{-4E_d}{RT}\right] exp\left[\frac{-(3\psi_1 + \psi_2)T_m^{\circ}}{T(T_m^{\circ} - T)}\right] t^2\big(1 - \alpha(t)\big)^2 * \int_0^t (t-\omega)^2\big(1 - \alpha(\omega)\big)d\omega \tag{2.42}$$

where $\dot{\alpha}(t)$ is the overall crystallization rate at time t, $\dot{\alpha}_1(t)$ is the crystallization rate contributed by the growth process initiated by heterogeneous nucleation, $\dot{\alpha}_2(t)$ is the crystallization rate contributed by the growth process initiated by homogeneous nucleation, k_1 is the rate constant for $\dot{\alpha}_1(t)$, E_d is the diffusional activation energy of crystallizing segments across the phase boundary, ψ_1 is a constant related to the free energy of formation of a critical nucleus on the growing crystal surface, k_2 is the rate constant for $\dot{\alpha}_1(t)$, and ψ_2 is a constant related to the free energy of formation of a growth embryo in the homogeneous nucleation process.

Good agreement was seen between this model and experimental data on PEEK at cooling rates from 10-50 C/min. In a subsequent work, however, they found that there were problems associated with the rate of homogeneous nucleation and heat of fusion and the following corrections were suggested (Eqs. 2.43-44) [89]. This model was not tested by the author but attempts were made to fit the model to non-isothermal crystallization data of iPP; though no reasonable fit was found [90].

$$\dot{\alpha}_1(t) = k_1\, exp\left[\frac{-3E_d}{RT}\right] exp\left[\frac{-3\psi_1 T_m^{\circ}}{fT(T_m^{\circ} - T)}\right] t^2\big(1 - \alpha(t)\big)^2 \tag{2.43}$$

$$\dot{\alpha}_2(t) = k_2 exp\left[\frac{-4E_d}{RT} - \frac{\psi_2 T_m^{\circ\,2}}{f^2 T(T_m^\circ - T)} - \frac{3\psi_1 T_m^\circ}{fT(T_m^\circ - T)}\right] t^2\big(1-\alpha(t)\big)^2 * \int_0^t (t-\omega)^2\big(1-\alpha(\omega)\big)d\omega \qquad (2.44)$$

Another limitation of these models is that they do not consider the effect of induction time. Chan and Isayev [91] considered temperature lag effects and non-isothermal induction times which are applied to the differential Nakamura equation. Isothermal induction times were found from DSC and applied to the Eq. 2.45:

$$t_i = t_m(T_m^\circ - T)^{-a} \qquad (2.45)$$

where t_i is the induction time, and t_m and a are material constants in $s*K^a$ and unitless respectively. This data can be extended to nonisothermal conditions by solving Eq. 2.46 resulting in Eqs. 2.47-49 [92]:

$$1 = \int_0^{t_{ni}} \frac{dt}{t_i(T)} \qquad (2.46)$$

or

$$1 = \int_0^{t_{ni}} \frac{\big(T_m^\circ - T(t)\big)^a}{t_m} dt \qquad (2.47)$$

$$1 = \sum_{i=1}^{\frac{t_{ni}}{dt}} \frac{(T_m^\circ - T)^a}{t_m} dt \qquad (2.48)$$

$$\frac{t_m}{dt} = \sum_{i=1}^{\frac{t_{ni}}{dt}} (T_m^\circ - T)^a \qquad (2.49)$$

where t_{ni} is the nonisothermal induction time. Using this, the crystallinity of quenched PET was predicted with reasonable accuracy. A similar approach was applied by Mubarak et al. to model crystallization of iPP at cooling rates from 1-100 °C/min using the modified Ozawa, Kamal, integral Nakamakura, differential Nakamakura, and parallel Avrami models. Without accounting for induction time, all the models failed to accurately predict crystallinity at either high or low cooling rates. By accounting for induction time, however, the modified Ozawa equation showed good fit to the experimental data. The fits of the other models when accounting for induction time were not explored.

In addition to modelling crystallization growth, it is necessary to model the melting of the polymer as this reduces crystallinity. Greco & Maffezzoli proposed a model for the melting behavior of polymers by assuming that "no rate dependent effects are dominant during the re-melting process" and that there is "a statistical distribution of crystal sizes in the material that evolve during polymer crystallization" [93]. This range is linked to the range in the melting temperature from the DSC data based on Eq. 2.50.

$$\frac{dX_m}{dT} = k_m\, exp\left(-k_m\left(T - T_p\right)\right) * \left[1 + (d-1)\, exp\left(-k_m\left(T - T_p\right)\right)\right]^{\frac{d}{1-d}} \qquad (2.50)$$

where X_m is the degree of melting, T_p is the peak melting temperature, k_m is the intensity factor related to the sharpness of the distribution, and d is a shape factor controlling the dispersion of melting temperatures lower than T_m. The total degree of melting at a temperature T can then be given by the integral (Eq. 2.51).

$$X_m(T) = \left(1 + (d-1)\, exp\left[-k_m\left(T - T_p\right)\right]\right)^{\frac{1}{1-d}} \qquad (2.51)$$

2.5 Effect of Crystallinity on Healing

The addition of crystallinity greatly complicates the diffusion model as it hinders diffusion into the crystalline phase as well as restricts movement of chains out of the crystalline phase. Because of this, the degree of healing must account for both effects. It has been shown in literature that amorphous/crystalline and crystalline/crystalline interfaces are still diffusion dominated [94].

Additionally, it has been suggested that the diffusion of polymer chains into semi-crystalline phases happens primary into the amorphous regions [95, 96]. Aside from this, little is known about the relationship between healing and crystallinity to date. In their work on PET interfaces, Boiko et al. [94] found that crystalline/crystalline interfaces showed healings one order of magnitude lower than those of amorphous/amorphous and amorphous/crystalline interfaces. Additionally, the amorphous/crystalline interface showed a lower degree of healing than the amorphous/amorphous interface, with significantly low degrees of healing when using a higher crystallinity sample. These results show that increased crystallinity hinders healing at polymer interfaces but did not attempt to fit this to any relationship outside of the basic diffusion equation. Similar results were found in PEEK by Cho and Krados [97] and Agawa et al. [98]. These results found that the bond strength exceeded the strength which can be accounted for through diffusion alone and suggested that crystallization at the interface lead to increased healing. This phenomena in which the crystallizing phase pulls the diffusing chains into the crystalline region, known as co-crystallization, has been show by a number of researchers, though its significance compared to the other forces acting on the interface are unknown [5, 99-101].

2.6 Temperature Measurements

The temperature of the filament within the nozzle is known to vary with respect to both location and time because FFF nozzles are asymmetrically heated by a single cartridge heater located in the hot end assembly while relatively cold filament is introduced into the extruder [3]. Osswald et al. studied nonisothermal melts by assuming the melt was restricted to a thin film at the tip of the nozzle [1]. This case applies for high feed rates (according to the paper about 0.25 mm/s) where thermal conduction prior to the filament reaching the tip is negligible. This model was capable of factoring in the initial temperature, heater temperature, applied force, nozzle angle, capillary length and diameter, and the rheological properties of the material for applied forces up to 40N. As stated by the authors, further work should be done to extend the model to account for shear thinning at higher forces as well as to account for heating from the side of the nozzle. Mackay et al. presented a dimensionless number based on a Péclet number to determine the minimum printing temperature at a given printing speed [2]. ABS, PLA, and a PLA/polyhydroxy butyrate copolymer were tested at temperatures ranging from 245-145 °C by increasing the printing speed until failure. After accounting for the nozzle diameter and measuring the maximum force for each filament, all the polymers and testing conditions fit well to a single curve. More advanced FFF models account for variations with respect to location using finite element analysis; however, these have limited capacity to account for transient in-situ variations.

For the vast majority of FFF systems, however, the only available experimental temperature information is provided by a single thermistor located on the side of the hot end assembly. This measurement determines variation in temperature with respect to time at the thermistor but lacks locational temperature dependence in the polymer melt. Furthermore, since the thermistor is located at the side of the nozzle rather than within, the variation with respect to time at the thermistor is not necessarily representative of the polymer melt due to thermal lag as a function of filament feed rate. Some researchers have used infrared cameras to observe the temperature of the nozzle during printing, however, this method is limited to only measuring the temperature at the surface of the nozzle [102]. To the best of the authors' knowledge, no empirical data on the temperature of the filament within FFF nozzles during printing has been measured.

2.7 Pressure Measurements and Theory

Similarly, there is a significant technical challenge of measuring the pressure in the small nozzle channel. To the best of the authors' knowledge, no directly measured empirical data has been reported regarding the pressure inside FFF nozzles [103]. Multiple groups have estimated the pressure drop within extruders of various shapes based on the inlet velocity of the filament. Ramanath et al. used FEA as well as mathematical modelling to calculate pressure drop during polycaprolactone (PCL) extrusion as a function of the internal angle of the extruder and the nozzle diameter. FEA results showed that at an extruder temperature of 333 K and filament velocity of 1.1 mm/s, the pressure drop through a curved extruder approximately 120 mm long with a nozzle diameter of 0.4 mm and angle of 20° was approximately 1.2 MPa. This decreased to approximately 0.9 MPa for an extruder angle of 70° and increased to a value of approximately 2.7 MPa for a nozzle diameter of 0.25 mm. The mathematical models showed a similar trend but approximately 20% lower pressure values; which was attributed to the FEA simulation parameters chosen [104]. Mostafa et al. also used FEA to model pressure drop in ABS-iron composite filaments. Using a extruder temperature of 543 K, filament velocity of 1 mm/s, and nozzle diameter of 0.3 mm the pressure drop in the mm curved extruder was 1.95 MPa [105]. Firoz ran FEA simulations of a straight 15 mm extruder with a nozzle diameter of 0.4 and nozzle length of 1.5 mm at a flow rate of 2.29 mm^3/s. He found that for a thermoplastic material reinforced with ceramic particles (PZT/ECG9) at 313.15 K, the pressure drop was approximately 1.8 MPa and for ABS at 533 K the pressure drop was approximately 1.1 MPa [106]. Recent studies have further inferred pressure drop, and subsequently viscosity based on filament feed rates, based on power fed to the FFF nozzle heaters and assumptions about the heat transfer in the heated block assembly [107]. Heywood has reported the potential to measure the pressure in FFF nozzles using a load cell by measuring the force applied to the filament and calculating the pressure from the force measurement [108]. However, this measurement can be challenging to account for solid filament friction, potential annular backflow or filament buckling, and changing dynamic conditions in the extruder nozzle.

Theoretical pressure is usually calculated based on the average flow rate using equations derived for flow through a die by Michaeli and adapted for FFF nozzles by Bellini *et al.* (Eqs. 2.52-55) [109, 110].

$$P_1 = 2L_1\left(\frac{Q(m+3)}{\pi f r_1^{m+3}}\right)^{\frac{1}{m}} \tag{2.52}$$

$$P_2 = \frac{m}{3 * tan\left[\frac{\theta}{2}\right]}\left(\frac{1}{D_2^{\frac{3}{m}}} - \frac{1}{D_1^{\frac{3}{m}}}\right)\left(\frac{Q}{\pi f}(m+3)2^{m+3}\right)^{\frac{1}{m}} \tag{2.53}$$

$$P_3 = 2L_2\left(\frac{Q(m+3)}{\pi f r_2^{m+3}}\right)^{\frac{1}{m}} \tag{2.54}$$

$$P = P_1 + P_2 + P_3 + 101.3\ kpa \tag{2.55}$$

where P_1, P_2, and P_3 are the pressure drops in the 1st, 2nd, and 3rd sections of the nozzle respectively; L_1, D_1, and r_1 are the length, diameter, and radius of the liquefier (section 1); L_2, D_2, and r_2 are the length, diameter, and radius of the extruder (section 3); and θ is the angle of the nozzle. Additionally, Q is the volumetric flow rate through the nozzle, and m and f are material constants equal to $1/n$, and $(k \exp\left(\frac{a}{RT}\right))^{-1/n}$ respectively. While these equations are commonly used, there has been no experimental validation of their accuracy in FFF applications.

References

[1] R. Wool, B. L. Yuan, and O. McGarel, "Welding of polymer interfaces," *Polymer Engineering & Science,* vol. 29, no. 19, pp. 1340-1367, 1989.

[2] P.-G. de Gennes, "Reptation of a polymer chain in the presence of fixed obstacles," *The journal of chemical physics,* vol. 55, no. 2, pp. 572-579, 1971.

[3] L. Bastien and J. Gillespie, "A non-isothermal healing model for strength and toughness of fusion bonded joints of amorphous thermoplastics," *Polymer Engineering & Science,* vol. 31, no. 24, pp. 1720-1730, 1991.

[4] R. Pitchumani, S. Ranganathan, R. C. Don, J. W. Gillespie, and M. A. Lamontia, "Analysis of transport phenomena governing interfacial bonding and void dynamics during thermoplastic tow-placement," *International Journal of Heat and Mass Transfer,* vol. 39, no. 9, pp. 1883-1897, 1996/06/01/ 1996.

[5] G. Jarrousse, "Self adhesion of semi-crystalline polymers between their glass transition temperature and their melting temperature," Université Pierre et Marie Curie-Paris VI, 2004.

[6] F. Yang and R. Pitchumani, "Healing of Thermoplastic Polymers at an Interface under Nonisothermal Conditions," *Macromolecules,* vol. 35, no. 8, pp. 3213-3224, 2002/04/01 2002.

[7] Q. Sun, "PhD Thesis," University of Calgary, Canada, 2004.

[8] Q. Sun, G. Rizvi, C. Bellehumeur, and P. Gu, "Effect of processing conditions on the bonding quality of FDM polymer filaments," *Rapid Prototyping Journal,* vol. 14, no. 2, pp. 72-80, 2008.

[9] C. Bellehumeur, L. Li, Q. Sun, and P. Gu, "Modeling of bond formation between polymer filaments in the fused deposition modeling process," *Journal of Manufacturing Processes,* vol. 6, no. 2, pp. 170-178, 2004.

[10] J. Thomas and J. Rodríguez, "Modeling the fracture strength between fused deposition extruded roads," in *Proceedings of the 11th Solid Freeform Fabrication Symposium*, 2000, pp. 16-23.

[11] S. Giannitelli, D. Accoto, M. Trombetta, and A. Rainer, "Current trends in the design of scaffolds for computer-aided tissue engineering," *Acta biomaterialia,* vol. 10, no. 2, pp. 580-594, 2014.

[12] S. Eshraghi and S. Das, "Mechanical and microstructural properties of polycaprolactone scaffolds with one-dimensional, two-dimensional, and three-dimensional orthogonally oriented porous architectures produced by selective laser sintering," *Acta biomaterialia,* vol. 6, no. 7, pp. 2467-2476, 2010.

[13] H. A. Almeida and P. J. Bártolo, "Numerical simulations of bioextruded polymer scaffolds for tissue engineering applications," *Polymer International,* vol. 62, no. 11, pp. 1544-1552, 2013.

[14] J. W. Jung *et al.*, "Evaluation of the effective diffusivity of a freeform fabricated scaffold using computational simulation," *Journal of biomechanical engineering,* vol. 135, no. 8, p. 084501, 2013.

[15] K. C. Yan, K. Nair, and W. Sun, "Three dimensional multi-scale modelling and analysis of cell damage in cell-encapsulated alginate constructs," *Journal of biomechanics,* vol. 43, no. 6, pp. 1031-1038, 2010.

[16] M. Dal, P. Le Masson, and M. Carin, "A model comparison to predict heat transfer during spot GTA welding," *International Journal of Thermal Sciences,* vol. 75, pp. 54-64, 2014.

[17] A. Gleadall, I. Ashcroft, and J. Segal, "VOLCO: A predictive model for 3D printed microarchitecture," *Additive Manufacturing,* vol. 21, pp. 605-618, 2018.

[18] A. D'Amico and A. M. Peterson, "An adaptable FEA simulation of material extrusion additive manufacturing heat transfer in 3D," *Additive Manufacturing,* vol. 21, pp. 422-430, 2018/05/01/ 2018.

[19] P. V. O'neil, *Advanced engineering mathematics*. Cengage learning, 2011.

[20] D. Gaskell, *An introduction to transport phenomena in materials engineering*. Momentum Press, 2012.

[21] S.-H. Ahn, M. Montero, D. Odell, S. Roundy, and P. K. Wright, "Anisotropic material properties of fused deposition modeling ABS," *Rapid prototyping journal,* vol. 8, no. 4, pp. 248-257, 2002.

[22] M. Dawoud, I. Taha, and S. J. Ebeid, "Mechanical behaviour of ABS: An experimental study using FDM and injection moulding techniques," *Journal of Manufacturing Processes,* vol. 21, pp. 39-45, 2016.

[23] A. K. Sood, R. K. Ohdar, and S. S. Mahapatra, "Parametric appraisal of mechanical property of fused deposition modelling processed parts," *Materials & Design,* vol. 31, no. 1, pp. 287-295, 2010.

[24] C. K. Chua, K. F. Leong, and C. S. Lim, *Rapid Prototyping: Principles and Applications (with Companion CD-ROM)*. World Scientific Publishing Company, 2010.

[25] N. T. Brian and A. G. Scott, "A review of melt extrusion additive manufacturing processes: II. Materials, dimensional accuracy, and surface roughness," *Rapid Prototyping Journal,* vol. 21, no. 3, pp. 250-261, 2015/04/20 2015.

[26] T.-M. Wang, J.-T. Xi, and Y. Jin, "A model research for prototype warp deformation in the FDM process," *The International Journal of Advanced Manufacturing Technology,* vol. 33, no. 11-12, pp. 1087-1096, 2007.

[27] M. Mahesh, Y. Wong, J. Fuh, and H. Loh, "Benchmarking for comparative evaluation of RP systems and processes," *Rapid Prototyping Journal,* vol. 10, no. 2, pp. 123-135, 2004.

[28] A. Kantaros and D. Karalekas, "Fiber Bragg grating based investigation of residual strains in ABS parts fabricated by fused deposition modeling process," *Materials & Design,* vol. 50, pp. 44-50, 2013/09/01/ 2013.

[29] E. R. Fitzharris, N. Watanabe, D. W. Rosen, and M. L. Shofner, "Effects of material properties on warpage in fused deposition modeling parts," *The International Journal of Advanced Manufacturing Technology,* vol. 95, no. 5-8, pp. 2059-2070, 2018.

[30] A. Peng and X. Xiao, "Investigation on reasons inducing error and measures improving accuracy in fused deposition modeling," *Advances in Information Sciences and Service Sciences,* vol. 4, no. 5, 2012.

[31] Y. Zhang and K. Chou, "A parametric study of part distortions in fused deposition modelling using three-dimensional finite element analysis," *Proceedings of the Institution of Mechanical Engineers, Part B: Journal of Engineering Manufacture,* vol. 222, no. 8, pp. 959-968, 2008/08/01 2008.

[32] S. N. Economidou and D. Karalekas, "Optical sensor-based measurements of thermal expansion coefficient in additive manufacturing," *Polymer Testing,* vol. 51, pp. 117-121, 2016.

[33] C. Casavola, A. Cazzato, V. Moramarco, and G. Pappalettera, "Residual stress measurement in Fused Deposition Modelling parts," *Polymer Testing,* vol. 58, pp. 249-255, 2017/04/01/ 2017.

[34] M. Nazan, F. Ramli, M. Alkahari, M. Sudin, and M. Abdullah, "Optimization of warping deformation in open source 3d printer using response surface method," *Proceedings of Mechanical Engineering Research Day,* vol. 2016, pp. 71-72, 2016.

[35] M. S. Alsoufi and A. Elsyeed, "Warping Deformation of Desktop 3D Printed Parts Manufactured by Open Source Fused Deposition Modeling (FDM) System," *International Journal of Mechanical and Mechatronics Engineering,* vol. 17, no. 4, pp. 7-16, 2017.

[36] A. K. Sood, R. K. Ohdar, and S. S. Mahapatra, "Improving dimensional accuracy of Fused Deposition Modelling processed part using grey Taguchi method," *Materials & Design,* vol. 30, no. 10, pp. 4243-4252, 2009/12/01/ 2009.

[37] R. K. Sahu, S. Mahapatra, and A. K. Sood, "A study on dimensional accuracy of fused deposition modeling (FDM) processed parts using fuzzy logic," *Journal for Manufacturing Science & Production,* vol. 13, no. 3, pp. 183-197, 2013.

[38] Y. Zhang and Y. Chou, "Three-dimensional finite element analysis simulations of the fused deposition modelling process," *Proceedings of the Institution of Mechanical Engineers, Part B: Journal of Engineering Manufacture,* vol. 220, no. 10, pp. 1663-1671, 2006.

[39] N. Watanabe, M. Shofner, N. Treat, and D. Rosen, "A model for residual stress and part warpage prediction in material extrusion with application to polypropylene," in *2016 Annual International Solid Freeform Fabrication Symposium, Austin Google Scholar*, 2016.

[40] D. KOSHAL, *Manufacturing Engineer's Reference Book*. Elsevier Science, 2014.

[41] C. Dichtl, P. Sippel, and S. Krohns, "Dielectric Properties of 3D Printed Polylactic Acid," *Advances in Materials Science and Engineering,* vol. 2017, p. 10, 2017, Art. no. 6913835.

[42] K. S. Boparai, R. Singh, F. Fabbrocino, and F. Fraternali, "Thermal characterization of recycled polymer for additive manufacturing applications," *Composites Part B: Engineering,* vol. 106, pp. 42-47, 2016/12/01/ 2016.

[43] X. Luo and Z. Pei, "High crystalline poly (lactic acid) filaments for material-extrusion based additive manufacturing," ed: Google Patents, 2017.

[44] C. A. Murphy and M. N. Collins, "Microcrystalline cellulose reinforced polylactic acid biocomposite filaments for 3D printing," *Polymer Composites,* vol. 39, no. 4, pp. 1311-1320, 2018.

[45] O. S. Carneiro, A. F. Silva, and R. Gomes, "Fused deposition modeling with polypropylene," *Materials & Design,* vol. 83, pp. 768-776, 2015/10/15/ 2015.

[46] S. Xiaoyong, C. Liangcheng, M. Honglin, G. Peng, B. Zhanwei, and L. Cheng, "Experimental analysis of high temperature PEEK materials on 3D printing test," in *Measuring Technology and Mechatronics Automation (ICMTMA), 2017 9th International Conference on*, 2017, pp. 13-16: IEEE.

[47] V. Kishore *et al.*, "Additive Manufacturing of High Performance Semi-crystalline Thermoplastics and their Composites," in *Solid Freeform Fabrication Symposium*, 2016.

[48] M. L. Shofner, K. Lozano, F. J. Rodríguez-Macías, and E. V. Barrera, "Nanofiber-reinforced polymers prepared by fused deposition modeling," *Journal of Applied Polymer Science,* vol. 89, no. 11, pp. 3081-3090, 2003.

[49] W. Zhong, F. Li, Z. Zhang, L. Song, and Z. Li, "Short fiber reinforced composites for fused deposition modeling," *Materials Science and Engineering: A,* vol. 301, no. 2, pp. 125-130, 2001.

[50] H. L. Tekinalp *et al.*, "Highly oriented carbon fiber–polymer composites via additive manufacturing," *Composites Science and Technology,* vol. 105, pp. 144-150, 2014/12/10/ 2014.

[51] F. Ning, W. Cong, J. Qiu, J. Wei, and S. Wang, "Additive manufacturing of carbon fiber reinforced thermoplastic composites using fused deposition modeling," *Composites Part B: Engineering,* vol. 80, pp. 369-378, 2015/10/01/ 2015.

[52] Z. Quan *et al.*, "Additive manufacturing of multi-directional preforms for composites: opportunities and challenges," *Materials Today,* vol. 18, no. 9, pp. 503-512, 2015.

[53] S. Kumar and J. P. Kruth, "Composites by rapid prototyping technology," *Materials & Design,* vol. 31, no. 2, pp. 850-856, 2010/02/01/ 2010.

[54] R. W. Gray, D. G. Baird, and J. H. Bøhn, "Thermoplastic composites reinforced with long fiber thermotropic liquid crystalline polymers for fused deposition modeling," *Polymer Composites,* vol. 19, no. 4, pp. 383-394, 1998.

[55] J. Korpela, A. Kokkari, H. Korhonen, M. Malin, T. Närhi, and J. Seppälä, "Biodegradable and bioactive porous scaffold structures prepared using fused deposition modeling," *Journal of Biomedical Materials Research Part B: Applied Biomaterials,* vol. 101, no. 4, pp. 610-619, 2013.

[56] R. W. Gray IV, D. G. Baird, and J. Helge Bøhn, "Effects of processing conditions on short TLCP fiber reinforced FDM parts," *Rapid Prototyping Journal,* vol. 4, no. 1, pp. 14-25, 1998.

[57] N. M. DeNardo, "Additive manufacturing of carbon fiber-reinforced thermoplastic composites," Purdue University, 2016.

[58] L. J. Love *et al.*, "The importance of carbon fiber to polymer additive manufacturing," *Journal of Materials Research,* vol. 29, no. 17, pp. 1893-1898, 2014.

[59] S.-L. Gao and J.-K. Kim, "Cooling rate influences in carbon fibre/PEEK composites. Part 1. Crystallinity and interface adhesion," *Composites Part A: Applied science and manufacturing,* vol. 31, no. 6, pp. 517-530, 2000.

[60] S.-L. Gao and J.-K. Kim, "Cooling rate influences in carbon fibre/PEEK composites. Part III: impact damage performance," *Composites Part A: Applied Science and Manufacturing,* vol. 32, no. 6, pp. 775-785, 2001.

[61] C. Marco, G. Ellis, M. Gomez, and J. Arribas, "Analysis of the isothermal crystallization of isotactic polypropylene nucleated with sorbitol derivatives," *Journal of applied polymer science,* vol. 88, no. 9, pp. 2261-2274, 2003.

[62] S. Nandi and A. K. Ghosh, "Crystallization kinetics of impact modified polypropylene," *Journal of Polymer Research,* vol. 14, no. 5, pp. 387-396, 2007.

[63] M. Avrami, "Kinetics of phase change. I General theory," *The Journal of Chemical Physics,* vol. 7, no. 12, pp. 1103-1112, 1939.

[64] M. Avrami, "Granulation, phase change, and microstructure kinetics of phase change. III," *The Journal of chemical physics,* vol. 9, no. 2, pp. 177-184, 1941.

[65] A. Shiryayev, "On The Statistical Theory of Metal Crystallization," in *Selected Works of AN Kolmogorov*: Springer, 1992, pp. 188-192.

[66] L. Mandelkern, "Crystallization of Polymers," *Physics Today,* vol. 17, no. 8, pp. 52-52, 1964.

[67] E. Schulz, "B. Wunderlich. Macromolecular physics, vol. 2 crystal nucleation, growth, annealing. Academic Press New York 1976, Preis $46, 50," *Crystal Research and Technology,* vol. 12, no. 1, 1977.

[68] B. Wunderlich, *Macromolecular physics* (no. Book, Whole). New York: Academic Press, 1973.

[69] T. Ozawa, "Kinetics of non-isothermal crystallization," *Polymer,* vol. 12, no. 3, pp. 150-158, 1971.

[70] T. Liu, Z. Mo, and H. Zhang, "Nonisothermal crystallization behavior of a novel poly (aryl ether ketone): PEDEKmK," *Journal of Applied Polymer Science,* vol. 67, no. 5, pp. 815-821, 1998.

[71] X. Chen, L. Wang, Y. Liu, J. Shi, and H. Shi, "Nonisothermal crystallization kinetics of high-density polyethylene/barium sulfate nanocomposites," *Polymer Engineering & Science,* vol. 49, no. 12, pp. 2342-2349, 2009.

[72] A. Hammami, J. E. Spruiell, and A. K. Mehrotra, "Quiescent nonisothermal crystallization kinetics of isotactic polypropylenes," *Polymer Engineering & Science,* vol. 35, no. 10, pp. 797-804, 1995.

[73] J. D. Hoffman, G. T. Davis, and J. I. Lauritzen, "The rate of crystallization of linear polymers with chain folding," in *Treatise on solid state chemistry*: Springer, 1976, pp. 497-614.

[74] M. R. Kamal and E. Chu, "Isothermal and nonisothermal crystallization of polyethylene," *Polymer Engineering & Science,* vol. 23, no. 1, pp. 27-31, 1983.

[75] K. Nakamura, K. Katayama, and T. Amano, "Some aspects of nonisothermal crystallization of polymers. II. Consideration of the isokinetic condition," *Journal of Applied Polymer Science,* vol. 17, no. 4, pp. 1031-1041, 1973.

[76] A. Ziabicki and L. Jarecki, "Theoretical analysis of oriented and non-isothermal crystallization III. Kinetics of crystal orientation," *Colloid and Polymer Science,* vol. 256, no. 4, pp. 332-342, 1978.

[77] M. Takayanagi and T. Kusumoto, "Growth rate of spherulites and its dependence on crystallization temperature," *Kogyo Kagaku Zasshi,* vol. 62, pp. 587-600, 1959.

[78] R. M. Patel and J. E. Spruiell, "Crystallization kinetics during polymer processing—analysis of available approaches for process modeling," *Polymer Engineering & Science,* vol. 31, no. 10, pp. 730-738, 1991.

[79] G. Z. Papageorgiou and C. Panayiotou, "Crystallization and melting of biodegradable poly (propylene suberate)," *Thermochimica acta,* vol. 523, no. 1-2, pp. 187-199, 2011.

[80] S. Chen, J. Jin, and J. Zhang, "Non-isothermal crystallization behaviors of poly (4-methyl-pentene-1)," *Journal of thermal analysis and calorimetry,* vol. 103, no. 1, pp. 229-236, 2011.

[81] W. Dietz, "Sphärolithwachstum in Polymeren," *Colloid and Polymer Science,* vol. 259, no. 4, pp. 413-429, 1981.

[82] C. N. Velisaris and J. C. Seferis, "Crystallization kinetics of polyetheretherketone (PEEK) matrices," *Polymer Engineering & Science,* vol. 26, no. 22, pp. 1574-1581, 1986.

[83] P. Cebe, "Application of the parallel Avrami Model to crystallization of Poly (Etheretherketone)," *Polymer Engineering & Science,* vol. 28, no. 18, pp. 1192-1197, 1988.

[84] V. Ratta, "Crystallization, morphology, thermal stability and adhesive properties of novel high performance semi-crystalline polyimides," Virginia Tech, 1999.

[85] L. Mandelkern, F. A. Quinn Jr, and P. J. Flory, "Crystallization kinetics in high polymers. I. Bulk polymers," *Journal of applied Physics,* vol. 25, no. 7, pp. 830-839, 1954.

[86] A. Y. Malkin, V. Beghishev, I. Keapin, and Z. Andrianova, "General treatment of polymer crystallization kinetics—Part 2. The kinetics of nonisothermal crystallization," *Polymer Engineering & Science,* vol. 24, no. 18, pp. 1402-1408, 1984.

[87] A. Y. Malkin, V. Beghishev, I. A. Keapin, and S. Bolgov, "General treatment of polymer crystallization kinetics—Part 1. A new macrokinetic equation and its experimental verification," *Polymer Engineering & Science,* vol. 24, no. 18, pp. 1396-1401, 1984.

[88] C. R. Choe and K. H. Lee, "Nonisothermal crystallization kinetics of poly (etheretherketone)(PEEK)," *Polymer Engineering & Science,* vol. 29, no. 12, pp. 801-805, 1989.

[89] A. Hammami and A. K. Mehrotra, "Re-examination of a proposed model for nonisothermal crystallization kinetics," *Polymer Engineering & Science,* vol. 35, no. 2, pp. 170-172, 1995.

[90] Y. Mubarak, E. Harkin-Jones, P. Martin, and M. Ahmad, "Modeling of non-isothermal crystallization kinetics of isotactic polypropylene," *Polymer,* vol. 42, no. 7, pp. 3171-3182, 2001.

[91] T. Chan and A. Isayev, "Quiescent polymer crystallization: modelling and measurements," *Polymer Engineering & Science,* vol. 34, no. 6, pp. 461-471, 1994.

[92] W. L. Sifleet, N. Dinos, and J. R. Collier, "Unsteady-state heat transfer in a crystallizing polymer," *Polymer Engineering & Science,* vol. 13, no. 1, pp. 10-16, 1973.

[93] A. Greco and A. Maffezzoli, "Polymer melting and polymer powder sintering by thermal analysis," *Journal of Thermal Analysis & Calorimetry,* Article vol. 72, no. 3, pp. 1167-1174, 2003.

[94] Y. M. Boiko, G. Guérin, V. A. Marikhin, and R. E. Prud'homme, "Healing of interfaces of amorphous and semi-crystalline poly(ethylene terephthalate) in the vicinity of the glass transition temperature," *Polymer,* vol. 42, no. 21, pp. 8695-8702, 2001/10/01/ 2001.

[95] J. G. Van Alsten, S. R. Lustig, and B. Hsiao, "Polymer Diffusion in Semi-crystalline Polymers. 2. Atactic Polystyrene-d Transport into Atactic and Isotactic Polystyrene," *Macromolecules,* vol. 28, no. 10, pp. 3672-3680, 1995.

[96] R. A. Segalman, A. Jacobson, E. J. Kramer, and S. R. Lustig, "Polymer diffusion in semi-crystalline polymers using secondary ion mass spectroscopy," *Macromolecules,* vol. 37, no. 7, pp. 2613-2617, 2004.

[97] B. R. Cho and J. L. Kardos, "Consolidation and self-bonding in poly (ether ether ketone)(PEEK)," *Journal of applied polymer science,* vol. 56, no. 11, pp. 1435-1454, 1995.

[98] F. Awaja and S. Zhang, "Self-bonding of PEEK for active medical implants applications," *Journal of Adhesion Science and Technology,* vol. 29, no. 15, pp. 1593-1606, 2015.

[99] C. Frederix, P. Beauchene, R. Seguela, and J. M. Lefebvre, "Kinetics of the non-isothermal fusion-welding of unlike ethylene copolymers over a wide crystallinity range," *Polymer,* vol. 54, no. 11, pp. 2755-2763, 2013/05/09/ 2013.

[100] A. Gent, E. G. Kim, and P. Ye, "Autohesion of crosslinked polyethylene," *Journal of Polymer Science Part B: Polymer Physics,* vol. 35, no. 4, pp. 615-622, 1997.

[101] Y. Q. Xue, T. A. Tervoort, S. Rastogi, and J. Lemstra, "Welding Behavior of Semi-crystalline Polymers. 2. Effect of Cocrystallization on Autoadhesion," *Macromolecules,* vol. 33, no. 19, pp. 7084-7087, 2000/09/01 2000.

[102] J. E. Seppala, K. E. Hillgartner, C. S. Davis, and K. D. Migler, "Thermography and Weld Strength Characterization of Thermoplastic Extrusion 3D Printing," 2016.

[103] S. Rangarajan, G. Qi, N. Venkataraman, A. Safari, and S. C. Danforth, "Powder processing, rheology, and mechanical properties of feedstock for fused deposition of Si3N4 ceramics," *Journal of the American Ceramic Society,* vol. 83, no. 7, pp. 1663-1669, 2000.

[104] H. S. Ramanath, C. K. Chua, K. F. Leong, and K. D. Shah, "Melt flow behaviour of poly-ε-caprolactone in fused deposition modelling," *Journal of Materials Science: Materials in Medicine,* journal article vol. 19, no. 7, pp. 2541-2550, 2007.

[105] N. Mostafa, H. M. Syed, S. Igor, and G. Andrew, "A study of melt flow analysis of an ABS-Iron composite in fused deposition modelling process," *Tsinghua Science and Technology,* vol. 14, no. S1, pp. 29-37, 2009.

[106] M. Firoz, "Physics based modeling of filaments melting in fused deposition modeling for 3D printing," State University of New York at Buffalo, 2016.

[107] M. E. Mackay, Z. R. Swain, C. R. Banbury, D. D. Phan, and D. A. Edwards, "The performance of the hot end in a plasticating 3D printer," *Journal of Rheology,* vol. 61, no. 2, pp. 229-236, 2017.

[108] M. Heywood. (2013). *Airtripper Extruder Filament Force Sensor – Introduction* [Internet]. Available: http://airtripper.com/1338/airtripper-extruder-filament-force-sensor-introduction/

[109] A. Bellini, S. I. Güceri, U. Drexel, and E. College of, "Fused deposition of ceramics: a comprehensive experimental, analytical and computational study of material behavior, fabrication process and equipment design," Drexel University, Philadelphia, 2002.

[110] W. Michaeli, *Extrusion dies for plastics and rubber 3E: design and engineering computations*, 3rd revised ed. Carl Hanser Verlag GmbH & Co. KG, 2003.

Chapter 3: In-Situ Monitoring of Polymer Flow Temperature and Pressure in Extrusion Based Additive Manufacturing

This chapter addresses research objective 1 and is presented in the form of a manuscript submitted for publication, with the exception of the abstract and introduction which were included in the previous chapters. In particular, this chapter presents the design for a system capable of measuring the in-situ temperature and pressure within FFF nozzles and validation for the accuracy and capabilities of the system.

3.1 Experimental

3.1.1 Filament Characterization

Acrylonitrile butadiene styrene (ABS) was received from HATCHBOX in filament form with a nominal diameter of 1.75 mm ± 0.1 mm. The filament was dried for 4 hours at 80 °C in a convection oven prior to testing. After drying, some of the filament was pelletized using a 2" Killion pelletizer with a Bronco II speed controller for use in rheological testing.

Rheological testing was performed using a CEAST SR20 capillary rheometer from Instron. Data was collected at temperatures of 220, 230, and 240 °C and 10 logarithmically spaced apparent shear rates between 10 and 1000 s^{-1}. A capillary die with an L/D of 30/1 was used to reduce entrance and exit effects on the pressure [1]. After the data was collected, the apparent shear rate was corrected using the Rabinowitsch correction. The activation energy of flow at a constant shear rate was calculated prior to determining the rheological fit to a power-law model (Eq. 3.1) which ABS has been shown to fit [2].

$$\eta = k * \exp\left[\frac{E_a}{RT}\right] \dot{\gamma}_w{}^{n-1} \tag{3.1}$$

where η is the viscosity of the polymer, k is the consistency index, $\dot{\gamma}_w$ is the corrected shear rate, n is the power-law index, a is the activation energy of flow of the material, R is the gas constant, and T is the temperature [3].

3.1.2 Equipment Selection and Sensor Testing Procedure

We performed in-situ temperature and pressure experiments using an open source Monoprice Maker Select 3D printer with a modified print head. Pressure measurements were collected using a Meggitt 8540-500 absolute pressure transducer. Temperature measurements were collected using a 40-gauge Type K thermocouple with a Neoflon perfluoroalkoxy alkane (PFA) coating. An NI 9219 Universal Analog Input data acquisition system was implemented to record signals from the sensors. Additionally, a PSS-10 Barrier Strip Style Power Supply 10V external power supply was used to provide the necessary excitation voltage for the pressure transducer. The uncertainty of the thermocouples was 2.2 ℃, and the uncertainty of the transducer was 0.2% of the full-scale output (3447 kPa) or 69 kPa.

Initial tests were run using a deadtime temperature control system with a deadtime of 7 s; the default temperature control system of the printer. Modifications were made for the later tests to improve the consistency of the flow rate. The standard extruder was replaced with an adjustable Flexion retrofit kit, which was tightened as tight as possible without skipping of the motor. The nozzles were wrapped in 1/8" thick fiberglass insulation. The steps/mm in the printer setting was reduced from 96 to 14 steps/mm. The temperature control mode of the printer was switched to a proportional–integral–derivative (PID) control. The P, I, and D parameters used were 17.3, 0.66, and 113 for the custom nozzles. We extruded 100 mm of filament prior to testing to ensure that the grip on the filament was consistent.

Tests were performed by manually extruding ABS filament at 230 ℃, 235 ℃, and 240 ℃ at a flow rate of approximately 0.73 mm^3/s. Temperature and pressure measurements from each sensor was recorded during the flow rate testing taking both the average value over the entirety of each test as well as the maximum pressure and minimum temperature. In order to verify the flow rate was correct, we measured the mass of filament extruded by each test and calculated the flow rate by dividing the extruded mass by the melt density of the ABS (0.97 g/cm^3) and the extrusion time. Tests were performed on the customized nozzle without any sensors, the customized nozzle with a thermocouple, and the customized nozzle with the transducer. Three tests were performed with each nozzle and temperature, with 3 minutes between tests to allow the pressure to return to the steady state value. Additionally, the theoretical pressure was calculated based on the average flow rate using Eqs. 2.52-55.

Temperature measurements were also taken at flow rates up to 5.5 mm^3/s to measure the effect of the flow rate on the temperature throughout the nozzle. To run the printer at these speeds, the extrusion region of the nozzles used were 1.17 mm shorter than the dimensions shown in Appendix 1. Additionally, a high temperature cement and 36-gauge type K thermocouples with glass braided insulation were used due to insufficient bonding of the epoxy.

3.1.3 Nozzle Design

The standard nozzles for Monoprice Maker Select 3D Printers are 0.4 mm MK10 M7 thread nozzles. To accommodate the pressure transducer and allow for controlled placement of the temperature sensor, it was necessary to make customized nozzles. These nozzles were machined from brass blocks according to the dimensions shown in Appendix A. The nozzles were designed to match the original dimensions as closely as possible.

To avoid impingement of the transducer on the filament flow, the transducer was recess mounted in a similar design to that used in a capillary rheometer. This is demonstrated in Appendix A. To prevent polymer from solidifying on the surface of the transducer, a thin coating of Jetlube AP-1 High Temperature Multi-Purpose Grease was applied to the transducer. The thermocouples were mounted in a hollow bolt using a high temperature epoxy. These bolts were then screwed into threaded holes along the side of the nozzle. Using this method, it was possible to measure the length of the thermocouple and calculate the distance it protrudes into the flow path.

3.2 Results and Discussion

3.2.1 Rheology Measurements

For calculation of the expected pressure drop per Eqs. 2.52-55, we measured the steady shear rheology of ABS at the FFF extrusion temperatures to determine parameters for a power-law fluid model. Additionally, these rheological measurements provide a comparison to the viscosity calculated from the apparent shear rates, pressure drops, and temperatures at the FFF nozzle exit. Fig. 3.1 presents the viscosity of the ABS filament as a function of corrected steady shear rate; along with the power-law fluid model fit. ABS does not exhibit a Newtonian plateau over the range of shear rates tested, which are representative of the extrusion shear rates expected in FFF printers [4]. Therefore, use of the power-law fluid model is a reasonable approach because the material was shear thinning over the entire range of temperatures and rates measured. Given that the activation energy of flow varies with shear rate, the activation energy at a shear rate representative of the FFF had to be taken [5]. The literature value for the activation energy at a constant shear rate of 148 s^{-1} (45200 J/mol) was used as this closely matches the shear rates in the nozzle (147 s^{-1}) [6]. This value matches well with the observed activation energy of flow of our filament which was 45400 J/mol at a constant shear rate of 163 s^{-1}. The best fit of the viscosity data using this activation energy to the power-law model (Eq. 3.1) is shown in Eq. 3.2. The relative error of the viscosity model was ± 7% at the 95% confidence interval.

$$\eta = 0.128 Exp\left[\frac{45200}{RT}\right]\dot{\gamma}^{-0.459} \qquad (3.2)$$

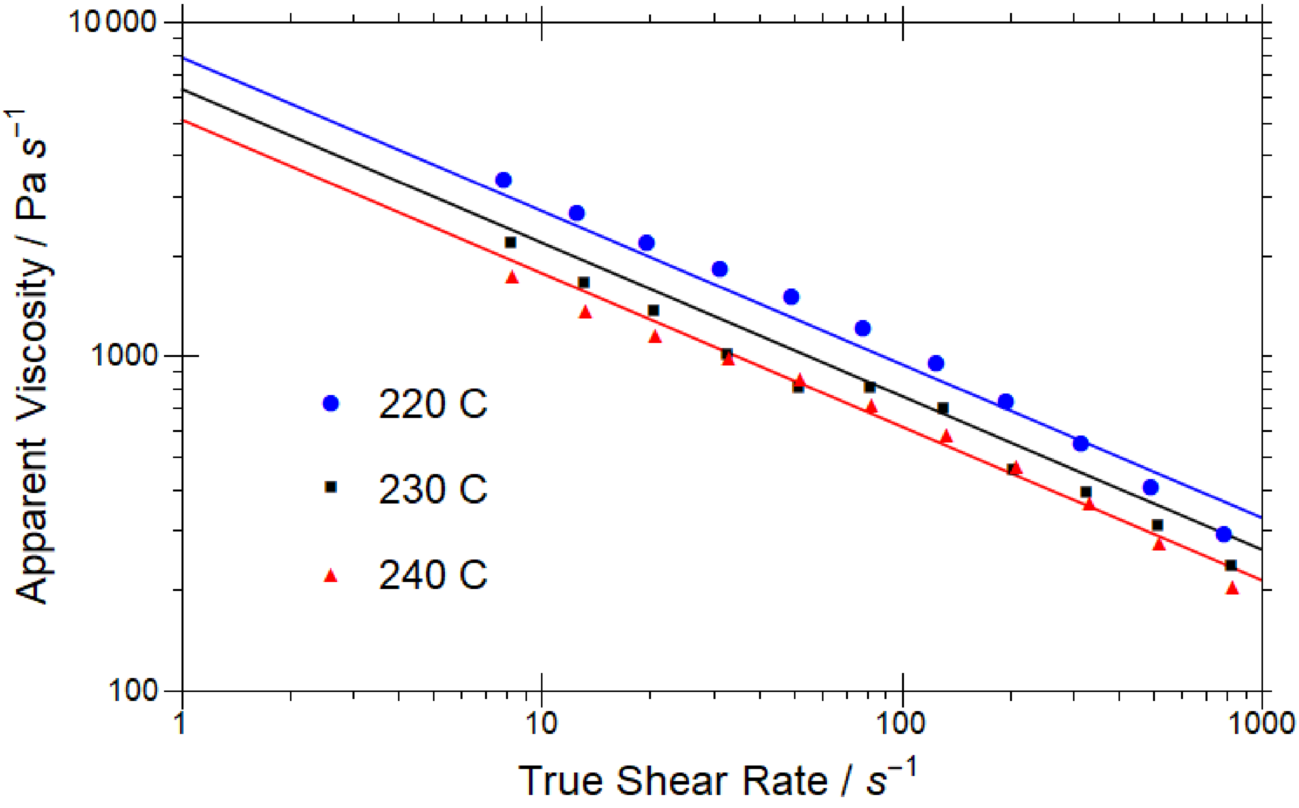

Fig. 3.1: Viscosity as a function of shear rate and temperature. The data was fit to a power-law model using an activation energy of flow at a steady shear rate of 148 s^{-1} of 45200 J/mol, which is shown for each temperature.

3.2.2 In-situ Temperature and Pressure Measurement of the Polymer Melt in the Nozzle

We first investigated the ability to capture simultaneous temperature and pressure readings of the printer, both while printing (Fig. 3.2) and while idle (Fig. 3.3) using the default printer control settings. When printing was initiated via filament feed into the hot end nozzle, the nozzle temperature dropped approximately 11 °C during extrusion. We expect that this is due to improper deadtime settings, in which the control system did not react in sufficient time to the introduction of cold filament into the hot nozzle, or due to the available power of the heater being insufficient for the extrusion rate. Upon closer inspection of the idle conditions (Fig. 3.3), both pressure and temperature fluctuate while idle. The oscillation in temperature is not unexpected as the system that regulates the temperature turns the heater off and on periodically to keep the temperature of the nozzle near the set temperature. We further observed that pressure also oscillates with the temperature. The direct correlation between the two suggests this is due to the thermal expansion of the filament. The magnitude of the variations in the temperature and pressure of the idle nozzle are approximately 2 °C and 14 kPa. This variation could be very important for materials with a low activation energy for flow or strict thermal limitations to mitigate material degradation. Additionally, these tests highlight the ability to accurately measure melt temperature in-situ which could be used to tune the control system for tighter feedback control at idle or during extrusion.

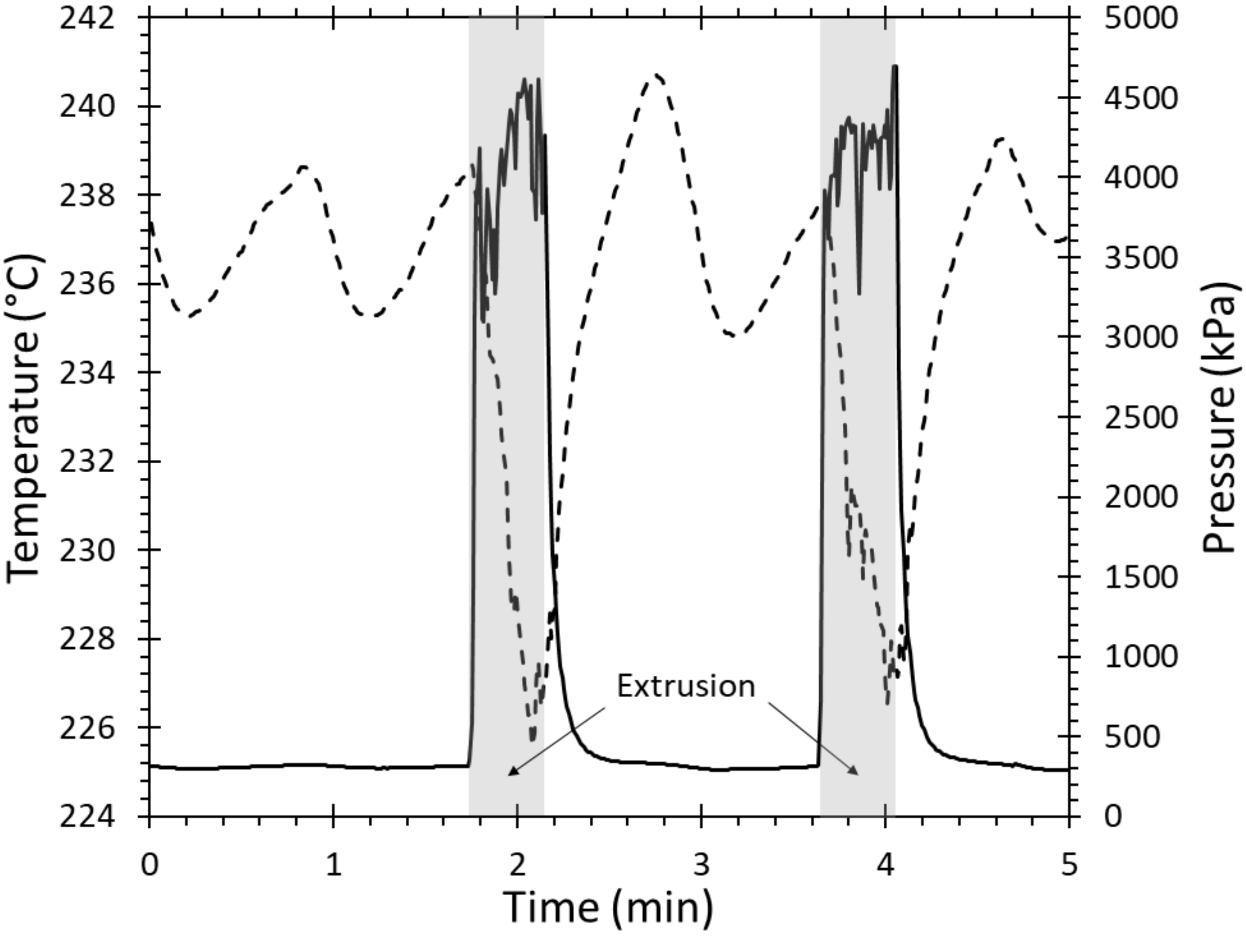

Fig. 3.2: Temperature and pressure measurements during printing and idle with two extrusion events using a poorly set deadtime temperature control system. Solid line (- -) is pressure, dashed line (—) is temperature.

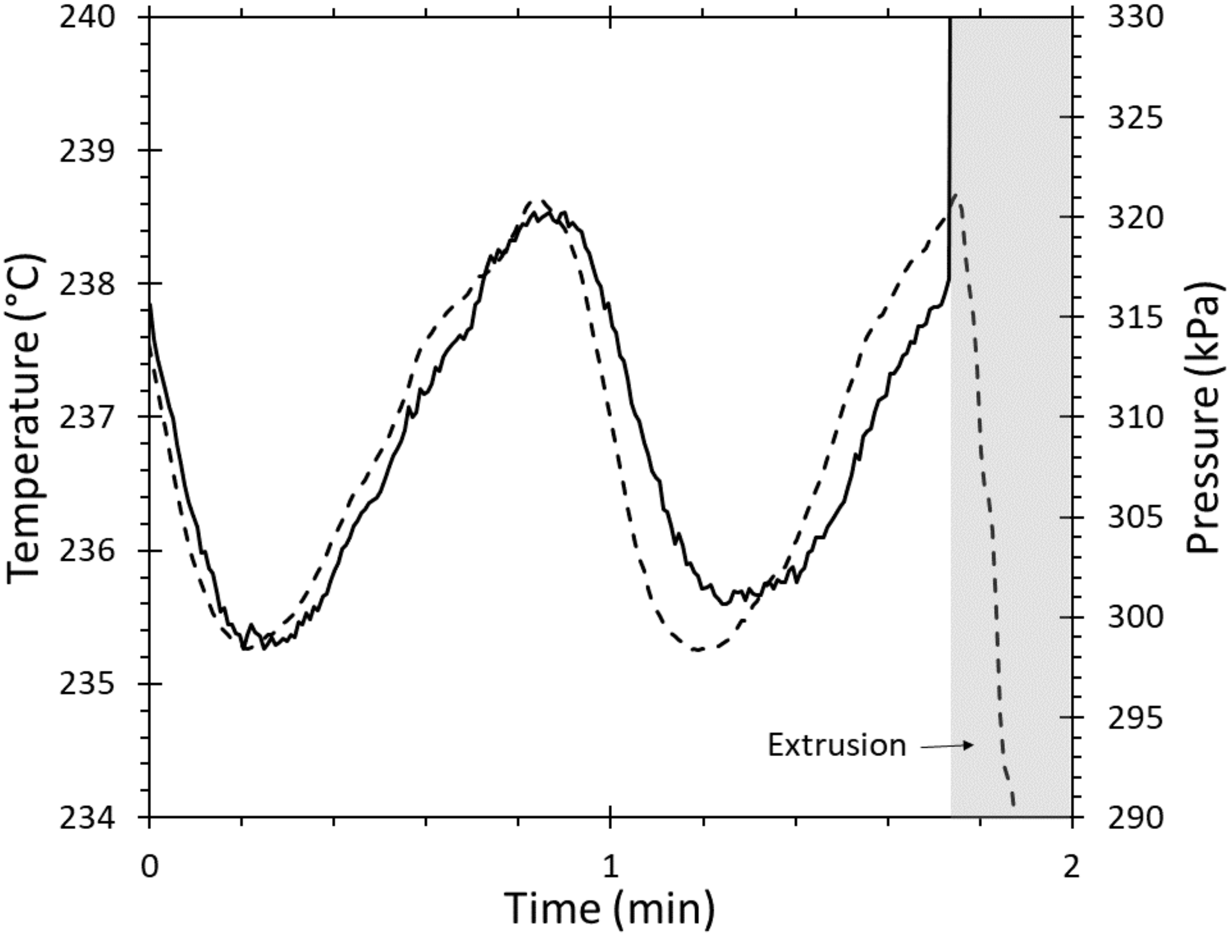

Fig. 3.3: Expanded view of idle conditions from Fig. 3.2, highlighting pressure fluctuations as the control system oscillates temperature. Beginning of extrusion is also shown starting at approximately 1:34. Solid line (___) is pressure, dashed line (- -) is temperature.

3.2.3 Comparison of Predicted vs. Measured Conditions for Modified Nozzle Configurations

In addition to the default printer settings, tests were performed after several modifications to improve the consistency of extrusion; as outlined in Section 2.2. Table 3.1 illustrates the maximum and average pressures during printing with these modifications. Additionally, theoretical pressure drop was calculated using Eq. 2.55 and the power-law model (Eq. 3.2). This data demonstrates a significant variation in pressure over the course of the printing process; with the maximum pressure exceeding the average pressure by as much as 13%. The distribution of this variation in pressure during extrusion is illustrated in Fig. 3.4. Despite this variation, the average pressure and viscosity match well with theoretical predications, falling well within the total relative uncertainty for the pressure predictions and viscosity calculation (22% and 35% respectively).

From Fig. 3.4, it can be seen that the pressure took approximately 10 seconds to attain maximum or baseline pressure when printing starts or ends. This behavior could cause prints with short spurts of printing to have different properties than those of an extended, steady print. Once the maximum pressure was reached, the pressure readings showed slight variation, but this is negligible compared to the total pressure. The changes in pressure during the beginning of extrusion shows a sigmoidal relationship while the pressure after extrusion more closely resembles an exponential decay. The pressure did not reach baseline until a few minutes after extrusion but the difference after only 10 seconds is less than 280 kPa. It should be noted that the baseline pressure was not atmospheric (101.3 kPa) but closer to 350 kPa. Outside of the nozzle, the transducer properly reads atmospheric pressure demonstrating that, even when idle, there is a slight residual pressure within the nozzle. This is not unrealistic as the viscous nature of the filament hinders flow at low pressure differentials. We further observed that the motor would skip when the pressure reached approximately 6900 kPa. This value would change depending on the motor but shows the maximum pressure our printer can reach. Further work needs to be done to determine if this behavior applies to other materials as well.

In addition to pressure data, the apparent viscosity in the nozzle can be calculated using the Hagen-Poiseuille equation. This is shown along with the theoretical viscosity in Table 3.1. This allows for determination of rheological information in addition to in-situ monitoring of other faults including blockages and under extrusion.

Table 3.1: Pressure and flow rate results.

Set Temperature (°C)	Flow Rate (mm^3/s)	Max Pressure (kPa ± 69 kPa)	Average Pressure (kPa ± 69 kPa)	Theoretical Pressure (kPa ± 22%)	Experimental Viscosity (Pa*s ± 35%)	Theoretical Viscosity (Pa*s ± 7%)
230	0.702 ± 0.032	3580	3150	3357	726	740
235	0.715 ± 0.008	3210	2870	3060	646	659
240	0.710 ± 0.041	2920	2610	2757	590	596

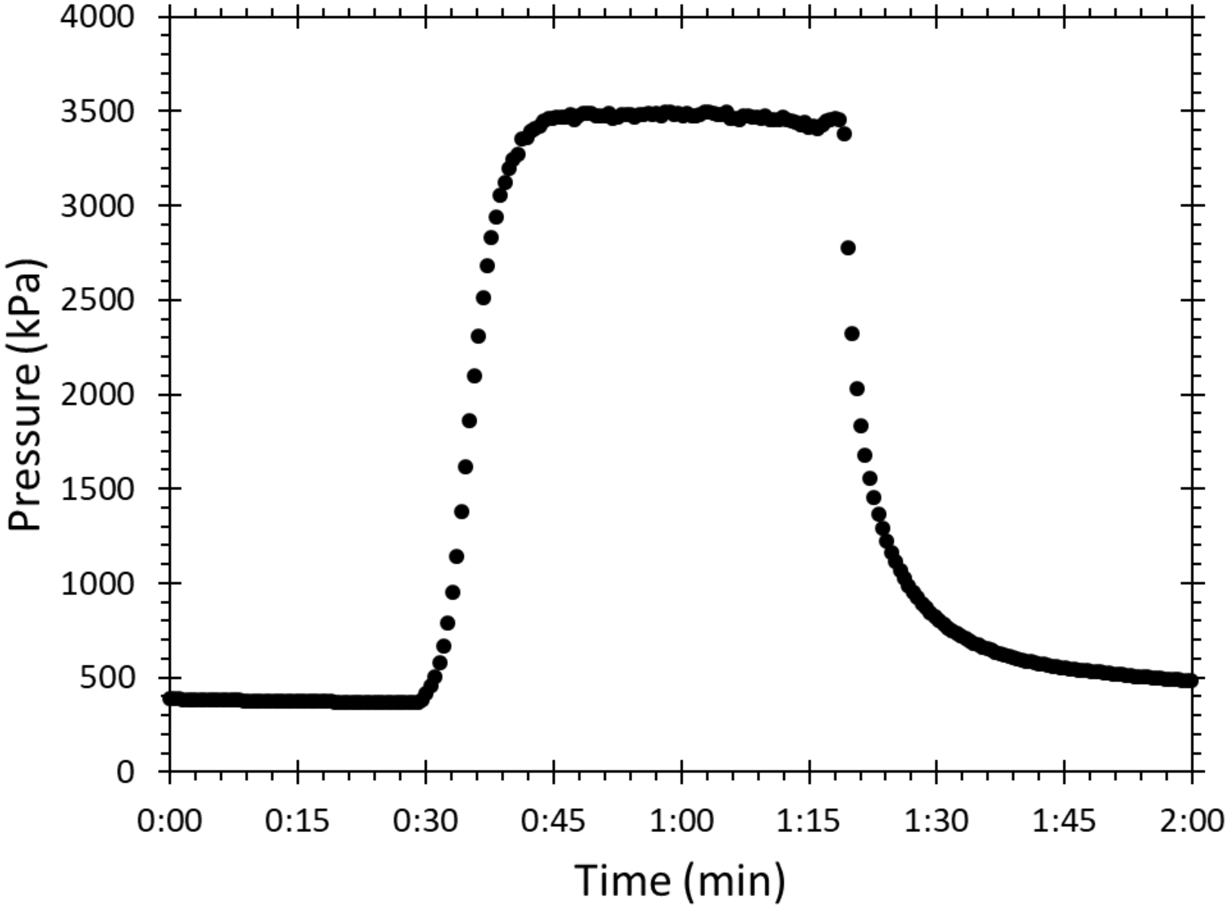

Fig. 3.4: Pressure during extrusion at 230 °C. Extrusion started at 0:30 and ended at 1:20.

After adjusting the PID parameters, no noticeable change in temperature was observed during extrusion at 0.75 mm^3/s or idle; indicating the importance of proper tuning to control the heater output and corresponding temperature consistency. At higher flow rate, however, a significant decrease in temperature developed. This is presented in Fig. 3.5 which shows the difference between the minimum temperature during extrusion and the steady state temperature as a function of flow rate. A linear increase in the temperature drop with flow rate can be clearly seen with a maximum change in temperature of 6.5 °C. This temperature drop is expected to be smaller at locations further along the nozzle. Nevertheless, the fact that the maximum obtainable flow rate was 5.5 mm^3/s rather than the theoretical maximum of 6.3 mm^3/s (calculated using Eq. 2.55 and a maximum pressure of 6900 kPa) highly suggests that there is a significant decrease in the filament temperature throughout the entirety of the nozzle. This reduction in the maximum flow rate is equivalent to a constant decrease in temperature of 3 °C. These tests highlight the ability to accurately measure melt temperature in-situ which could be used to tune the control system for tighter feedback control at idle or during extrusion. This process would be further improved by using readings from the thermocouple placed inside the polymer melt, as the direct measurements of the filament would lower the response time of the system.

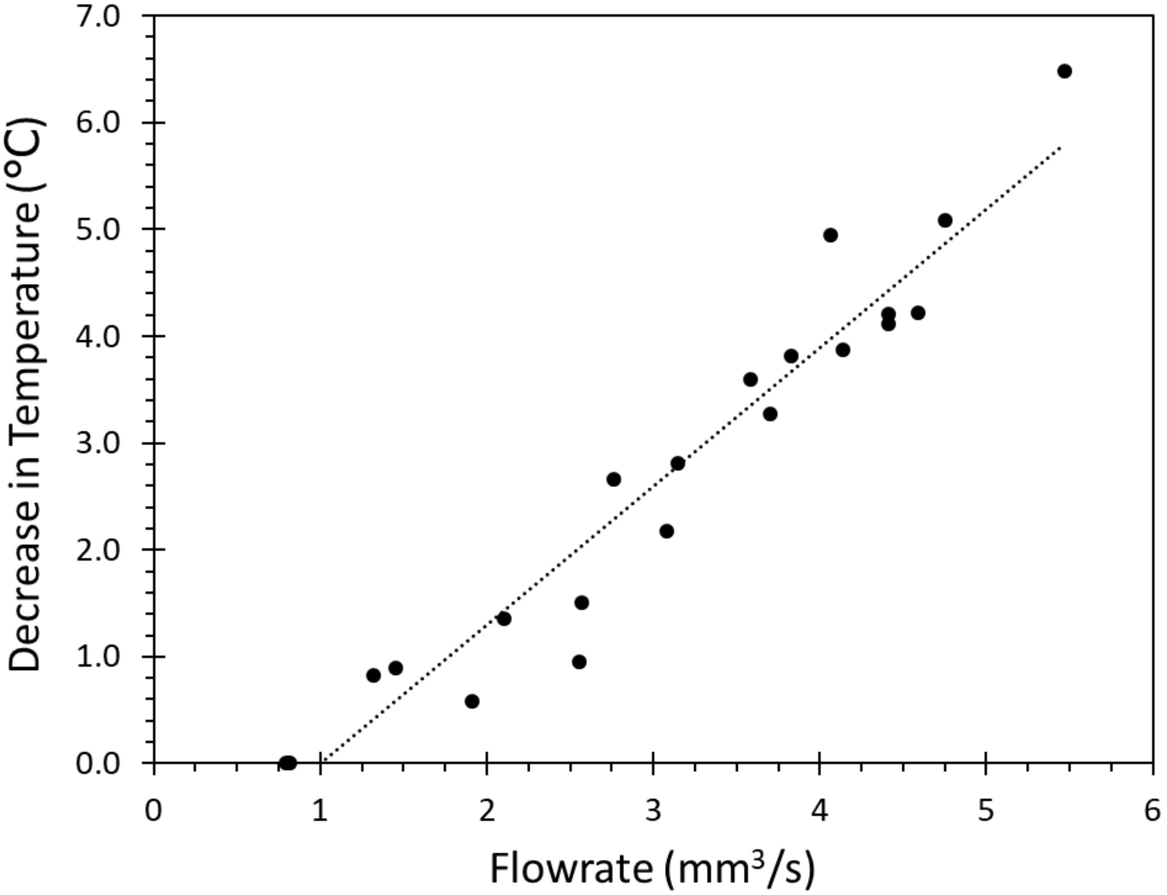

Fig. 3.5: Difference between the minimum temperature during extrusion and the steady state temperature as a function of flow rate.

3.3 Summary and Conclusions

A functional nozzle was designed, implemented, and tested in an FFF printing system. The nozzle was capable of measuring and recording the pressure and temperature distributions during extrusion. Readings showed an extensive decrease in filament temperature and significant fluctuations in pressure during printing when using an uncalibrated temperature control system. When using a calibrated temperature control system, the changes in temperature and pressure while printing were negligible, except during the initial and final stages of extrusion, where the pressure took time to build up and dissipate. Pressure readings correlated closely to predictions;

though manufacturing error lead to higher than ideal pressures at normal flow rates. While idle, temperature fluctuations were found to directly affect pressure through thermal expansion although proper PID calibration eliminated thermal fluctuations. This is the first observations of this phenomena. Based on these discoveries, the process of designing new filaments can be improved by ensuring that the PID is properly calibrated for sensitive materials. If the data from this nozzle is used in place of the thermistor, the delay between changes in temperature and the heater's response could be significantly reduced, improving the accuracy of PID calibration or potentially avoiding the need for PID calibration entirely. Furthermore, this system allows for process monitoring, something which is lacking in current FFF technology, as drops in temperature can be used to identify excessive feed rates and changes in pressure can be used to detect changes in the flow rate which lead to leaking, stringing, and inconsistent extrusion. Further work needs to be done to determine the relationship between these conditions and the variables encountered in FFF including the material, flow rate, and nozzle geometry; but this novel design is the first step towards improving our knowledge of the internal processes of FFF.

References

[1] C. W. Macosko and R. G. Larson, "Rheology: principles, measurements, and applications," 1994.

[2] Y. Q. Asif Ali Qaiser, and Rehman Rafiq, "Rheological Properties of ABS at Low Shear Rates: Effects of Phase Heterogeneity," *Malaysian Polymer Journal,* vol. 4, no. 2, pp. 29-36, 2009.

[3] H. S. Ramanath, C. K. Chua, K. F. Leong, and K. D. Shah, "Melt flow behaviour of poly-ε-caprolactone in fused deposition modelling," *Journal of Materials Science: Materials in Medicine,* journal article vol. 19, no. 7, pp. 2541-2550, 2007.

[4] E. L. Gilmer *et al.*, "Model analysis of feedstock behavior in fused filament fabrication: Enabling rapid materials screening," *Polymer,* vol. 152, pp. 51-61, 2018.

[5] G. Toth, A. Bata, and K. Belina, "DETERMINATION OF POLYMER MELTS FLOW-ACTIVATION ENERGY," *Gradus,* vol. 4, no. 2, pp. 318-322, 2017.

[6] H. Kubota, "Flow properties of ABS (acrylonitrile–butadiene–styrene) terpolymer," *Journal of Applied Polymer Science,* vol. 19, no. 8, pp. 2299-2308, 1975.

Chapter 4: Simulations of the Non-Isothermal Crystallization, Polymer Diffusion and Heat Transfer of FFF Printed Materials, and the Effect on Part Properties

This chapter addresses research objective 2 by presenting the first principle models for simulating the FFF process (Section 4.1) and applying them to a simulated PEEK part. In Section 4.3, the variation in temperature, crystallinity, degree of healing, and residual stress with time and location are explored using typical PEEK printing parameters. In Section 4.4, the printing parameters and material properties are varied to determine their effect of the part properties as well as the sensitivity of the models to these variables.

4.1 Models for Multiphysics Analysis

4.1.1 Heat Transfer

A simplified model of the FFF process was used to predict thermal history throughout FFF parts. Each line of printed material (hereafter referred to as a road) was reduced to a rectangular cross section which was in perfect contact with each adjacent road. Parts were represented by layers of roads which were all printed in the same direction and with an equal number of roads in each layer. The time required to print each layer (referred to as the layer time) was a user defined constant which could be obtained from the slicing software used. The temperature of the nozzle, printing bed, and environment as well as the heat transfer coefficient of the environment were also user defined variables and assumed to be constant throughout the printing process. Each road was added to the model under the assumption of instantaneous deposition time and that the temperature of each road was the extrusion temperature. Each road was broken down into smaller rectangular elements with dimensions dx by dy; such that there were nx and ny elements within each road in the x and y directions respectively. The heat transfer equations for discretized elements (Eqs. 2.14-17) were then applied to the elements to determine the change in temperature over time.

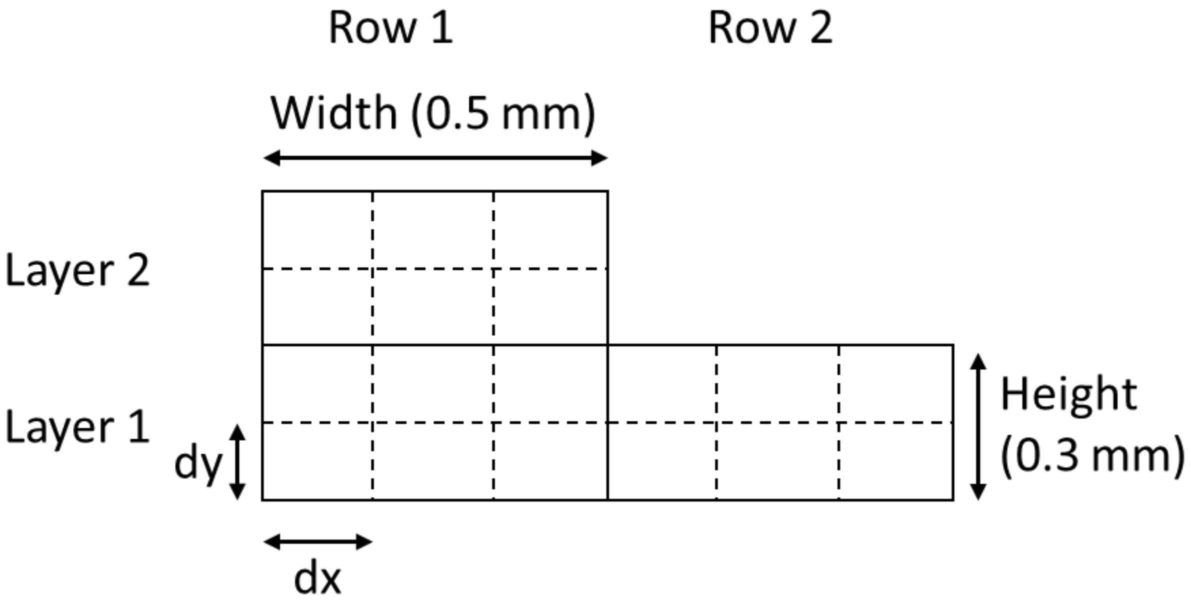

Fig. 4.1: Model of FFF cross section.

For this model, Eq. 2.8 can be simplified in several ways. First, it is assumed that $\frac{\partial^2 T}{\partial z^2} = 0$. Under this assumption, the equation reduces to Eq. 4.1.

$$\frac{dT}{dt} = \frac{K}{\mu\rho}\left(\frac{T_r + T_l - 2T}{dx^2} + \frac{T_t + T_b - 2T}{dy^2}\right) + \frac{hA}{\mu\rho dxdydz}(T_{env} - T) \qquad (4.1)$$

For the case of internal elements, A = 0 and the convection term drops out. For the case of an element on the edge, A = dx*dz or dy*dz and the value of $\frac{\partial T}{\partial x}$ or $\frac{\partial T}{\partial y}$ (aka $\frac{T_{edge} - \mathrm{T}}{dx}$) on the edge is zero. For the case of a corner node, A = (dx+dy)*dz and $\frac{\partial T}{\partial x}$ on two edges is zero. To simplify this, the value of $\frac{dT}{dt}$ can be expressed as a sum of the heat transfer in all four directions according to Eqs. 4.2-6.

$$\frac{dT}{dt} = \frac{dT}{dt}_l + \frac{dT}{dt}_r + \frac{dT}{dt}_t + \frac{dT}{dt}_b \tag{4.2}$$

where:

$$\frac{dT}{dt}_{\frac{l}{r}} = \frac{K}{\mu\rho}\left(\frac{T_r + T_l - 2T}{dx^2}\right) \tag{4.3}$$

$$\frac{dT}{dt}_{\frac{t}{b}} = \frac{K}{\mu\rho}\left(\frac{T_t + T_b - 2T}{dy^2}\right) \tag{4.4}$$

if there is an element in that direction and where:

$$\frac{dT}{dt}_{\frac{l}{r}} = \frac{h}{\mu\rho dx}(T_{env} - T) \tag{4.5}$$

$$\frac{dT}{dt}_{\frac{t}{b}} = \frac{h}{\mu\rho dy}(T_{env} - T) \tag{4.6}$$

if there is no element in that direction. Given an initial temperature of T_i, the value of T at T_{i+1} can then be found according to Eq. 4.7.

$$T_{i+1} = T_i + \left(\frac{dT}{dt}_l + \frac{dT}{dt}_r + \frac{dT}{dt}_t + \frac{dT}{dt}_b\right)dt \tag{4.7}$$

Given an upper limit of 100 w/(m^2*K) for h, lower limit of 0.04 W/(m*K) for k, and an upper limit of 0.4 mm for dx and dy, the internal elements restrict dt more according to Eqs. 2.22. Therefore, the maximum time step can be calculated according to Eq. 2.18. Given that the height of the layers is smaller than their width and that nx = ny, this can be approximated conservatively according to Eq. 4.8.

$$dt \leq 0.25\frac{\rho c_p dy^2}{k} \tag{4.8}$$

When the temperature dependency of ρ, cp, and k are accounted for, the minimum dt is smallest at low temperatures. The minimum dt was therefore calculated at the minimum possible temperature (T_{air}). Additionally, while this is the theoretical maximum time step, we found that the addition of subsequent layers introduced instabilities into the system which oscillated to extreme values. Because of this the time step was decreased slightly using a factor of 0.2 rather than 0.25 to prevent this instability.

The major assumption of this model is that the roads have a rectangular cross section. In reality, the roads are elliptical in shape. This assumption leads to a larger volume per road making the temperature changes in the model less extreme; as the thermal energy needs to heat a larger volume of material. At the same time, this assumption means that the contact between each road is greater which increases the heat flow between elements; thereby partially counteracting each other. The existence of these voids reduces the mechanical properties of the printed parts, though this can be accounted for provided the void fraction is known. Additionally, it is assumed that $\frac{\partial^2 T}{\partial z^2}$ = 0. In reality, the locations in the part which have just been printed have a larger temperature difference with the environment and therefore cool faster. Because of this, $\frac{\partial T}{\partial z}$ is larger at those areas and the heat flow into the elements in the z direction is greater that the heat flow out. This would lead to slower cooling. The significance of this compared to the heat flow in the other directions is shown to be insignificant, as highlighted in Appendix C.

Linear approximations of the temperature dependence of the density, specific heat, and thermal conductivity were included in the model to improve the accuracy of the material properties. The accuracy of the simulations could be improved by using more complicated approximations. The dependence of material properties on crystallinity was not included in this study as sufficient data was unavailable and estimates showed it has a negligible effect on heat transfer. The material properties used in this model that would vary with crystallinity include the density, specific heat, thermal conductivity. Density change was found to affect heat transfer by less than 2.7% when CTE is included in the temperature dependence of the specific heat capacity. Specific heat capacity, according to Cheng et al. [1], lowered by at most 2% at $X_{c\infty}$. As for thermal conductivity, while crystallinity is known to increase conductivity due to the ease of thermal motion through the crystalline regions, the increase in conductivity below 500 K is approximately 7% [1]. Furthermore, processes which could generate or absorb heat such as crystallization and chemical reactions and sources of radiative heat transfer to and from the part are ignored. Each of these could be added to the model as additional term of Eq. 4.2 if the rate of heat generation/loss is known.

4.1.2 Crystallization

To predict the crystallinity of prints, a combination of Velisaris and Seferis' model and the differential Nakamakura model were used. Eqs. 2.34, 2.36, and 2.37 were combined with Eq. 2.28 to account for multiple crystallization mechanisms and complicated thermal histories. To link these equations to the temperature model, they were rewritten in an incremental form (Eqs. 4.9-12) as done by Brenken et al. [2].

$$F_{vci} = 1 - exp\left[-{I_i}^{ni}\right] \tag{4.9}$$

$$I_i = \int_{t_{activation}}^{t} \left(c1i * T * exp\left[\frac{-c2i}{T - T_g + 51.6} - \frac{c3i}{T(T_{mi} - T)^2}\right]\right)^{1/ni} dt \tag{4.10}$$

$$\frac{dI_i}{dt} = \left(c1i * T * exp\left[\frac{-c2i}{T - T_g + 51.6} - \frac{c3i}{T(T_{mi} - T)^2}\right]\right)^{1/ni} \tag{4.11}$$

$$\Delta I_i = \left(c1i * T * exp\left[\frac{-c2i}{T - T_g + 51.6} - \frac{c3i}{T(T_{mi} - T)^2}\right]\right)^{1/ni} dt \tag{4.12}$$

where T is the temperature at the time step, t is the time, and $t_{activation}$ is equal to the time of deposition plus the induction time as calculated by Eq. 2.49. To reduce the amount of computations that need to be done, the model was only applied at temperatures where the value of $\Delta I/\Delta I_{max} > 10^{-6}$; where ΔI_{max} was found using the derivative of I with respect to T.

This model inherits the same assumptions as the Avrami equation; mainly that nucleation happens randomly and homogenously throughout the entirety of the amorphous phase and that growth happens evenly in all direction without being affect from the transformed material. Additionally, the non-isothermal approximation requires that “nucleation is controlled by both the free energy of short range diffusion and the free energy of formation of a nucleus” and the rate constants of nucleation and growth are the same [3]. Velisaris and Seferis’ model assumes that there are two and only two crystallization mechanisms which may not entirely encompass the complexity of the crystallization process. Furthermore, this model assumes that the weight factors of each mechanism as well as the equilibrium crystallinity are constant where in reality, they are dependent on the cooling rate. For cooling rates above 0.16°C/s, these values are fairly constant for PEEK but this assumption will need to be checked for other materials [3]. Finally, this model does not account for alignment of the polymer chains due to shear forces in the nozzle which had been shown to increase crystallization rates [4].

Melting during processing was calculated using Eq. 2.51 for each time step where the temperature was greater than the previous time step. The crystallinity was then multiplied by X_m to account for melting. When the temperature was at a maximum (determined by $T > T_{t-1}$ and $T > T_{t+1}$), values of I_1 and I_2 were recalculated according to Eqs. 4.13-16 and $t_{activation}$ was set to t. It was assumed that the melting of both phases is indistinguishable and that the crystallization rate of the partially melted crystals is the same as the initial crystallization.

$$F_{vci,t} = F_{vci,t-1}(1 - X_m) \tag{4.13}$$

$$1 - exp\left[-I_{i,t}{}^{ni}\right] = \left(1 - exp\left[-I_{i,t-1}{}^{ni}\right]\right)(1 - X_m) \tag{4.14}$$

$$exp\left[-I_{i,t}{}^{ni}\right] = (X_m) + exp\left[-I_{i,t-1}{}^{ni}\right](1 - X_m) \tag{4.15}$$

$$I_{i,t}{}^{ni} = -ln\left[X_m + (1 - X_m)\, exp\left[-I_{i,t-1}{}^{ni}\right]\right]^{1/ni} \tag{4.16}$$

4.1.3 *Degree of Healing*

Since the model assumed immediate contact and wetting of the same material, the bonding of the layers was solely dependent on healing. The average temperature of the elements on each side of the interface was used as it was assumed that thermal transport would be faster than mass transport. Furthermore, it was assumed that both sides have an equal contribution to the final degree of healing (Eq. 4.17).

$$D_h(t_h) = 0.5D_{h1}\left(t_h, \frac{T_1 + T_2}{2}\right) + 0.5D_{h2}\left(t_h, \frac{T_1 + T_2}{2}\right) \tag{4.17}$$

As in the case of symmetric bonding, the maximum degree of healing is 1; at which point the interface has reached bulk properties. Because there are no known models in literature to account for the effect of crystallinity on diffusion, a novel model was developed to account for it using two separate correction factors. First, because diffusion can only occur into amorphous regions, a factor of (1-X_c) was added to represent the volume which chains can diffuse into. Additionally, the crystalline regions and the regions around them have restricted movements such that their diffusion is negligible compared to the diffusion of the unrestricted chains. By assuming that the entire volume is restricted at maximum crystallinity, the volume of chains which are unrestricted can be accounted for using 1-X_c/$X_{c\infty}$. In total, the degree of healing is expressed by Eq. 4.18.

$$D_h = \left(0.5\left(1 - \frac{X_{c1}}{X_{c\infty}}\right)(1 - X_{c2}) + 0.5\left(1 - \frac{X_{c2}}{X_{c\infty}}\right)(1 - X_{c1})\right) * D_h\left(t_h, \frac{T_1 + T_2}{2}\right) \tag{4.18}$$

By combining Eqs. 2.5 and 4.18 and including the time dependent factors in the integral you obtain Eq. 4.19.

$$\mathrm{D_h} = \frac{0.5}{\tau_r^{*\frac{1}{4}}\exp\left[\frac{-\mathrm{E_a}}{4\mathrm{RT_{ref}}}\right]}\left(\int_0^t \frac{\left(\left(1-\frac{X_{c2}}{X_{c\infty}}\right)(1-X_{c1})+\left(1-\frac{X_{c1}}{X_{c\infty}}\right)(1-X_{c2})\right)^4}{exp\left[\frac{2E_a}{R(T_1+T_2)}\right]}d\tau\right)^{\frac{1}{4}} \quad (4.19)$$

For the bonding between layers, the total strength is the average degree of healing of each element (Eq. 4.20).

$$\mathrm{D_h}(\mathrm{t_h}, X_{c1}, X_{c2}) = \frac{0.5 * dt^{1/4}}{\tau_r^{*\frac{1}{4}}\exp\left[\frac{-\mathrm{E_a}}{4\mathrm{RT_{ref}}}\right] nx * rows}$$

$$* \left(\sum_{\tau=0}^{t}\sum_{x=1}^{nx*rows}\frac{\left(1-\frac{X_{c1}}{X_{c\infty}}\right)^4(1-X_{c2})^4+\left(1-\frac{X_{c2}}{X_{c\infty}}\right)^4(1-X_{c1})^4}{exp\left[\frac{2E_a}{R(T_1+T_2)}\right]}\right)^{\frac{1}{4}} \quad (4.20)$$

The main assumptions of this model are the effect of crystallinity on the degree of healing. In reality, the effect of crystallization on diffusion is a very complicated interaction. An example of the complex nature of this interaction is the phenomena of co-crystallization in which the crystallizing phase pulls the diffusing chains into the crystalline region. This effect should be negligible compared to the rate of diffusion though [5]. Other assumptions of the model include the Arrhenius dependency of the reptation time as well as the fact that full healing takes place in the reptation time. In reality, the chain doesn't need to move completely out of its reptation tube if the molecular weight is high enough (more than 8x the critical entanglement molecular weight). Under those conditions, the healing time is lower and requires replacing the reptation time in the previous equations with a temperature dependent welding time; where the welding time is defined as the contact time necessary to reach bulk material properties. Furthermore, initial polymer conformations such as alignment due to the extrusion process can change the time needed to heal but were not accounted for [6, 7].

4.1.4 Stress Strain Behavior

When FFF filaments cool, they shrink due to thermal expansion and crystallization. Because the bottom layer is adhered to the printing bed, however, the bottom of the filament is prevented from shrinking. This causes the filament to decrease in width and length as the height increases due to a combination of shear and tensile stresses. The length of the road in the unconstrained case can be expressed using Eqs. 4.21-26.

$$L_{shrunk} = L_{dep}(1 + CTE\Delta T)\sqrt[3]{\frac{\rho_{dep}}{\rho}} \qquad (4.21)$$

$$L_{shrunk} = L_{dep}(1 + CTE\Delta T)\sqrt[3]{\frac{\rho_a}{\rho_a + (\rho_c - \rho_a)X_c}} \qquad (4.22)$$

$$L_{shrunk} = L_{dep}(1 + CTE\Delta T)\left(1 + \left(\frac{\rho_c}{\rho_a} - 1\right)X_c\right)^{-\frac{1}{3}} \qquad (4.23)$$

or

$$L_{shrunk} = L_{dep} * Shrinkage \qquad (4.24)$$

where shrinkage is the average degree of thermal contraction throughout each layer and can be determined using Equation 4.25 or 4.26.

$$Shrinkage = (1 + CTE\Delta T)\left(1 + \left(\frac{\rho_c}{\rho_a} - 1\right)X_c\right)^{-\frac{1}{3}} \qquad (4.25)$$

$$Shrinkage = \frac{1}{nx * ny}\sum_{y=1}^{ny}\sum_{x=1}^{nx}(1 + CTE\Delta T)\left(1 + \left(\frac{\rho_c}{\rho_a} - 1\right)X_c\right)^{-\frac{1}{3}} \qquad (4.26)$$

If it is assumed that the shear strain is constant throughout a layer, the shear stress is the average of the shear stress at the top and bottom of the layer, and the shear stress linearly decreases to 0 as z approaches the center of the part, the forces can be derived according to Eqs. 4.27-29.

$$\frac{F_{tensile}}{dxdy} = E\frac{\Delta L}{L} \tag{4.27}$$

$$F_{tensile} = \int_{o}^{h} Edx\left(\frac{L - y * tan(\theta)}{L_{dep}Shrinkage} - 1\right)dy \tag{4.28}$$

$$F_{tensile} = Edx\left(\frac{Lh - \frac{1}{2}h^{2}\,tan(\theta)}{L_{dep}Shrinkage} - h\right) \tag{4.29}$$

where L is half the length of the layer, L_{dep} is half the width of the layer at deposition, h is the height of the layer, and θ is the angle of contraction of the layer caused by shear stress. Furthermore, the shear stress can be calculated using Eqs. 4.30-33.

$$\frac{F_{shear}}{dxdz} = G * tan(\theta) \tag{4.30}$$

$$F_{max} = Gdzdx * tan(\theta_{max}) \tag{4.31}$$

$$F_{shear} = \int_{o}^{L} Gdx * tan(\theta_{max}) * \left(1 - \frac{z}{L}\right)dz \tag{4.32}$$

$$F_{shear} = \frac{Gdxtan(\theta)L}{2} \tag{4.33}$$

To find the value of tan(θ) the value of F_{shear} can be estimated using Eq. 4.34.

$$F_{shear} = \frac{F_{s,top} + F_{s,bottom}}{2} \tag{4.34}$$

where the values of $F_{s,top}$ and $F_{s,bottom}$ are found by balancing the forces on the layer as shown in Fig. 4.2 and Eq. 4.35.

$$F_{tensile} = F_{s,bottom} - F_{s,top} \tag{4.35}$$

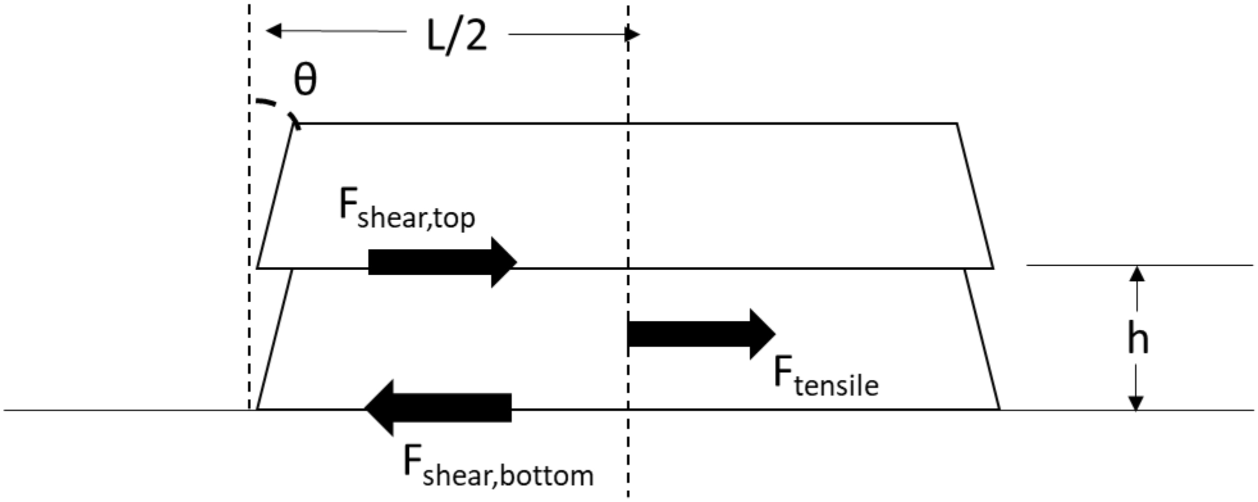

Fig. 4.2: Diagram of the cross section of a road used for stress analysis (θ is exaggerated).

For the case of the first layer, this reduces to Eqs. 4.36-40:

$$F_{s,bottom} = 2\,F_{shear} = Gdxtan(\theta)L = Edx\left(\frac{Lh - \frac{1}{2}h^2\,tan(\theta)}{L_{dep}Shrinkage} - h\right) \tag{4.36}$$

$$Gdxtan(\theta)L = Edx\left(\frac{Lh - \frac{1}{2}h^2\,tan(\theta)}{L_{dep}Shrinkage} - h\right) \tag{4.37}$$

$$\frac{Gtan(\theta)L}{E} = \frac{Lh - \frac{1}{2}h^2\,tan(\theta)}{L_{dep}Shrinkage} - h \tag{4.38}$$

$$\left(\frac{\mathrm{GL}}{\mathrm{E}} + \frac{0.5\mathrm{h}^2}{\mathrm{L_{dep}Shrinkage}}\right)\tan(\theta) = \frac{\mathrm{h}\left(\mathrm{L} - \mathrm{L_{dep}Shrinkage}\right)}{\mathrm{L_{dep}Shrinkage}} \tag{4.39}$$

$$tan(\theta) = \frac{h\left(L - L_{dep}Shrinkage\right)}{\frac{G}{E}LL_{dep}Shrinkage + 0.5h^2} \tag{4.40}$$

When additional layers are applied, the width of the bottom of these layers is not constant as they can expand and contract with the bottom layer. Rather, assuming prefect bonding with the layer below at the time of deposition, the change in w_2 is proportional to the change in the width of the top of the last layer from its width at deposition (u_1) (Eqs. 4.41-42).

$$L_2 = L * \frac{u_1(t)}{u_1} = \frac{L}{u_1}(L_1 - h * tan(\theta_1)) \tag{4.41}$$

$$u_1 = L_1 - h * tan(\theta_1) \tag{4.42}$$

where u_1 is a constant determined at the end of printing layer 1 and θ_1, L_1, and L_2 are state variables that vary with time. In the general case, this becomes Eq. 4.43

$$L_i = \frac{L}{u_{i-1}}(L_{i-1} - h * tan(\theta_{i-1})) \tag{4.43}$$

The force balance equations then are Eqs. 4.44-45.

$$F_i - F_{i+1} = Edx\left(\frac{L_i h - \frac{1}{2}h^2 \, tan(\theta_i)}{L_{dep} Shrinkage_i} - h\right) \tag{4.44}$$

$$\frac{F_i + F_{i+1}}{2} = \frac{GdxL_i}{2} tan(\theta_i) \tag{4.45}$$

where F_i is the shear forces at the bottom of layer i. Eqs. 4.44 and 4.45 can be applied to each layer giving, in the case of two layers, 4 equations and 6 variables (θ_1, θ_2, F_1, F_2, F_3, L_1, and L_2). Additionally, Eq. 4.43 can be used for all except the first layer, $L_1 = L$, and there is no shear stress at the top layer ($F_3 = 0$); giving a total of 7 equations and 7 variables.

Adding layers adds 3 variables and three equations so by calculating $u_i$at the end of each layer, a system of equations can be set up to solve for the shear and tensile stresses in each region. u_i is found using Eq. 4.46

$$u_i = L_i(i) - h * tan\big(\theta_i(i)\big) \tag{4.46}$$

The limitation of the assumption that shear strain throughout each layer is constant is that the shear strain is proportional to shear stress which must decrease to 0 at the top of the part. This means the actual parts would have more concavity with θ approaching 0 at the top of the part and therefore slightly lower stresses than predicted. Additionally, this model assumes that each road stays in the linear elastic regime. If the strain exceeds the elastic limit, the modulus of the material would be lower; leading to smaller residual stresses. The stress would be further reduced if the strain is high enough to cause yielding. Finally, polymer viscoelasticity will play a role in reducing the residual stress through relaxation. We assumed that above the Tg, relaxation prevents the buildup of stress; however, due to the low time scale, it is likely that some residual stress will remain. Another assumption of this model is that the ratio of G/E is constant. While both G and E vary greatly with temperature and crystallinity, the ratio is not as sensitive to conditions. Assuming a positive Poisson's ratio, the values of G/E are restricted to 0.33-0.5. Given that G/E has been shown to decrease with temperature [8] and the values at room temperature for PEI and PEEK are 0.34 and 0.37, changes in this ratio are negligible. Given all these sources of error, the final residual stresses may need a correction factor before they can be used to identify the likelihood of part failure. Nonetheless, the model is the first reported model capable of accounting for the cumulative buildup of stress due to deformation between printing of layers and is capable of identifying areas of higher stress as well as the effect of printing properties on the residual stress.

4.2 Simulation Settings

4.2.1 Material and Process Parameters

The default printing parameters used for the simulations were typical values for printing of PEEK filaments, shown in Table 4.1. Material properties of PEEK were obtained from literature and are shown in Table 4.2. To obtain the crystalline properties of PEEK, DSC analysis was performed on Ketaspire 820 PEEK using a DSC Q 2000 from TA instruments. Each sample was melted at 360 °C for 5 min prior to each test. Isothermal crystallization tests were run from 300-310 °C using a cooling rate of 50 °C/min, and the induction times were fit to Eq. 2.49. Nonisothermal crystallization measurements were performed using cooling rates of 15, 30, and 45

°C/min. The crystallinity as a function of time was found for each sample and analyzed using Microsoft Excel. Excel's solver function was then used to minimize the mean sum of the squares by changing the values of c11, c21, c31, c12, c22, c32 and w1. To ensure the model could account for higher cooling rates, data of samples quenched at cooling rates of 0.03154, 44.56, and 113.9 K/s, as reported by Velisaris and Seferis [3], were also included. A regression of the data indicated a mean sum of squares of 0.0001 and is shown with the DSC data in Fig. 4.3. The best fit of the crystallization model as well as the other crystalline properties of the PEEK are shown in Table 4.3.

Table 4.1: Default printing parameters for PEEK simulations.

	Parameter	Symbol	Value
Printing parameters	Width of road	width	0.5 mm
	Height of road	height	0.3 mm
	Number of roads in a layer	rows	1
	Number of layers	layers	24
	Time between printing each layer	t_{layer}	15 s
	Air temperature while printing	T_{air}	70℃ [9]
	Temperature of the printing bed	T_{bed}	160℃ [9]
	Temperature of the extruded material	T_{dep}	400℃ [9]
	Heat transfer coefficient	h	62 w/m^{2}K [10]
User defined values	Number of elements per road in the x direction	dx	0.05 mm
	Number of elements per road in the y direction	dy	0.03 mm
	Length of print	dz	76 mm
	Factor for determining dt	factor	0.2

Table 4.2: PEEK properties.

Material Property	Symbol	Value
Shear modulus	G	1.3 GPa [11]
Young's modulus	E	3.5 GPa [11]
Thermal expansion coefficient	α	-220.2 + 0.75T μm/mK [12]
Density	ρ	1.2626 g/cm^3 [11]
Specific heat	cp	1068.85 + 1.72T J/(kg*K) [13]
Thermal conductivity	k	T < 250℃ 0.219 W/(mK) T > 250℃

		0.1 + 0.00024T W/(mK) [14]
Activation energy of diffusion	E_a	57.3 kJ mol^{-1} [15]
Reptation time at the reference temperature	τ_r^*	0.11 at 400℃ [15]
Reference temperature	T_{ref}	400℃ [15]
Glass transition temperature	T_g	144℃ [3]

Table 4.3: Crystalline properties of PEEK.

Property	Symbol	Value
Density of the crystalline phase	ρ_c	1.4006 [16]
t_m	t_m	2.96*10^{16}
a	a	7.64
Equilibrium volume fraction crystallinity	$X_{vc\infty}$	0.37 [3]
Weight factor of the first mechanism	w1	0.676
Avrami exponent of mechanism 1	n1	2.5 [3]
c11	c11	2.49*10^{1} s^{-n}K^{-1}
c12	c12	574 K
c13	c13	8.29*10^{7} K^{3}
Avrami exponent of mechanism 2	n2	1.5 [3]
c21	c21	1.26*10^{9} s^{-n}K^{-1} [3]
c22	c22	4457 K [3]
c23	c23	7.25*10^{7} K^{3} [3]
Equilibrium melting temperature	T_m	662.15 [17]
Approximate temperature at which melting starts	$T_{melting}$	264℃ [18]
Peak melting temperature from DSC	T_{peak}	345℃ [18]
Intensity factor related to the sharpness of the distribution	K_m	0.965 K^{-1} [19]
Shape factor controlling the dispersion of melting temperatures lower than T_m	d	8.58 [19]

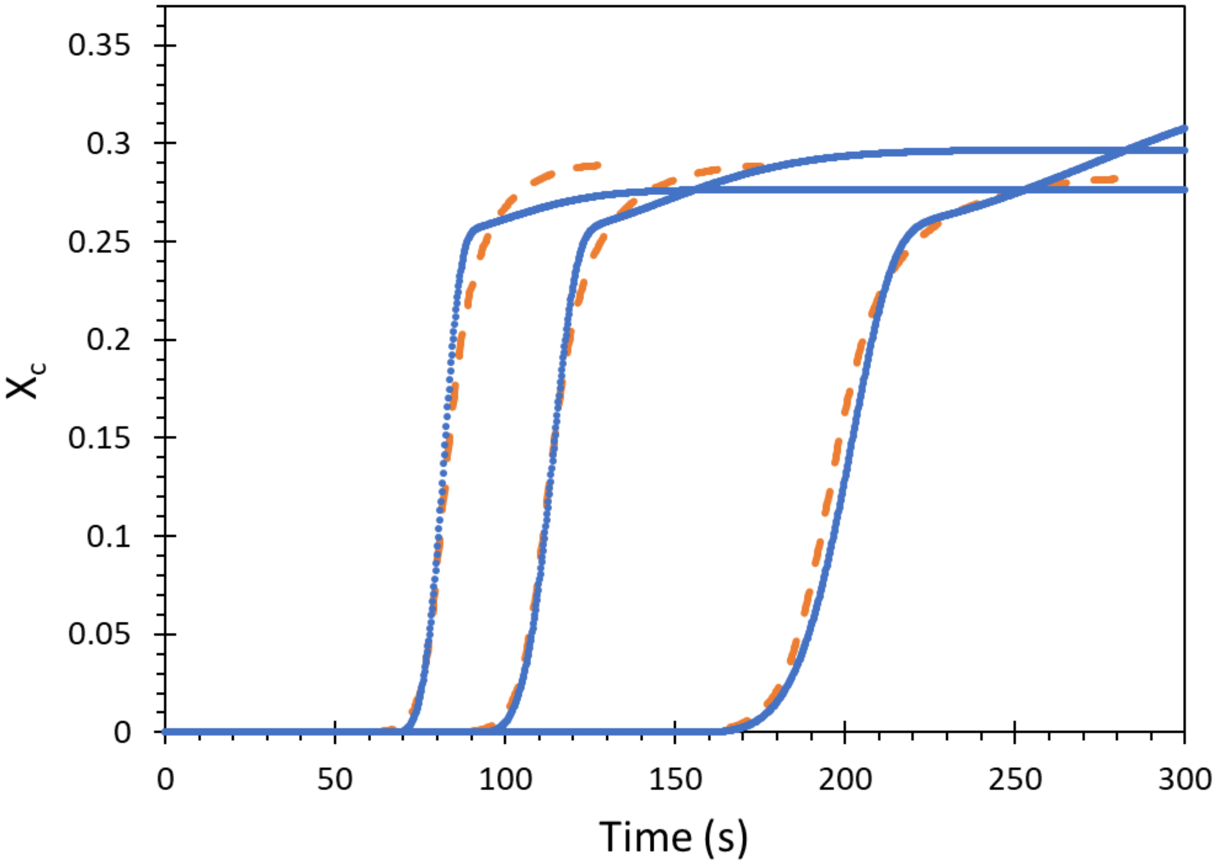

Fig. 4.3: Crystallization of ICI 450 PEEK at various cooling rates with best fit model.

4.2.2 Build Height Analysis

Because each layer increases the computation time, it is prudent to only simulate as many layers as necessary. For these simulations, two regions of interest were examined. The first region of interest was layer 1. This layer is critical for successful prints as bed adhesion is highly dependent on the printing conditions of this layer. Additionally, this layer is the least similar to the bulk part properties as it is in direct contact with the bed which affects its cooling behavior. The other region of interest is the steady state region which is sufficiently far from print bed that the cooling behavior is not affected by it. Because of this, the properties of each layer in this region are the same and represent the bulk properties of sufficiently large parts. A 40 layer print was simulated using the printing parameters in Tables 4.1-3 to determine the lowest layer in this region. We found that the final crystallinity decreased with layer number for about 20 layers and then leveled out. To ensure that the error at all points within the cross section were examined, data was collected at 6 different locations within the cross section of the layer; shown in Fig. 4.4. The crystallinity at each location and layer is shown in Fig. 4.5. The final crystallinity of layer 1 was 25.0% at all locations, 68% of the maximum crystallinity. At higher layers, the crystallinity decreased to steady state values of 18.3, 23.5, 25.0, 19.4, 24.1, and 25.0 for locations 1-6 respectively. This decrease in crystallinity is due to the layer cooling to a lower temperature which inhibits crystallization. This is excluding the upper two layers which showed lesser degrees of crystallinity due to no additional heating from subsequent layers. To achieve crystallinities within 1% of these steady state values, 22 layers were required (plus the two on top) for a total of 24 layers. This is higher than the findings of D'Amico and Peterson who found convergence in the temperature history at around 7 layers [20]. Fig. 4.6 shows the degree of healing for each layer, which exhibited a more complicated relationship with layer number. This is due to the changes in the crystallinity at the interface as a simulation run with no crystallization showed that the degree of healing decreased with layer number for more than 40 layers. Overall, the maximum degree of healing at higher layers was 51.7%. With 22 layers and two on top, the value was 0.4% lower than this value showing 24 layers is sufficient for modeling the steady state degree of healing as well. The change in the shear stress was also investigated and it was found that the shear stress increased linearly as layers were added. Only simulating 24 layers underpredicts the shear stress of taller parts but the results should be proportional to the percentage of the part simulated. Furthermore, the simulations can still be compared to one another to evaluate the effect of each printing parameter.

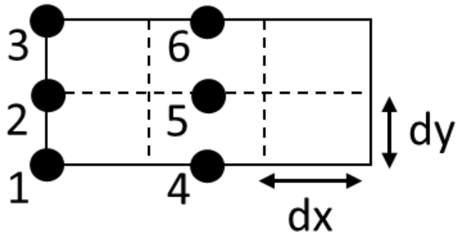

Fig. 4.4: Locations tested within each road.

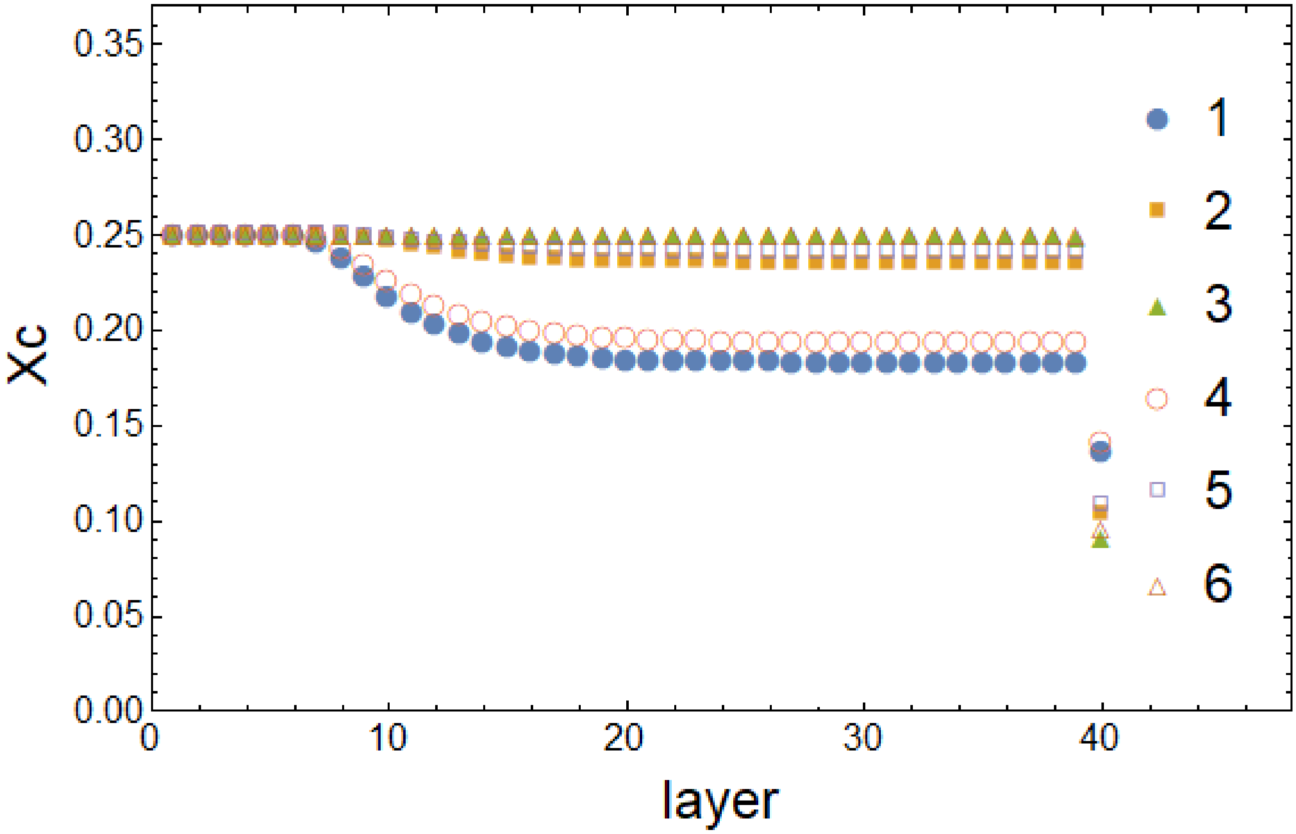

Fig. 4.5: Variation of crystallinity across layers at various locations within a road as described by Fig. 4.4.

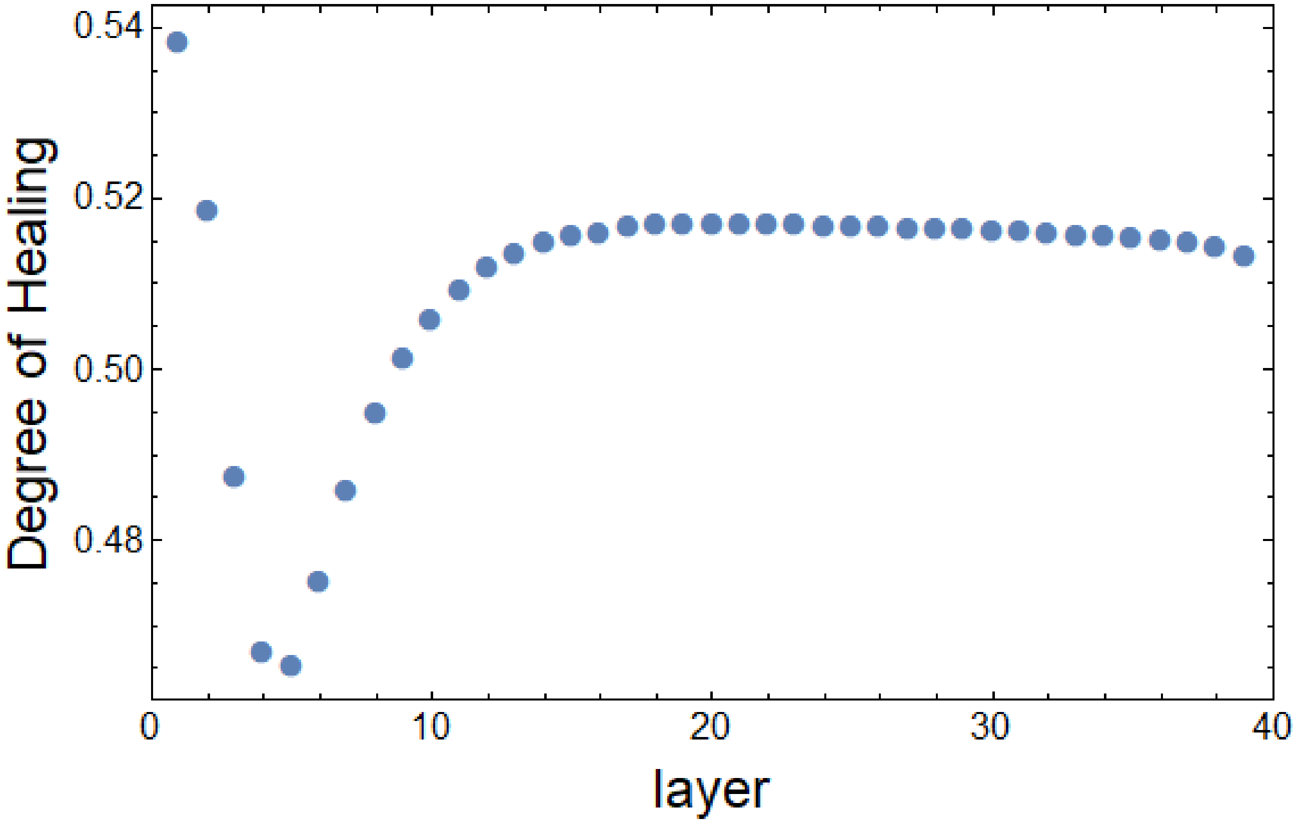

Fig. 4.6: Variation in degree of healing across layers.

4.2.3 Analysis of Maximum Element Size and Time Step

The discretization process does introduce a discretization error into the calculations. This error can be reduced by increasing the number of time steps or elements. By extrapolation to the cases of an infinite number of time steps or elements, the error in any property due to discretization of that dimension can be calculated as the difference between that property for the finite case and for the infinite case. The model $a - \frac{b}{nx}$ was used to quantify the error. These models were chosen as they match the theoretical and experimentally observed trends where the values approach a constant value as the number of elements (nx and ny) approach ∞. Tests for the necessary values of nx and ny were run with an equal number of elements in each direction (nx = ny), exploring the error in the crystallinity, degree of healing, and shear stress at the bottom of layer 1.

Overall, the effect of discretization was negligible when nx = ny = 7. The largest error in crystallinity was at location 4 in layer 22 where the error was 0.12% in layer 22. The discretization error of the degree of healing was 0.02% and 0.08% for layers 1 and 22 respectively. The error in the shear stress was 0.003 MPa which is 0.02% of the total stress.

Next the time step factor was changed to assess the error introduced by the time step discretization. The factor of 0.2 was lowered by intervals of 0.01 though no significant change was seen in Xc, D_h or the residual stress. Literature values show dt less than 0.2 s for ABS are sufficient [10]. For the initial trial, the factor of 0.2 lead to a dt of 0.17 showing good agreement with that finding.

4.3 Simulation Results for Typical Printing Parameters

4.3.1 Temperature Results

Figs. 4.7-8 show the temperature profile of layers 1 and 22 at multiple locations in the road. Bumps in the temperature profile were seen every 15s as additional layers were printed. These bumps were seen for more than 3 additional layers showing good agreement with experimental observations [21] and proving the model are capable of accounting for them. As discussed in Section 4.2.2, however, only the two subsequent layers significantly affect the part properties. The temperature profiles showed little variation with changes in the x locations but the maximum temperature upon deposition of additional layers was noticeably higher for the upper locations; as they were closer to the newly printed layer. Layer 22 showed much slower cooling rates and dropped to a lower temperature than layer 1 because it was farther from the bed and conduction to the bed was much slower. It should be noted that the Tg of PEEK is about 417 °C. This means that the bumps in temperature brought the temperature significantly above the Tg; confirming the hypothesis that crystallization and healing can continue to occur upon the addition of more layers.

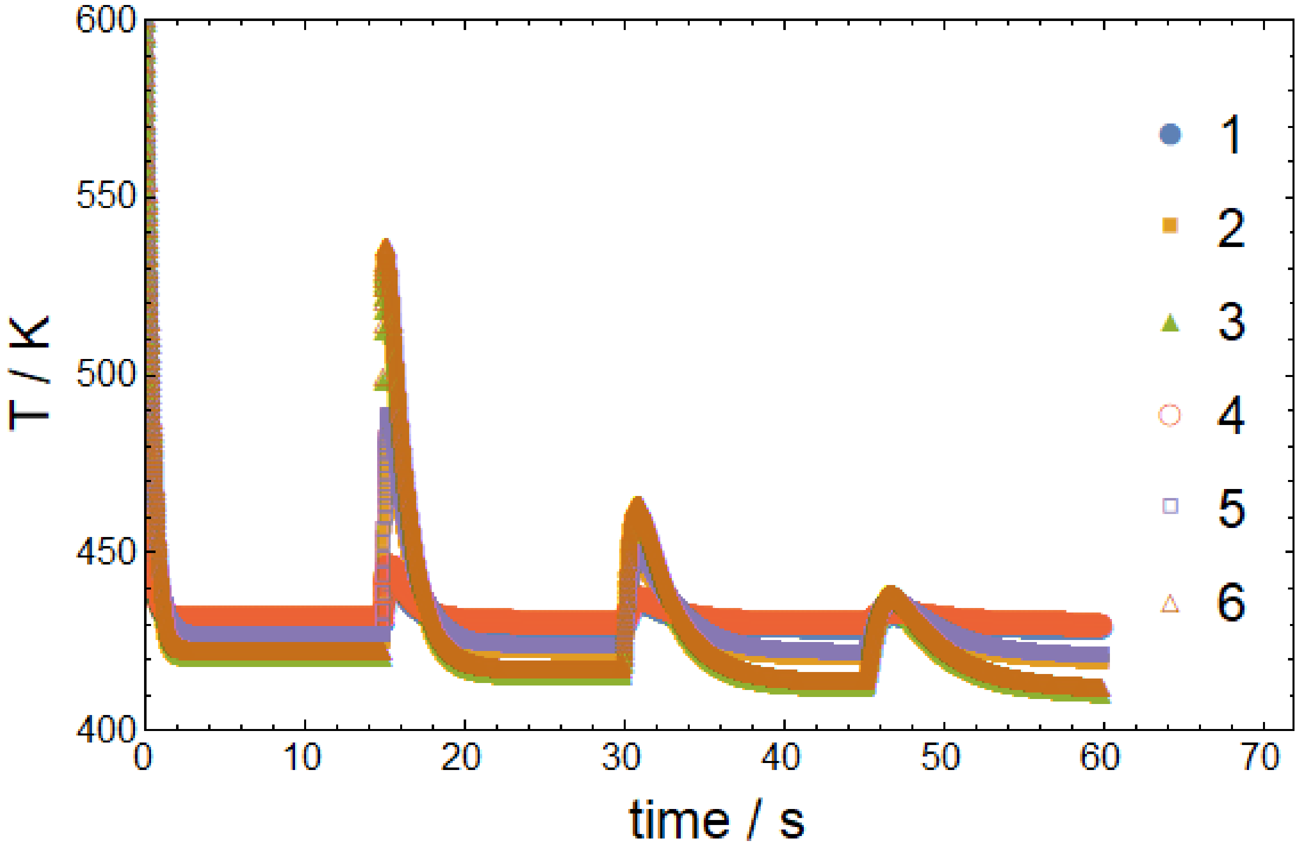

Fig. 4.7: Temperature vs time profile of layer 1 at various locations within a road as described by Fig. 4.4.

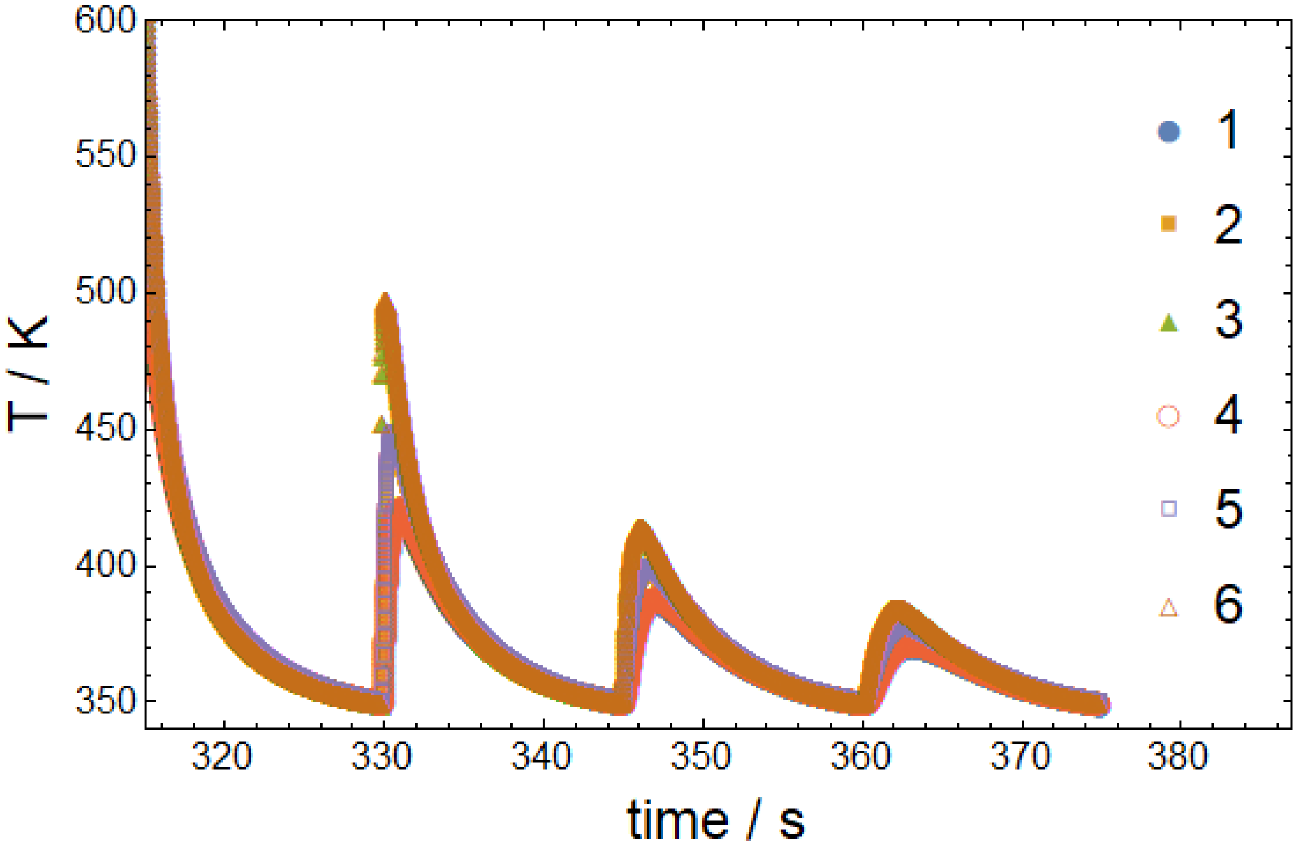

Fig. 4.8: Temperature vs time profile of layer 22 at various locations within a road as described by Fig. 4.4.

Figs. 4.9-10 show the temperature of the minimum and subsequent maximum temperature after extrusion of each layer. After about 10 layers, the values flattened out confirming that the thermal history is approaching steady state conditions. Locations at different y values showed differences in the maximum temperature of approximately 80 °C while smaller differences (~5°C) were seen due to changes in the x location. The highest maximum temperatures were at the upper locations because they were closest to subsequently deposited layers. In contrast, the minimum temperatures were highest at the lower locations which were closest to the warm bed. For layer 1, this difference in the minimum temperature was as high as 10.6 °C but reduced to less than 1 °C by layer 10. While these differences in temperature may be small, crystallization and interlayer healing are highly dependent on the temperature, so they may have a significant effect on part properties.

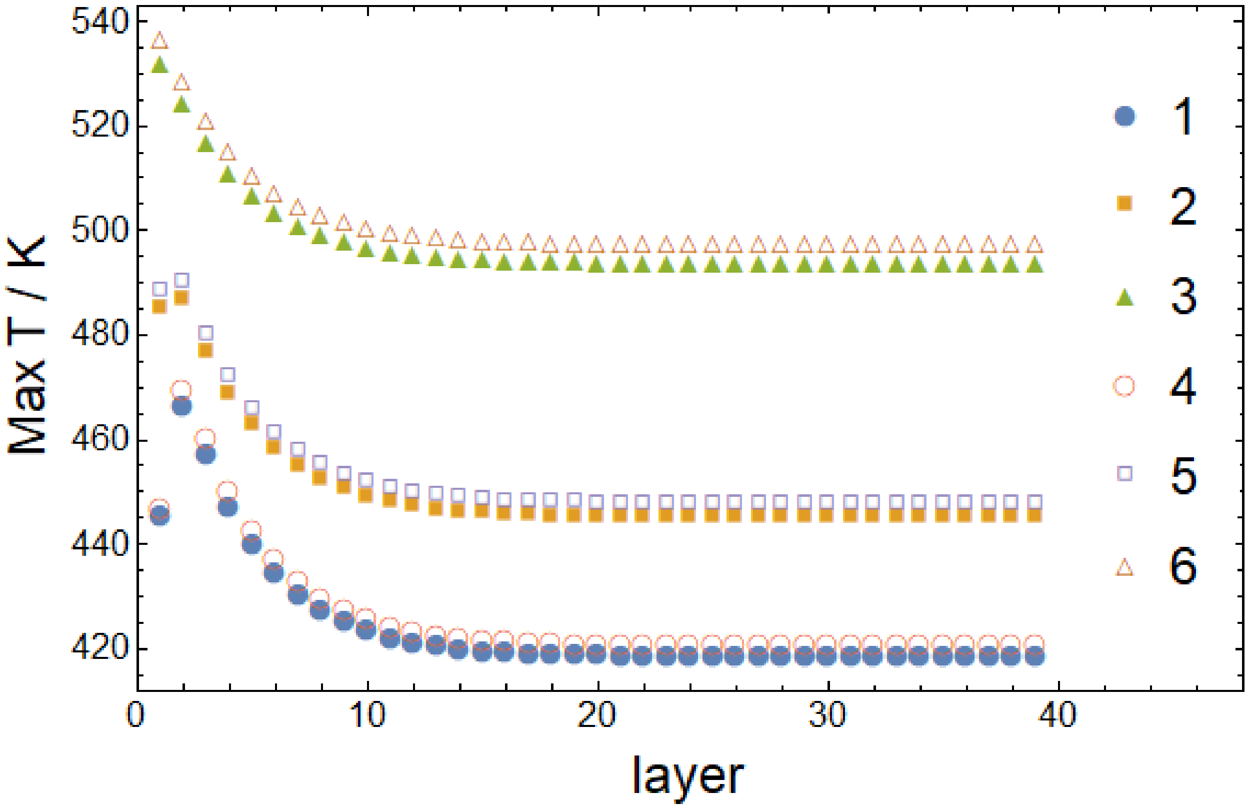

Fig. 4.9: Maximum temperature during extrusion of next layer vs layer at various locations within a road as described by Fig. 4.4.

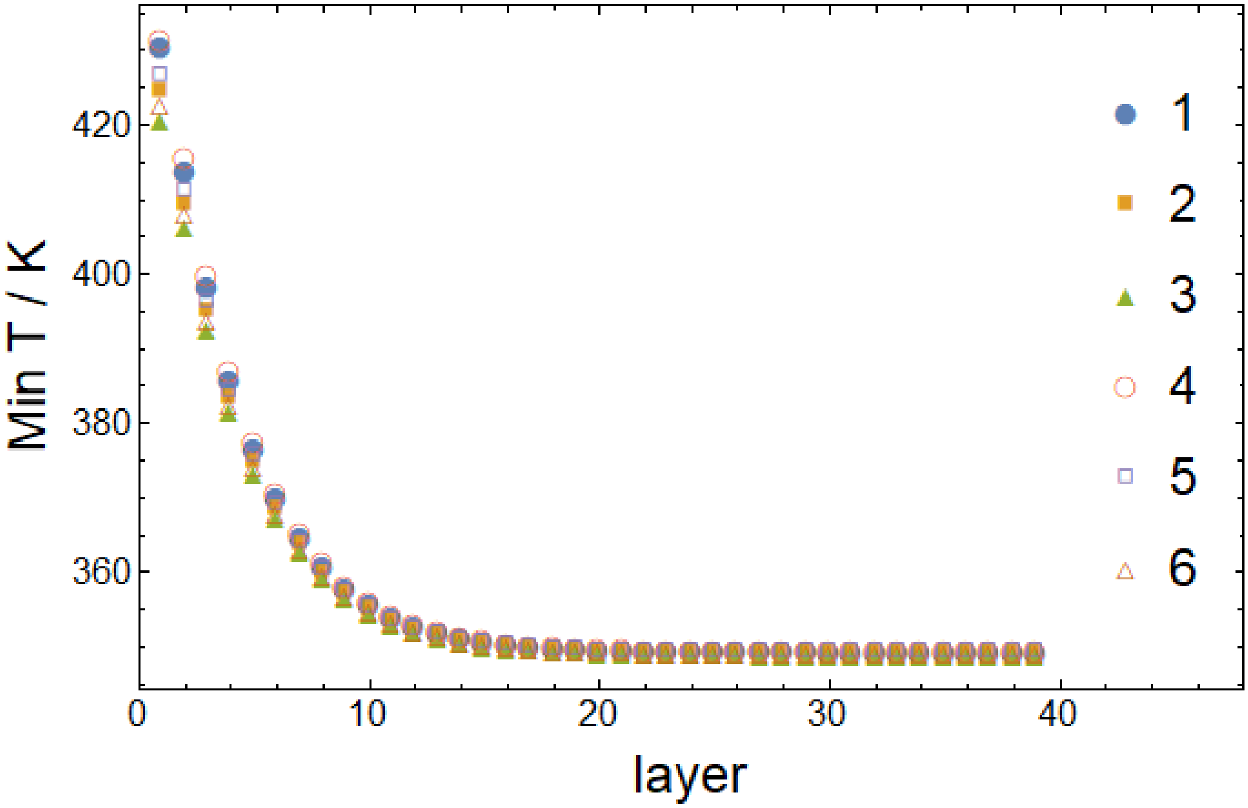

Fig. 4.10: Minimum temperature during extrusion of layer vs layer at various locations within a road as described by Fig. 4.4.

4.3.2 Crystallinity Results

Figs. 4.11-12 show the crystallization of layers 1 and 22 as a function of time. Layer 1 crystallized significantly faster showing a maximum crystallinity of 25.0% within 10 s. Layer 22, however, cooled to a significantly lower temperature so crystallization was slower and less extensive. When the next layer was deposited, further crystallization occurred, with locations 2, 3, 5, and 6 reaching the same crystallinity as layer 1 and locations 1 and 4 reaching final crystallinities of 18.4% and 19.4% respectively. This highlights the importance of modeling crystallization differences within a road as the crystallinity of locations 1 and 4 directly impacts the healing with the previous road. It should be noted that the maximum crystallinity only reached 68% of equilibrium volume fraction crystallinity. This is because the secondary crystallization method according to the crystallization model was too slow to occur during deposition. This is entirely material dependent and faster crystallizing materials could achieve maximum crystallinity.

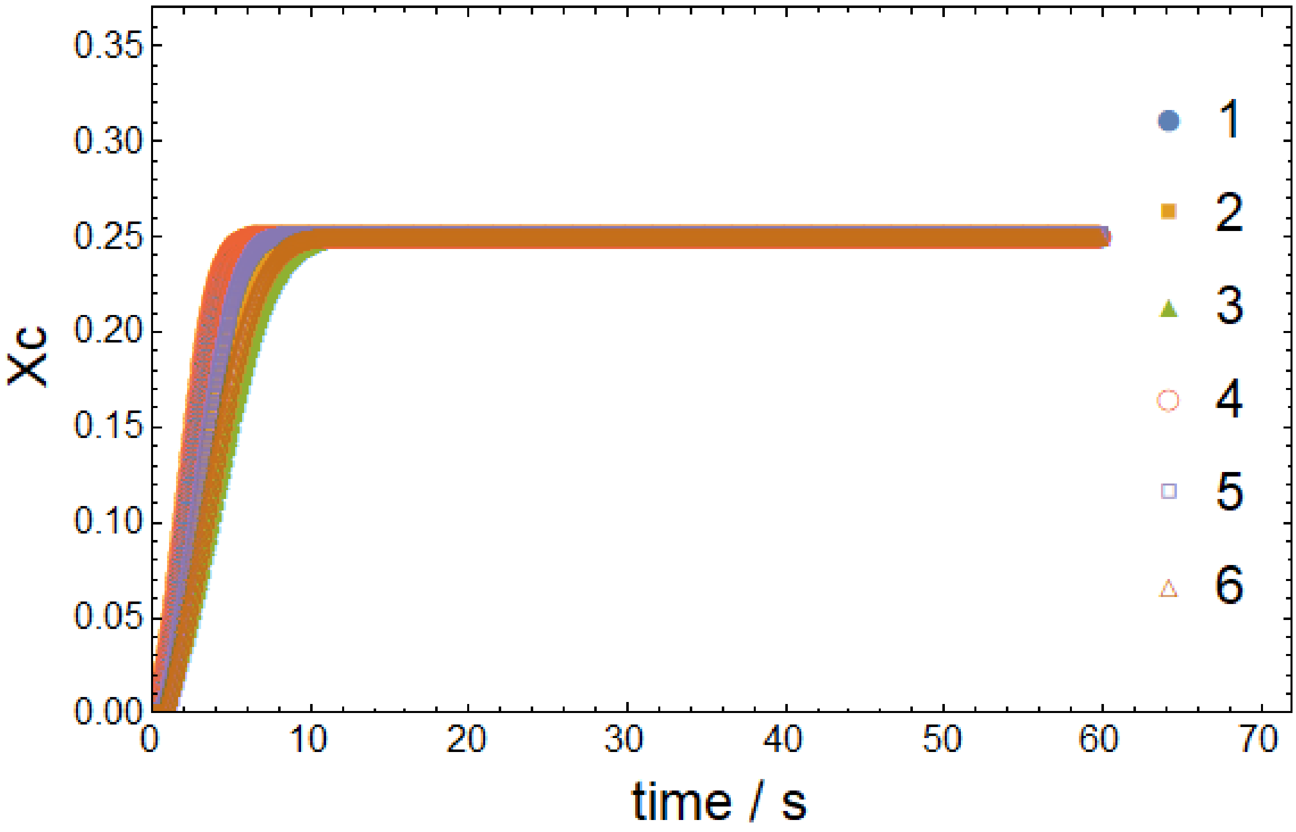

Fig. 4.11: Crystallinity vs time profile of layer 1 at various locations within a road as described by Fig. 4.4.

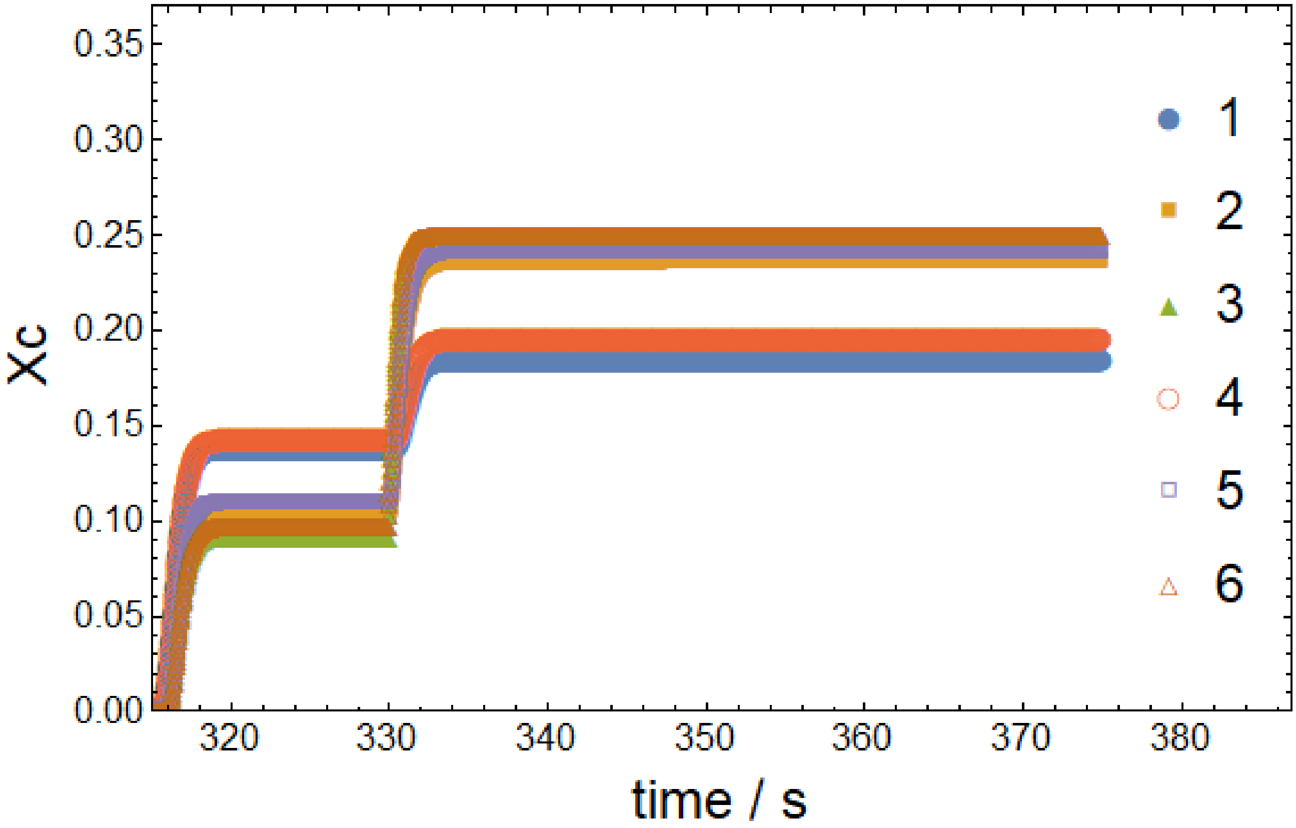

Fig. 4.12: Crystallinity vs time profile of layer 22 at various locations within a road as described by Fig. 4.4.

4.3.3 Degree of Healing Results

Fig. 4.13 shows how degree of healing increases with time. Healing took place over tens of seconds showing it continued to develop after multiple layers have been deposited. Layer 22 had a final degree of healing of 53.8%, showing a greater degree of healing than layer 1 (51.7%). This can be attributed to the delay in the crystallization of layer 22 which would prevent healing. This is supported by Fig. 4.14 which shows healing without accounting for crystallinity. When crystallization is ignored, the degree of healing was much higher, showing complete healing for layer 1 and 87.3% healing for layer 22. Given that achieving full healing in amorphous materials is challenging, the significant decrease in healing due to crystallization demonstrates the difficulties involved in printing with semi-crystalline polymeric materials.

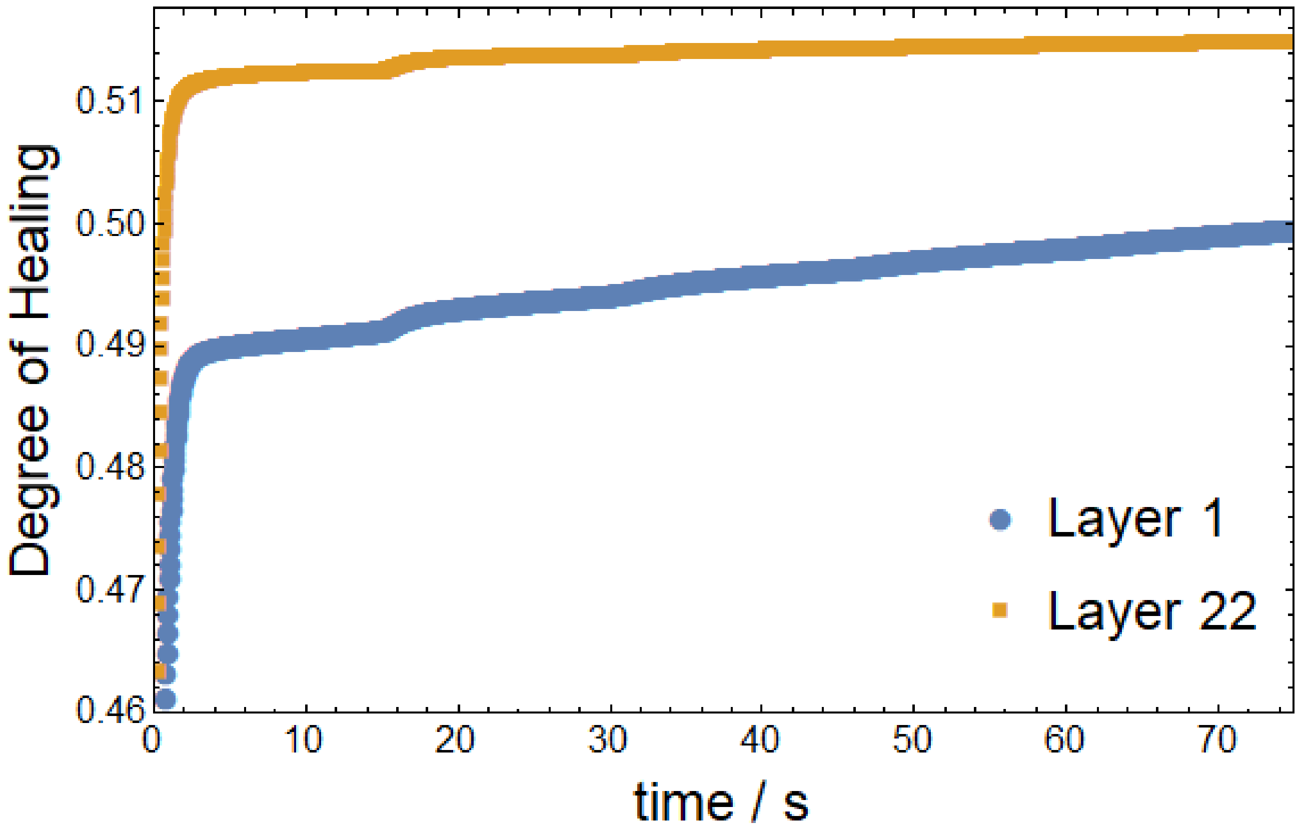

Fig. 4.13: Degree of healing vs time profile of layers 1 and 22.

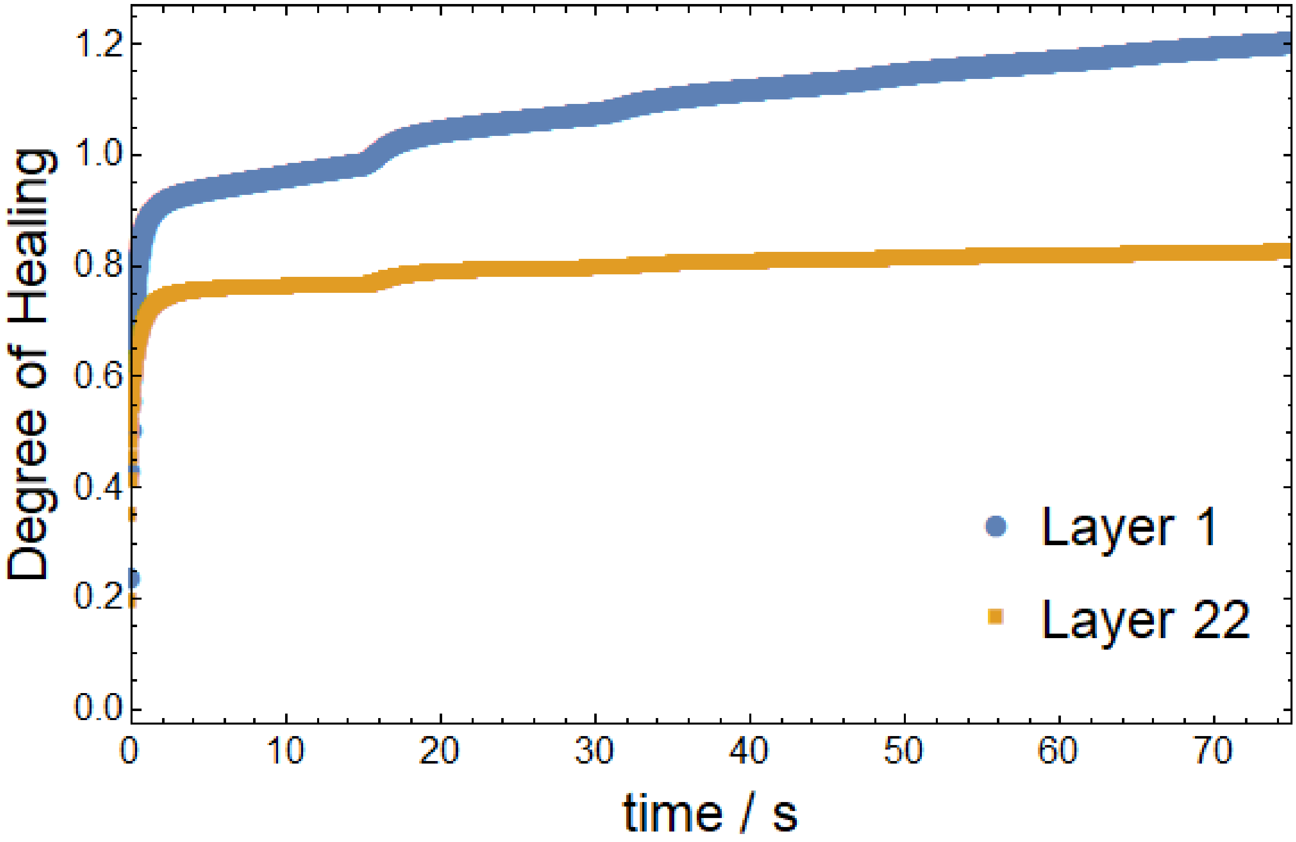

Fig. 4.14: Degree of healing vs time profile of layers 1 and 22 assuming no crystallization.

4.3.4 Residual Stress Results

Fig. 4.15 illustrates the shear stress at the bottom of each layer after printing. The stress decreased mostly linearly with a highest stress of 19.4 MPa at layer 1. This trend is further demonstrated in Fig. 4.16 where the shear stress of layer 1 increases linearly as layers are deposited. Crystallinity significantly contributed to the stress development, accounting for 44% of the total stress under these printing conditions. Complexity of a part as well as thermal fluctuations would affect these results and could lead to high stresses at higher locations; explaining why some materials crack while printing. However, for simple shapes that only decrease or stay the same in size, this relationship should apply. While the model only simulated 40 layers of deposition, both figures show a linear increase in stress with number of layers and the results could be extrapolated to more layers.

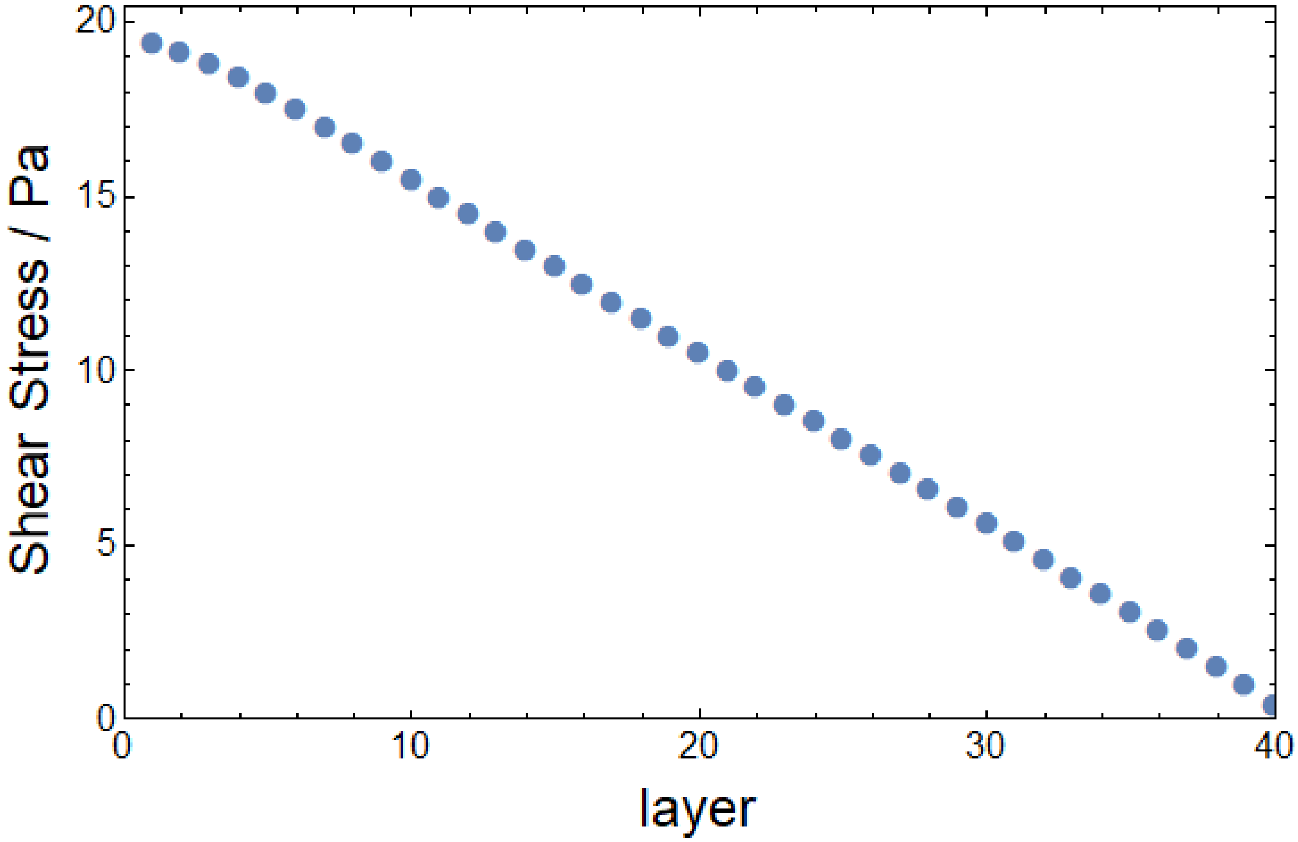

Fig. 4.15: Shear stress at the bottom of each layer after printing.

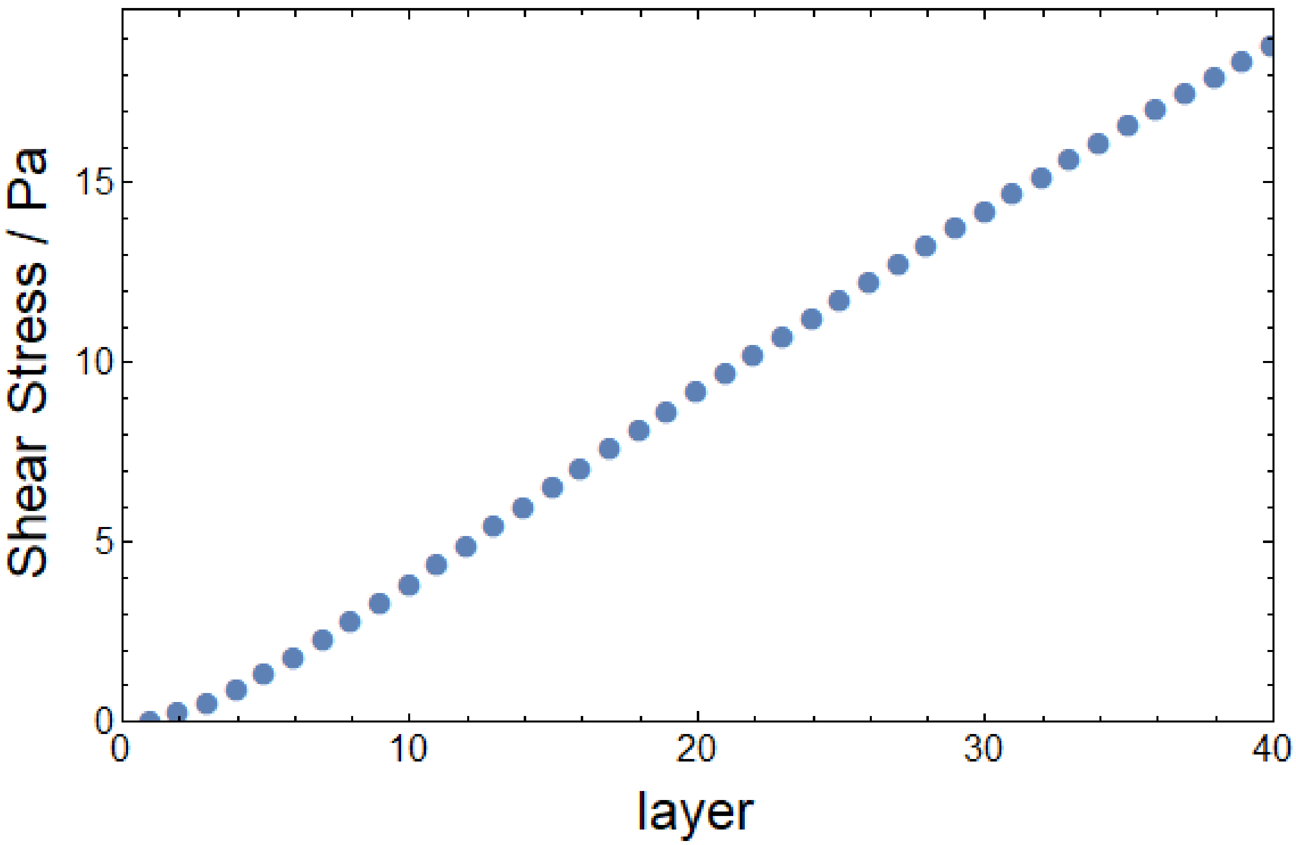

Fig. 4.16: Stress vs time profile of layer 1.

4.4 Sensitivity Analysis of Printing Parameters

To show the effect and significance of each printing parameter, simulations were run using the settings presented in Tables 4.1-3, while varying one printing parameters as shown in Table 4.4. These simulations provide important insight from a manufacturing standpoint as they show how significantly fluctuations or inaccuracies in the printing parameters will affect the part properties. Additionally, these simulations provide initial insight into which parameters significantly affect the part properties and can be used as a starting point for more thorough process optimization. The effect of each parameter on crystallinity in layers 1 and 22, degree of healing at layers 1 and 22, and residual stress at layer 1 are shown in the following sections.

Table 4.4: Variables and levels used to analyze sensitivity of model results.

Variable	Min	Max	Step
t_{layer} (s)	1	10	1
T_{air} (K)	293	423	10
T_{bed} (K)	293	423	10
T_{dep} (K)	653	693	10
h (W/m^2K)	10	100	10

4.4.1 Effect of Printing Parameters on Crystallinity

Figs. 4.17-21 show the effect of each printing parameter on the crystallinity in layer 1. Only bed temperature was found to affect the crystallinity to any significant degree. This shows the expected predominance of the bed on the cooling behavior of the first layer. Crystallization occurred primarily through mechanism 1 and reached the maximum degree of crystallinity possible through that mechanism. This is due to mechanism 2 occurring too slowly to be significant. It is highly likely that if further crystallization could occur, or the bed temperature was lower, the other printing parameters would have had a larger impact on the final crystallinity. Nevertheless, it is apparent that these effects are much weaker than the effect of the bed temperature.

Crystallinity at all locations was the same at bed temperatures 130 °C and higher. This demonstrates that bed temperatures below the Tg can be sufficient for high degree of crystallinity. Below 130 °C, the crystallinity dropped of drastically; showing no crystallization at the bottom of the part at bed temperatures of 110 °C and lower. Crystallinity at the top of the layer decreased much slower, as it was farther from the bed and heated by the adjacent layer, but still decreased significantly as the bed temperature was lowered.

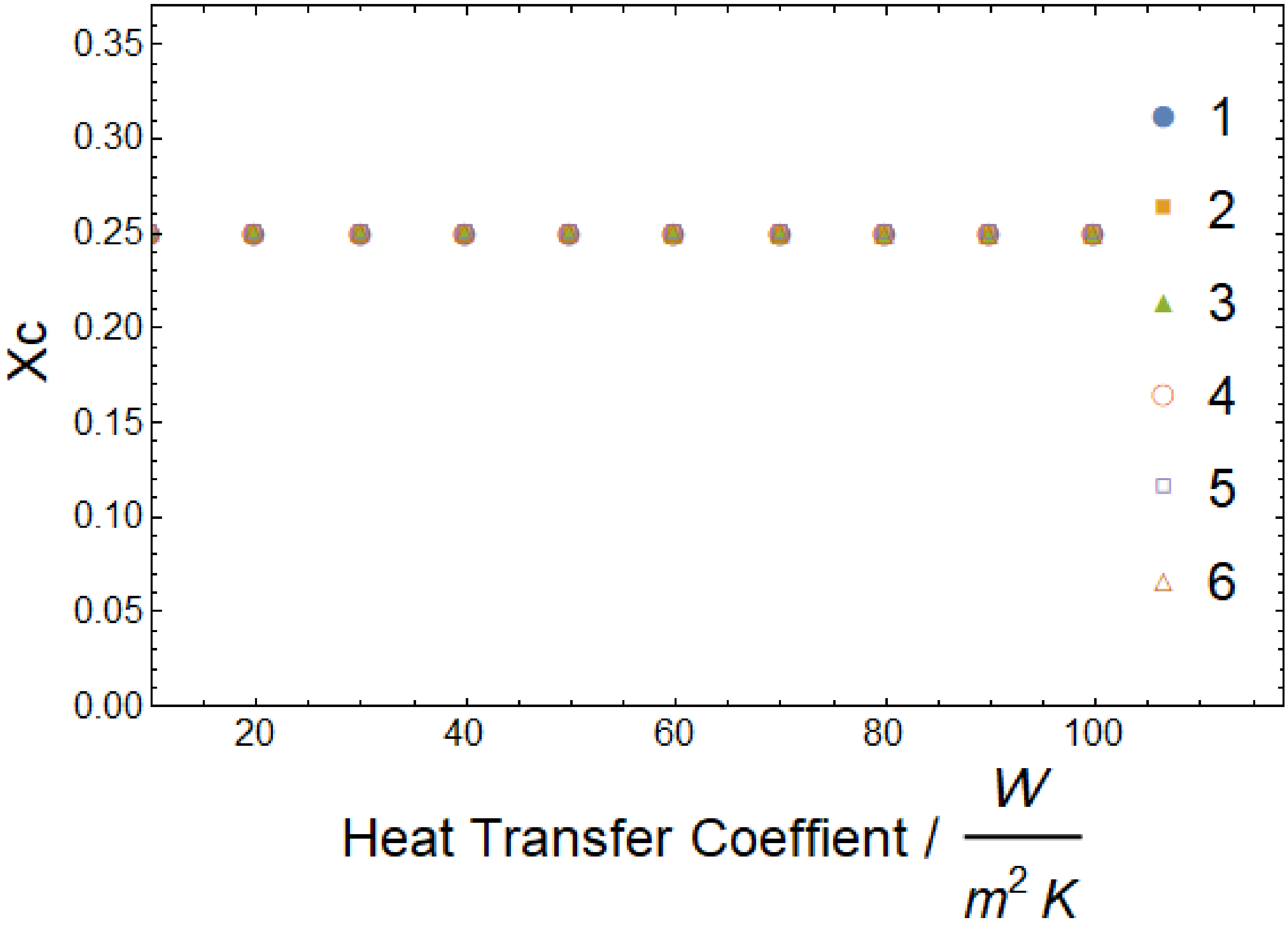

Fig. 4.17: Crystallinity throughout layer 1 as a function of heat transfer coefficient at various locations within a road as described by Fig. 4.4.

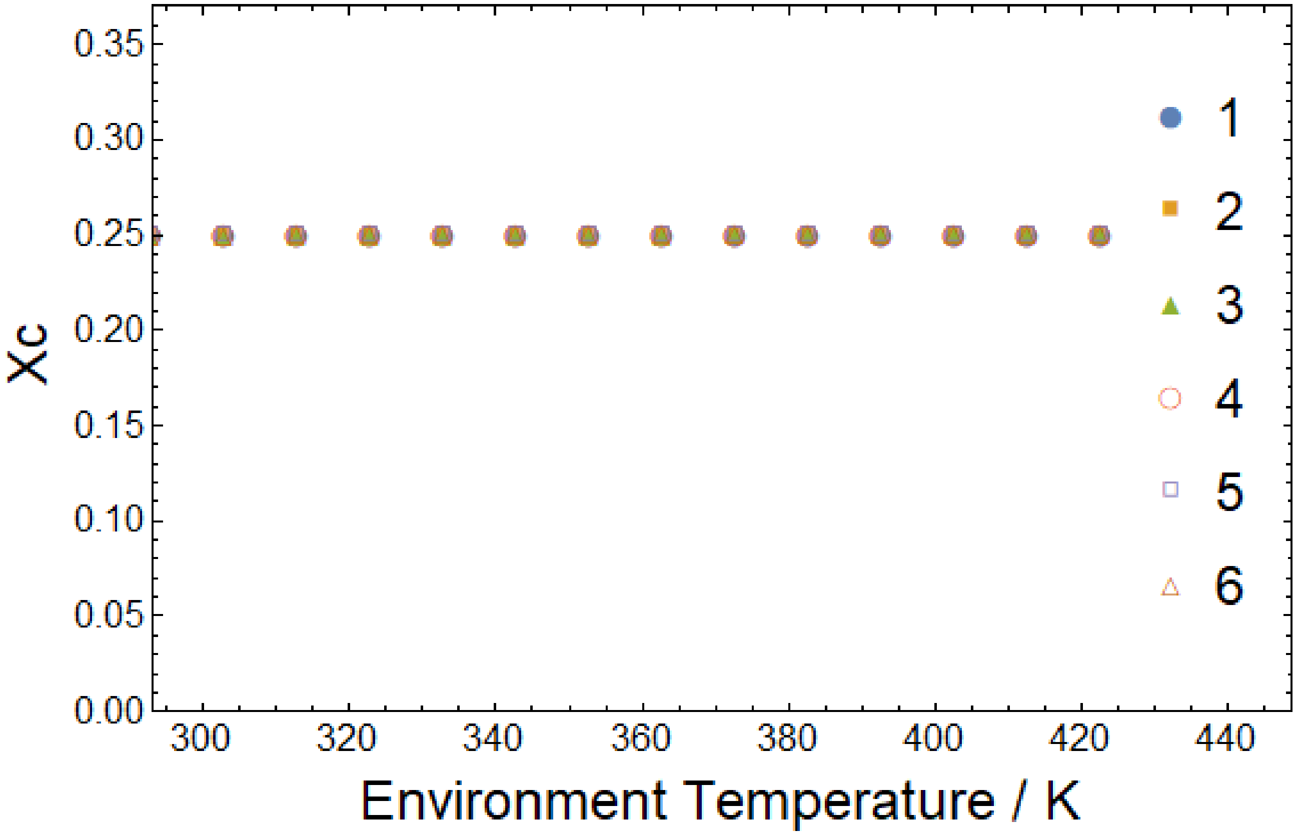

Fig. 4.18: Crystallinity throughout layer 1 as a function of environment temperature at various locations within a road as described by Fig. 4.4.

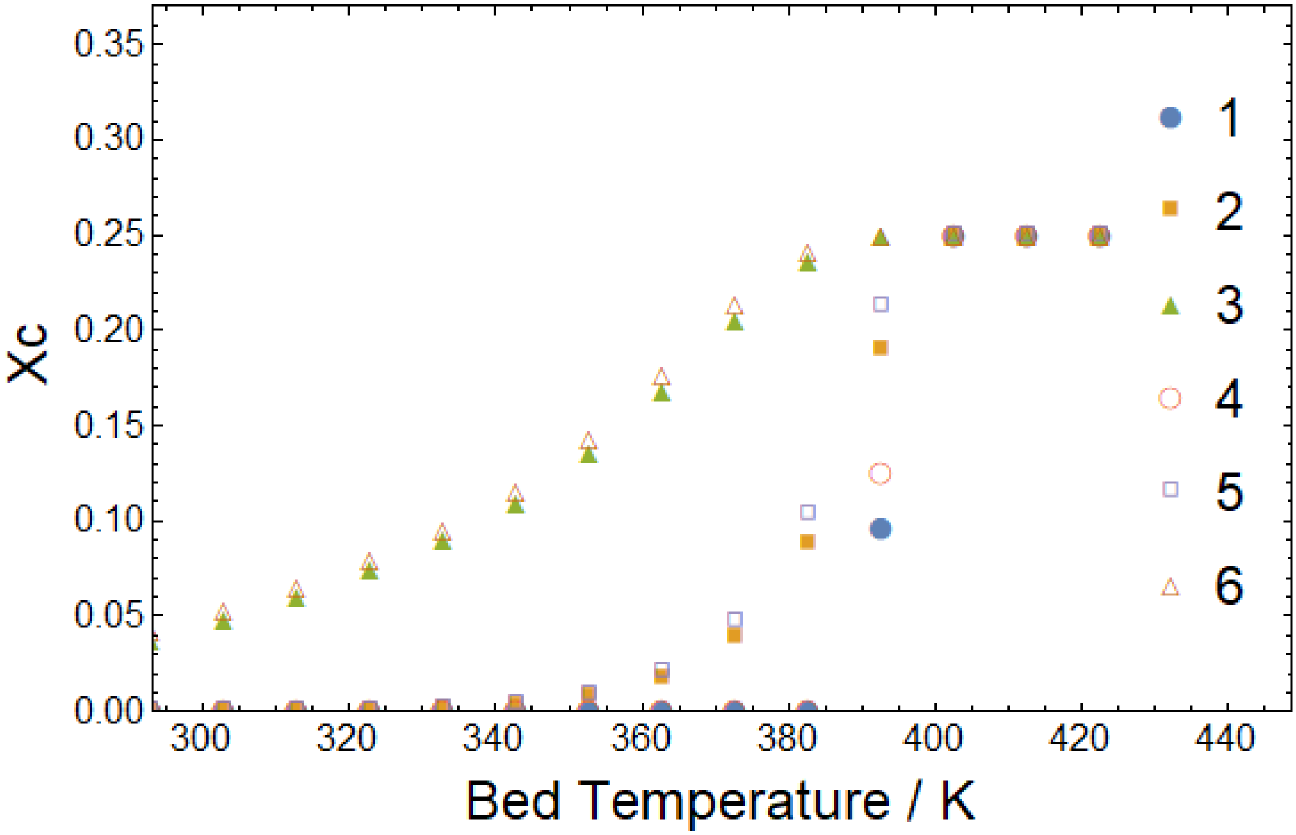

Fig. 4.19: Crystallinity throughout layer 1 as a function of bed temperature at various locations within a road as described by Fig. 4.4.

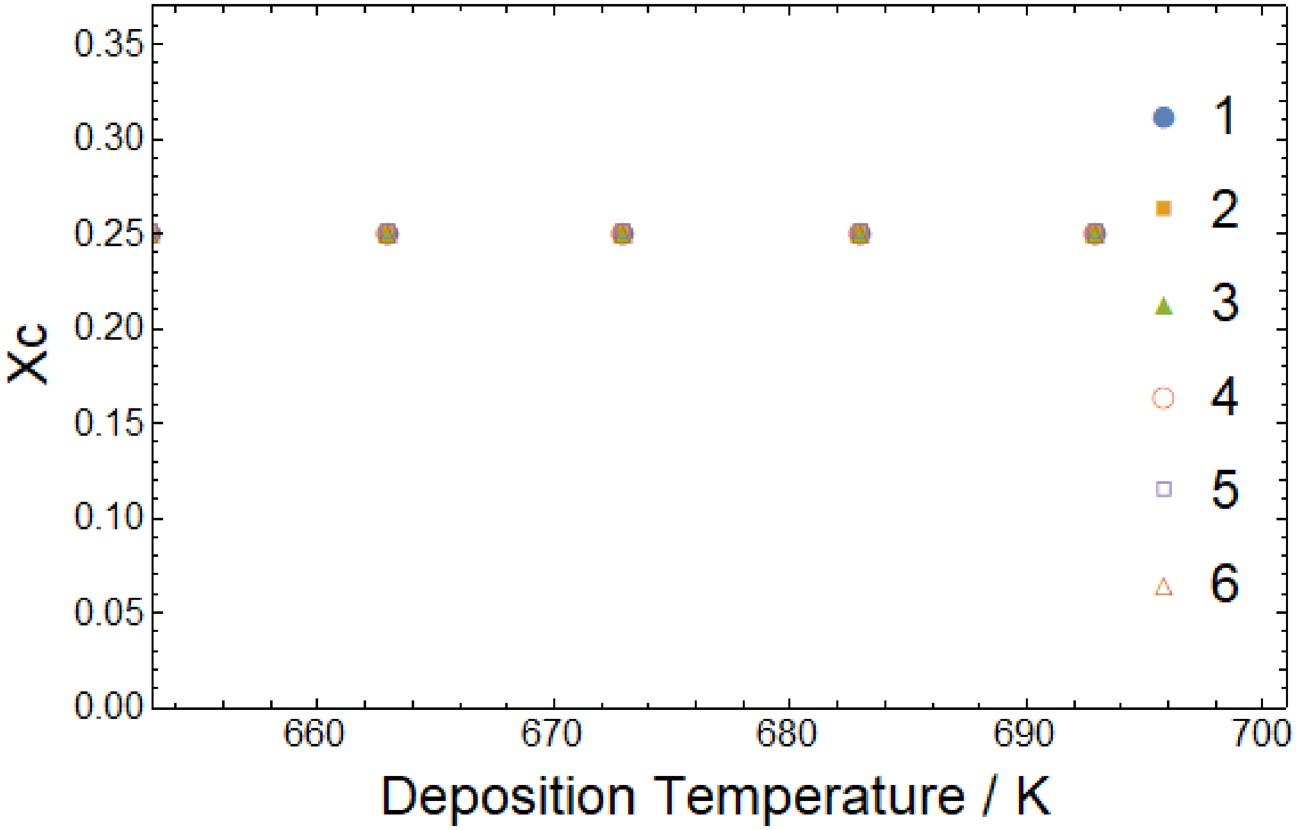

Fig. 4.20: Crystallinity throughout layer 1 as a function of deposition temperature at various locations within a road as described by Fig. 4.4.

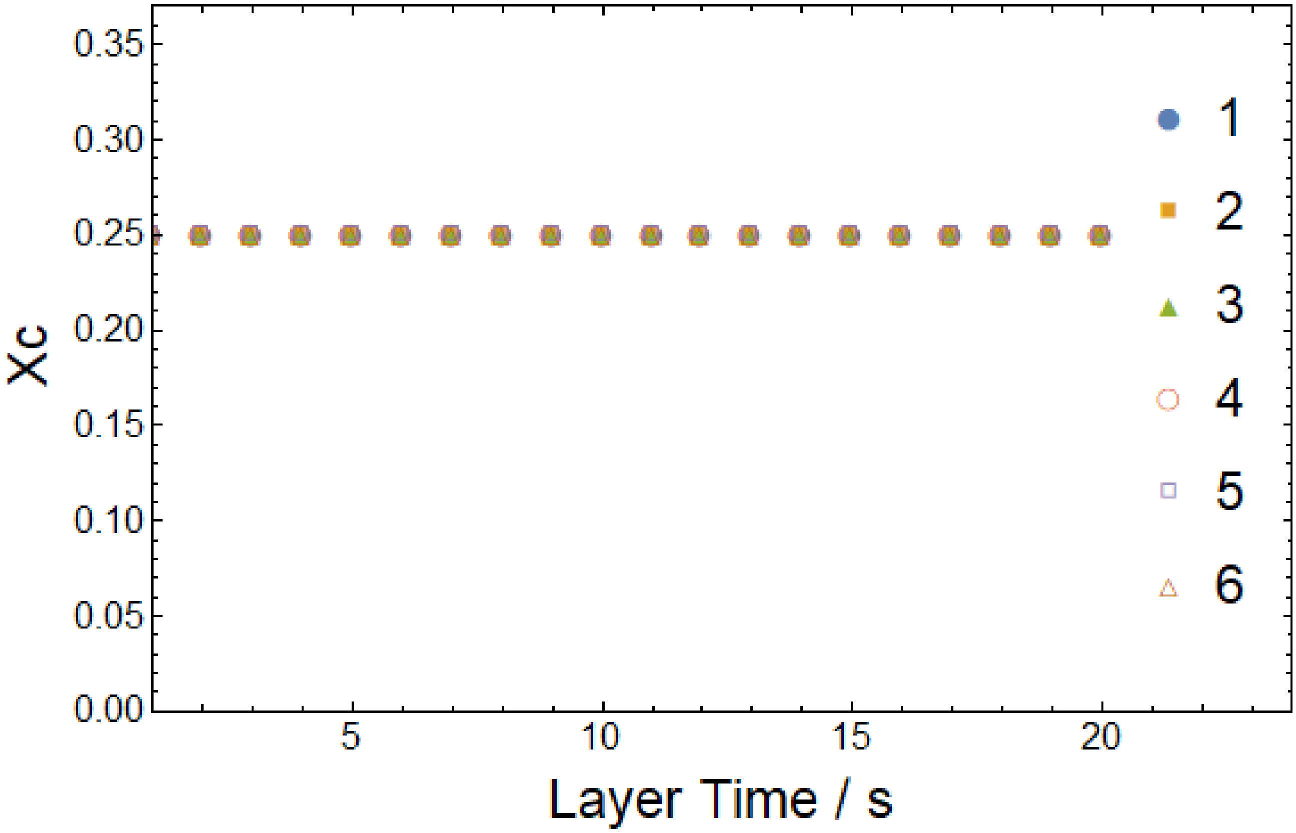

Fig. 4.21: Crystallinity throughout layer 1 as a function of layer time at various locations within a road as described by Fig. 4.4.

Figs. 4.22-26 illustrate the effect of each printing parameter on the crystallinity of layer 22. Layer 22 was much more dependent on every printing parameter other than the bed temperature. This was expected as layer 22 was selected to be far enough from the bed that conduction to and from the bed was negligible. The deposition temperature had little impact on the crystallinity, increasing the degree of crystallinity at the bottom of the part (locations 1 and 4) by 5% but the other locations by much less. This is likely because increasing the deposition temperature does not affect the cooling rate significantly. The more significant effect on crystallinity seen at the lower layers is likely due to the upper layers being sufficiently crystallized such that small changes in the cooling behavior did not affect the final crystallinity.

A low heat transfer coefficient, high environment temperature, and short layer times all lead to high degrees of crystallinity, with values below 60 W/m^{2}K, above 80 °C, or less than 8s all leading to maximum crystallization. This makes sense as each of these reduce the amount of heat dissipated to the environment; confirming that crystallinity depends predominately on convection in the higher layers. On the opposite end, when large amounts of heat were transferred to the environment, the parts cooled too quickly for complete crystallization. The exception to this is the upper regions of each part which had high degrees of crystallinity at most conditions tested. This was because the heating from the next road was sufficient to produce a high degree of crystallization regardless of the convection behavior. Of the three terms, layer time had the smallest effect; reducing the crystallinity at location 1 to 17.1% while the heat transfer coefficient and environment temperature lowered the crystallinity to 8.3% and 4.0% respectively. Given that the ranges simulated represent the reasonable possible ranges of these parameters, this gives an idea of the relative importance of each parameter on crystallinity.

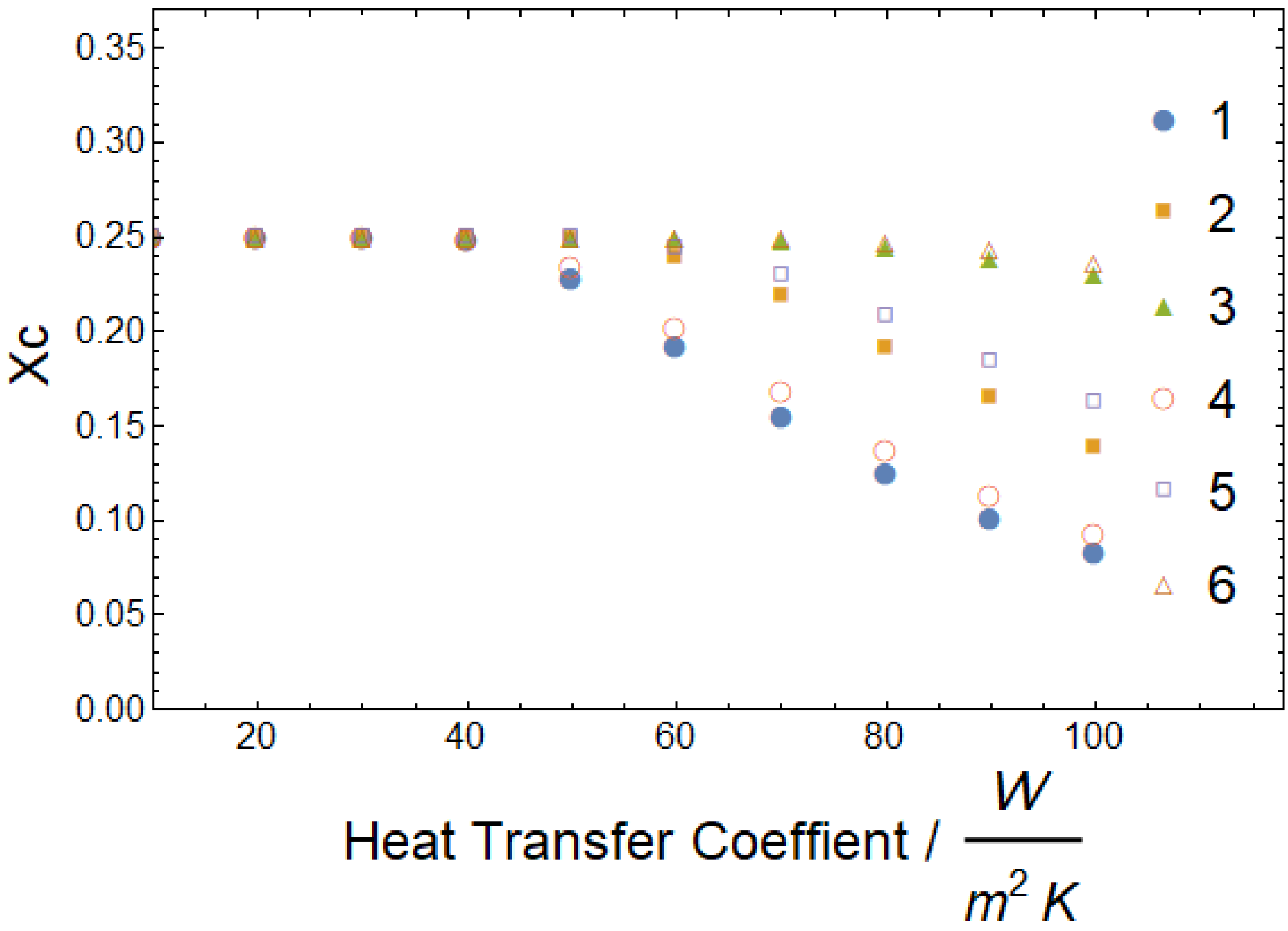

Fig. 4.22: Crystallinity throughout layer 22 as a function of heat transfer coefficient at various locations within a road as described by Fig. 4.4.

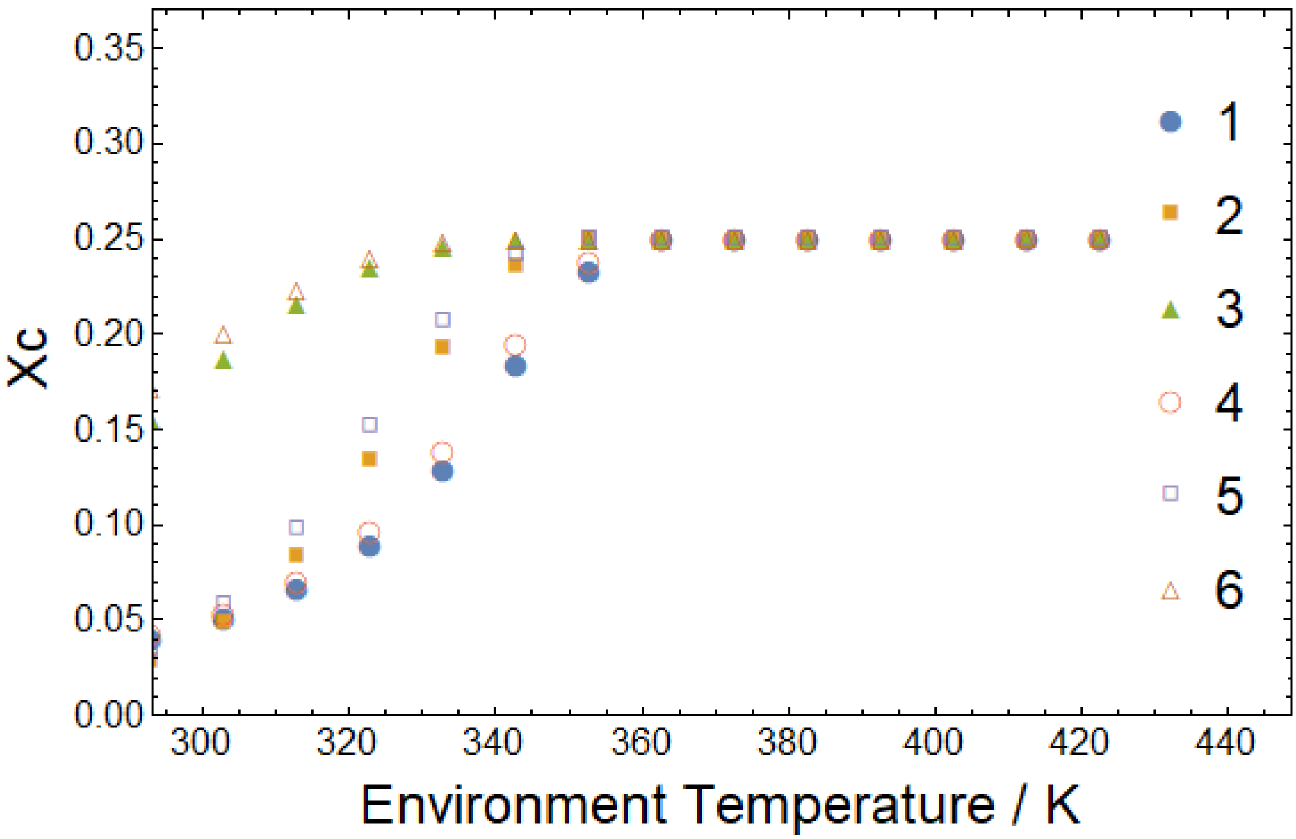

Fig. 4.23: Crystallinity throughout layer 22 as a function of environment temperature at various locations within a road as described by Fig. 4.4.

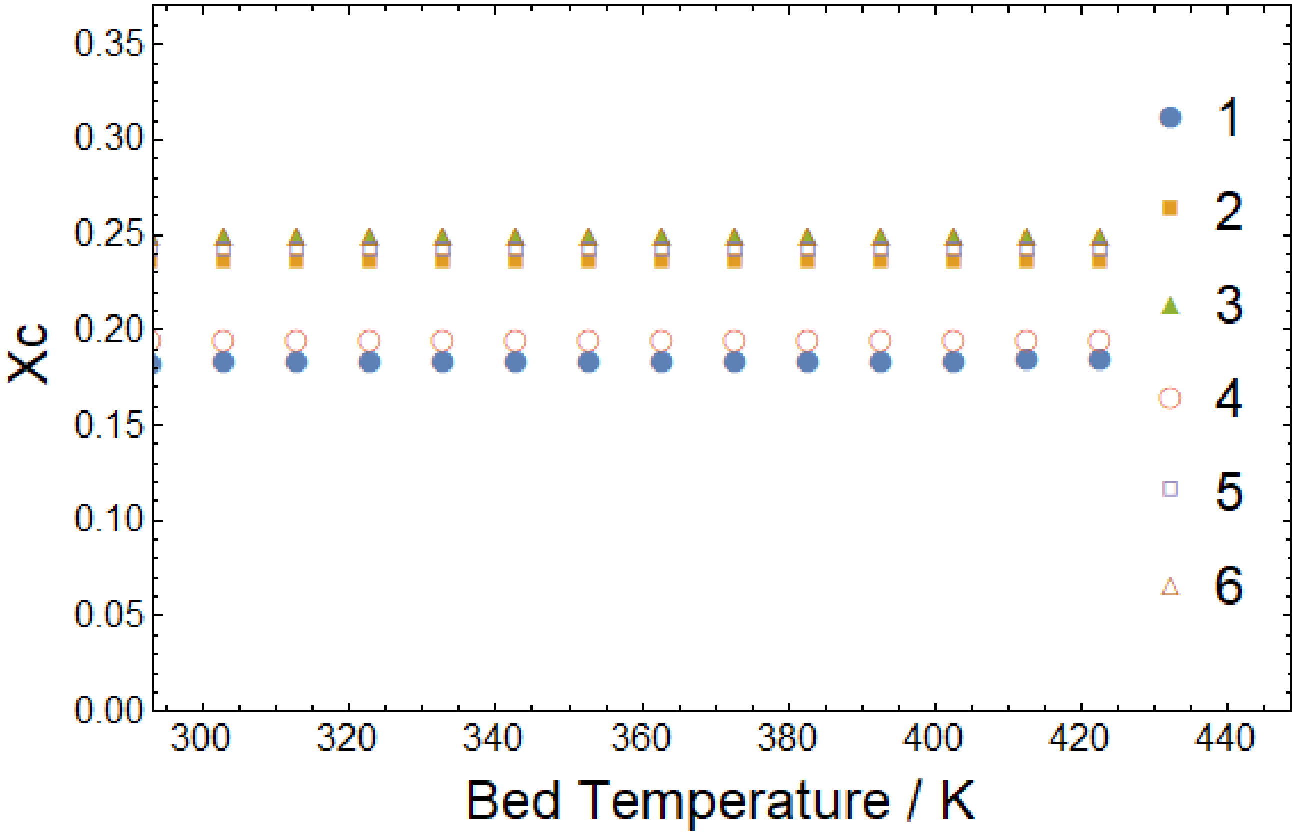

Fig. 4.24: Crystallinity throughout layer 22 as a function of bed temperature at various locations within a road as described by Fig. 4.4.

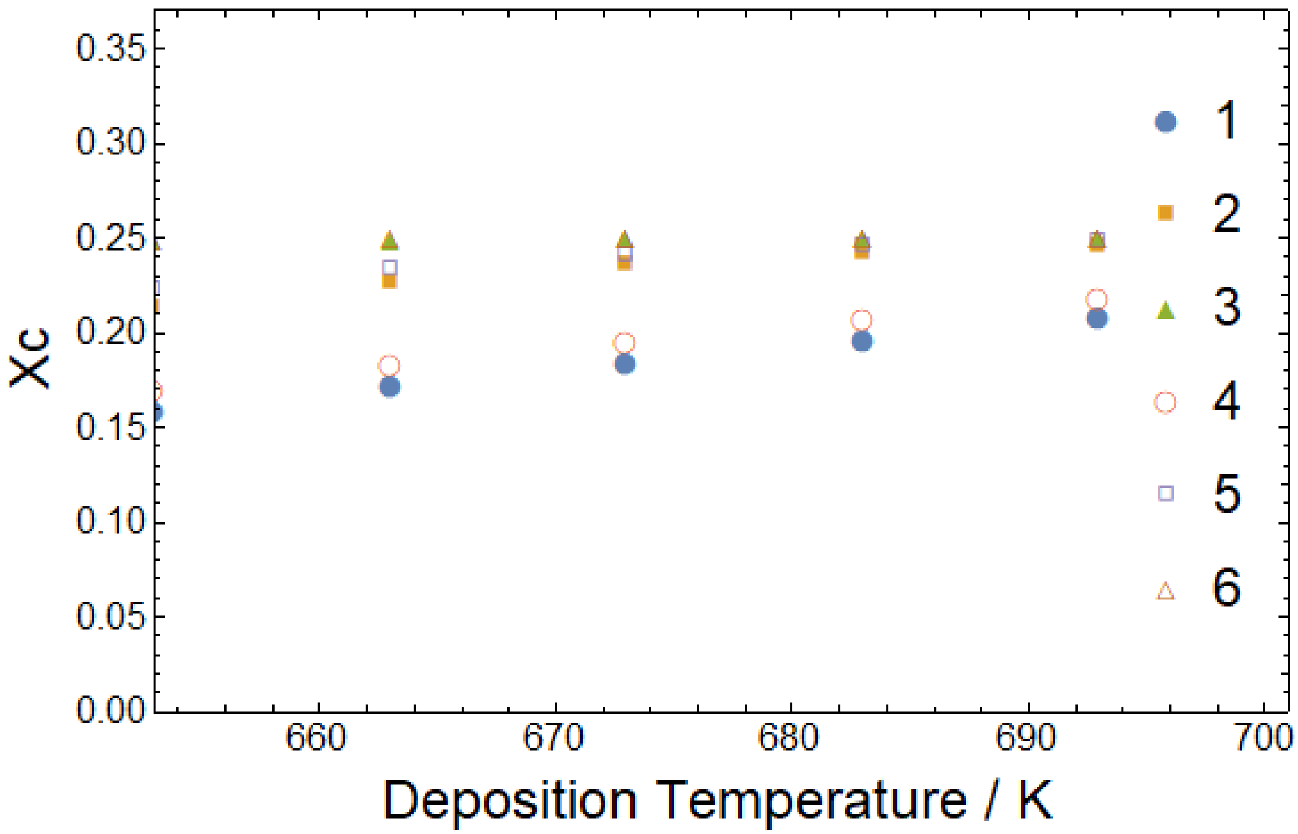

Fig. 4.25: Crystallinity throughout layer 22 as a function of deposition temperature at various locations within a road as described by Fig. 4.4.

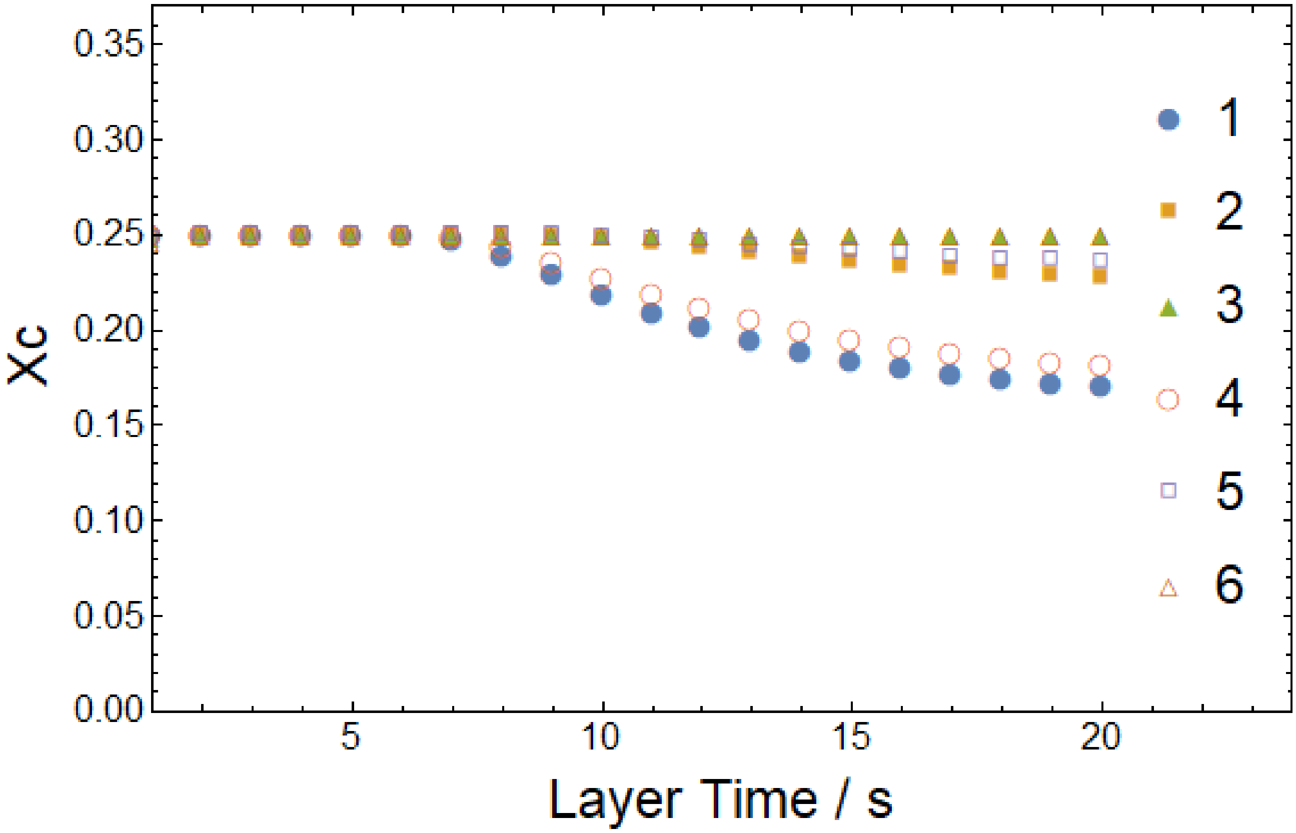

Fig. 4.26: Crystallinity throughout layer 22 as a function of layer time at various locations within a road as described by Fig. 4.4.

4.4.1 Effect of Printing Parameters on Degree of Healing

The degree of healing at layers 1 and 22 as a function of each printing parameter are illustrated in Figs. 4.27-31. Each parameter had a significant effect on the degree of healing, many of which were complicated due to the interactions between crystallization and interlayer healing. Healing in the case of no crystallization was also examined to deconvolute this interaction.

For the amorphous case, higher heat transfer coefficients lead to a significant reduction in the degree of healing due to faster cooling. This is shown in layer 1 which had a decrease in healing from 58.7% to 49.7%. For layer 22, however, the decrease in crystallinity at higher values of h lead to an overall increase in the degree of healing at high heat transfer coefficients. The opposite relationship was seen with environment temperature; where the degree of healing of layer 1 increased from 50.1% to 57.3 while the degree of healing of layer 22 had a minimum at a temperature of 373° C. Given that layer 22 represents the bulk properties, these results show that elevated environment temperatures may have a detrimental effect on the strength of semi-crystalline materials unless it is heated to very high temperatures.

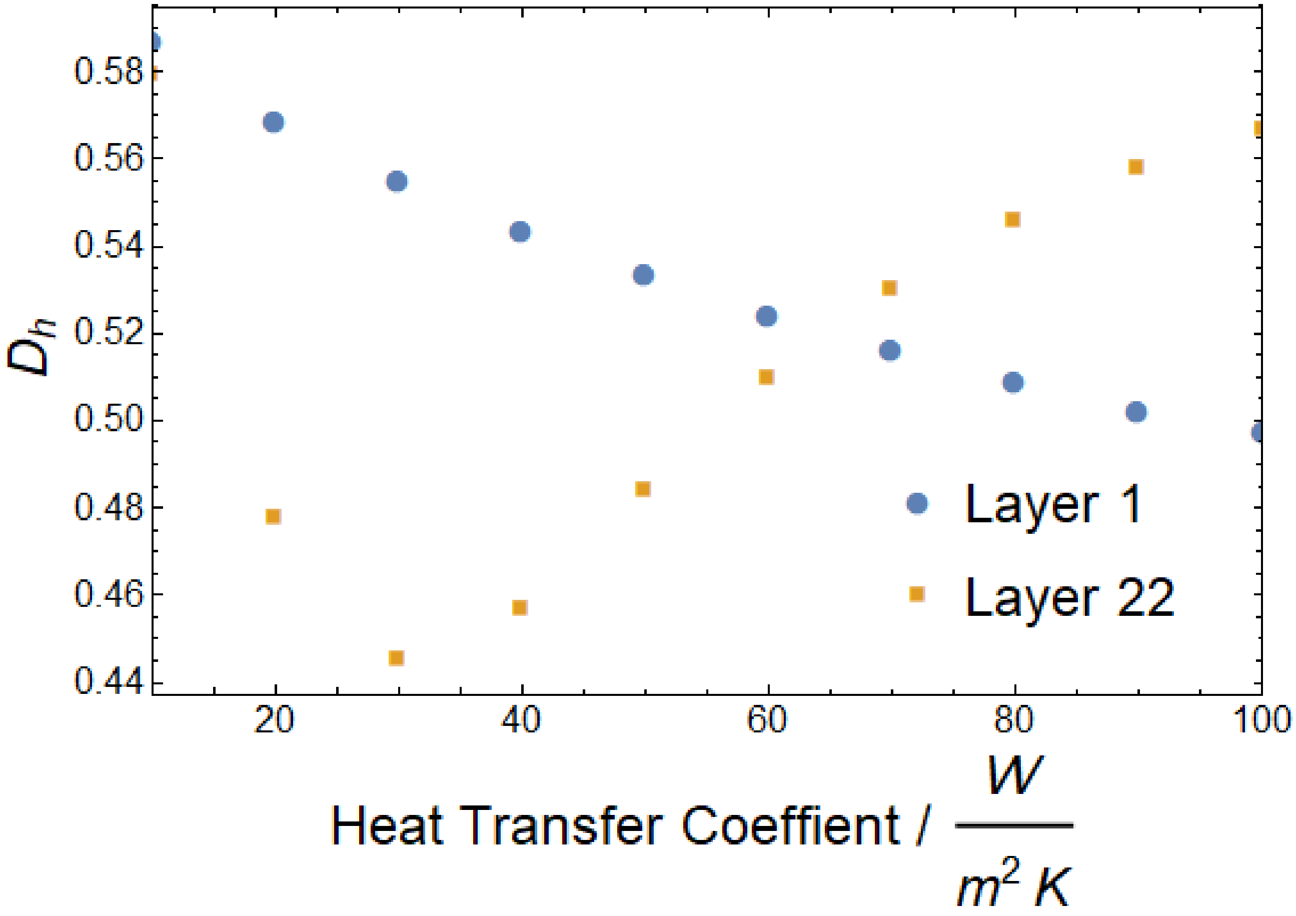

Fig. 4.27: Degree of healing of layers 1 and 22 as a function of heat transfer.

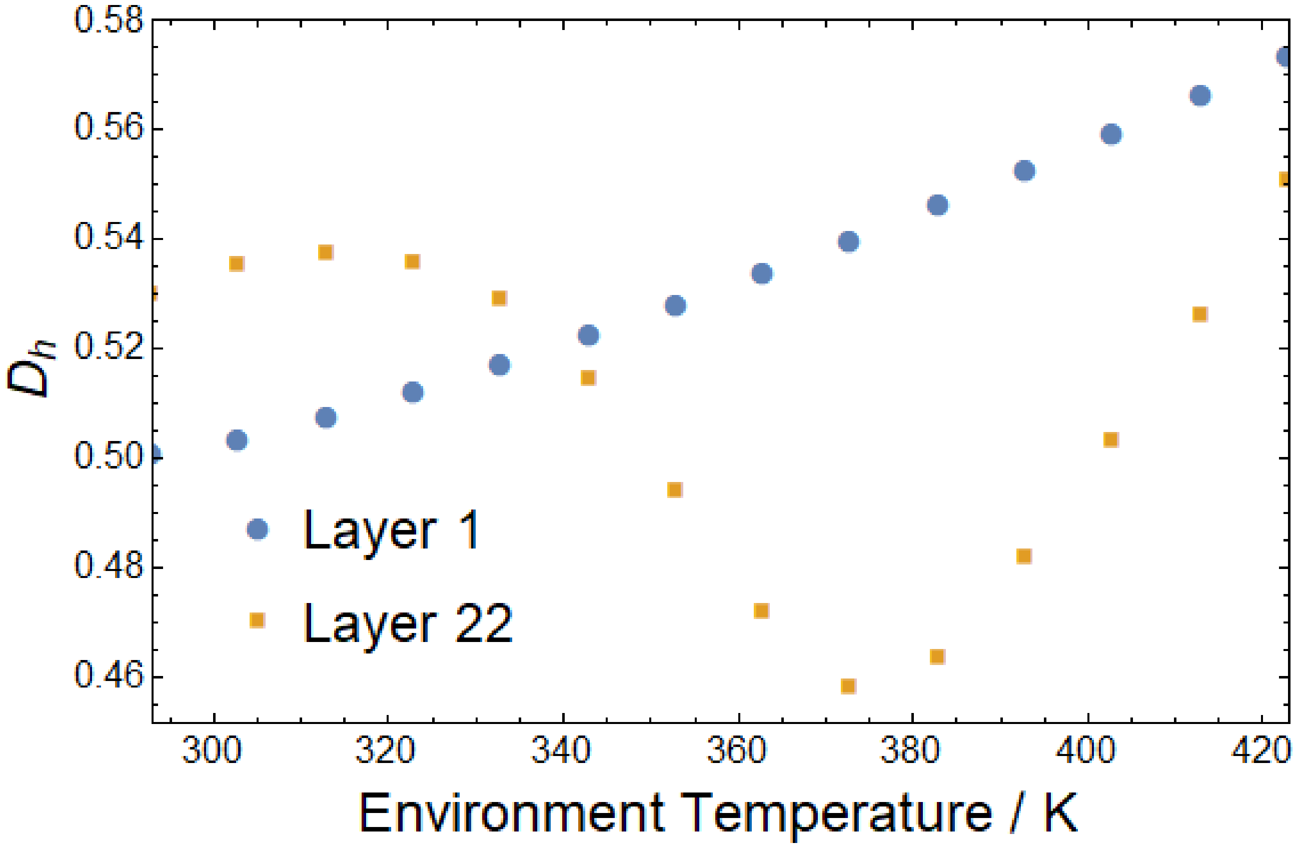

Fig. 4.28: Degree of healing of layers 1 and 22 as a function of environment temperature.

As with crystallinity, bed temperature had no influence on the healing of layer 22. Layer 1, however, had significantly higher healing at elevated bed temperatures until 140 °C where the degree of healing started to weaken again. This is likely due to faster crystallization at these temperatures. It should be noted that all the other tests were run at bed temperatures above this range and therefore had a lower degree of healing than if a lower bed temperature was used. It is also important to note that very high bed temperatures are needed to reduce warpage so finding ways to slow crystallization may be necessary to achieve high degrees of healing.

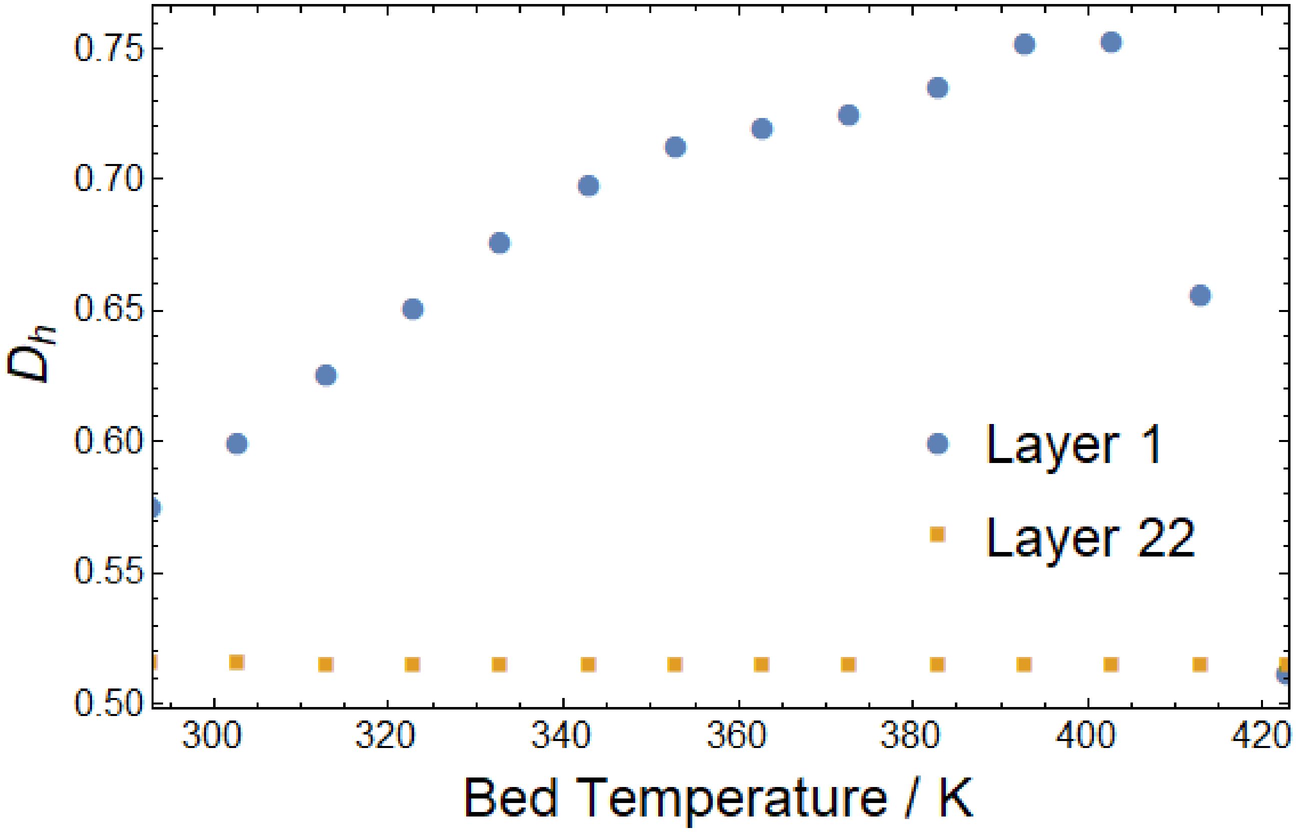

Fig. 4.29: Degree of healing of layers 1 and 22 as a function of bed temperature.

Higher deposition temperatures lead to increased healing at both layers. Layer 1 increased from 50.2 to 54.4% and layer 22 increased from 49.4 to 53.6%. This is expected as healing takes place significantly faster at higher temperatures.

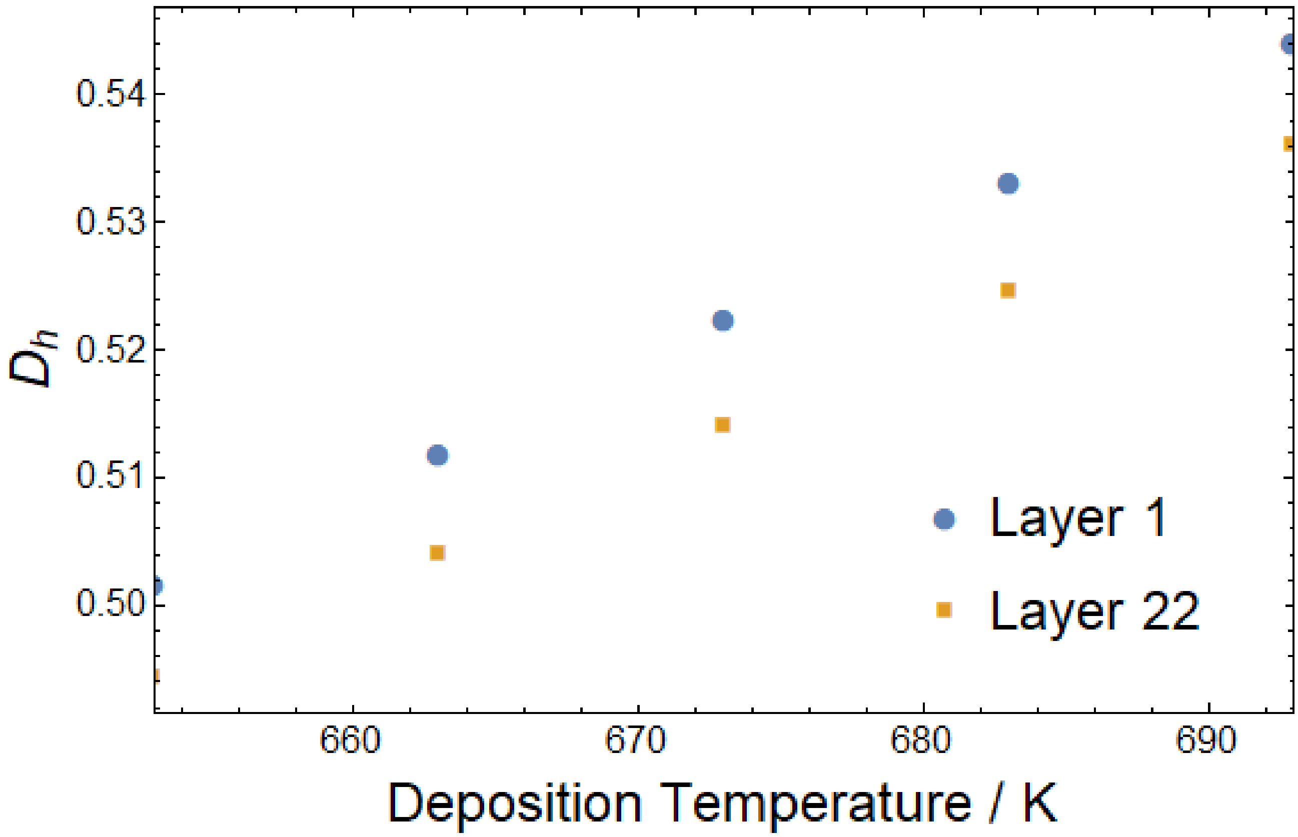

Fig. 4.30: Degree of healing of layers 1 and 22 as a function of deposition temperature.

At very short layer times (high print speeds), the degree of healing was significantly higher because it did not have as much time to cool before the addition of the next layer. These layer times would be very small for a real part, however, making it difficult to increase healing this way. Alternatively, the degree of healing was somewhat greater at long layer times as the maximum amount of healing could take place before the interface was heated again. For layer 1, healing increased from 51.7% at a layer time of 10 s to 53.5% at a layer time of 20 s. Layer 22 showed a much smaller effect with only a 0.5% increase.

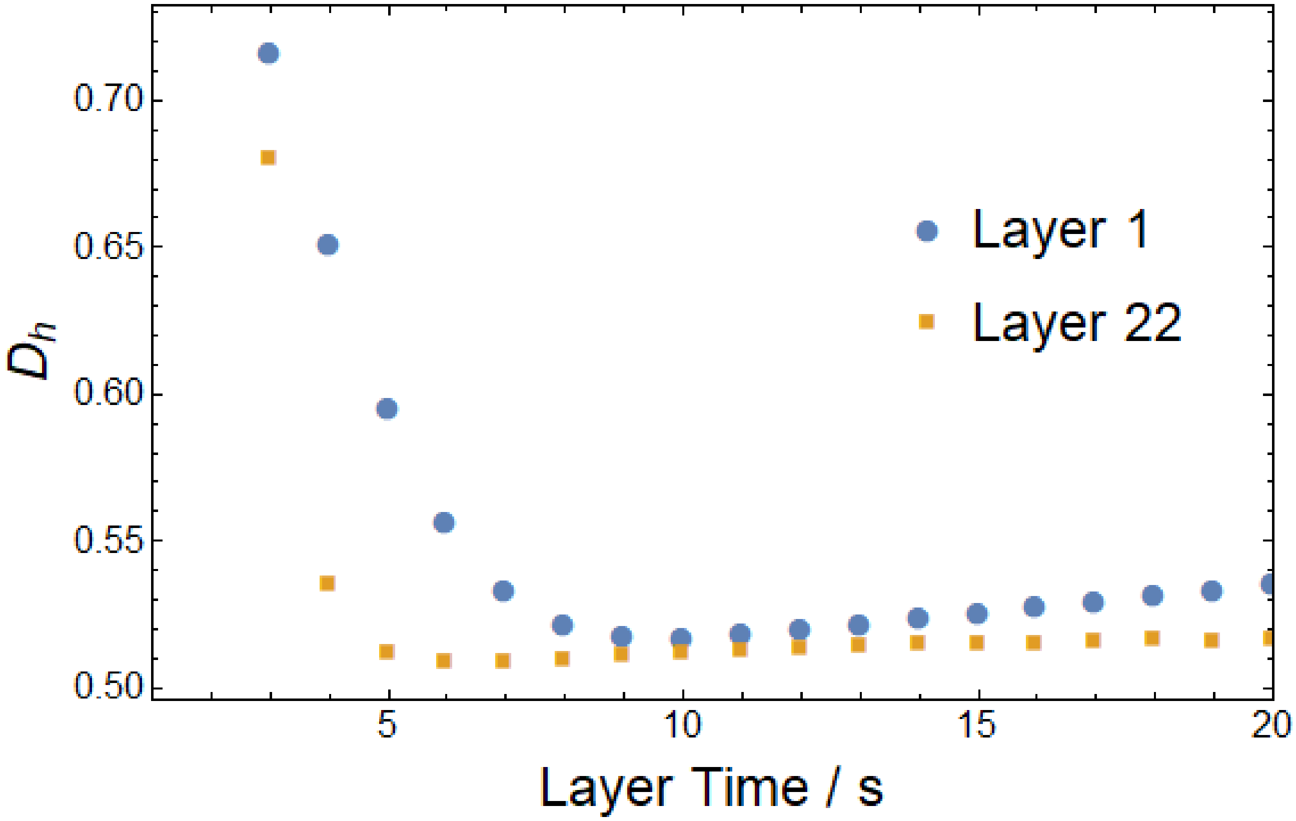

Fig. 4.31: Degree of healing of layers 1 and 22 as a function of layer time.

4.4.1 Effect of Printing Parameters on Residual Stress

Figs. 4.32-36 show the effect of each printing parameter on the shear stress at the bottom of layer 1. The interaction between shear stress and the heat transfer showed a maximum at around 50 W/m^{2}K. The decrease at small values of h was due to slower cooling while the decrease at high values of h was due to less crystallization. Overall, the reduction in stress due to slower cooling at low heat transfer coefficients was greater than the reduction in stress due to reduced crystallinity.

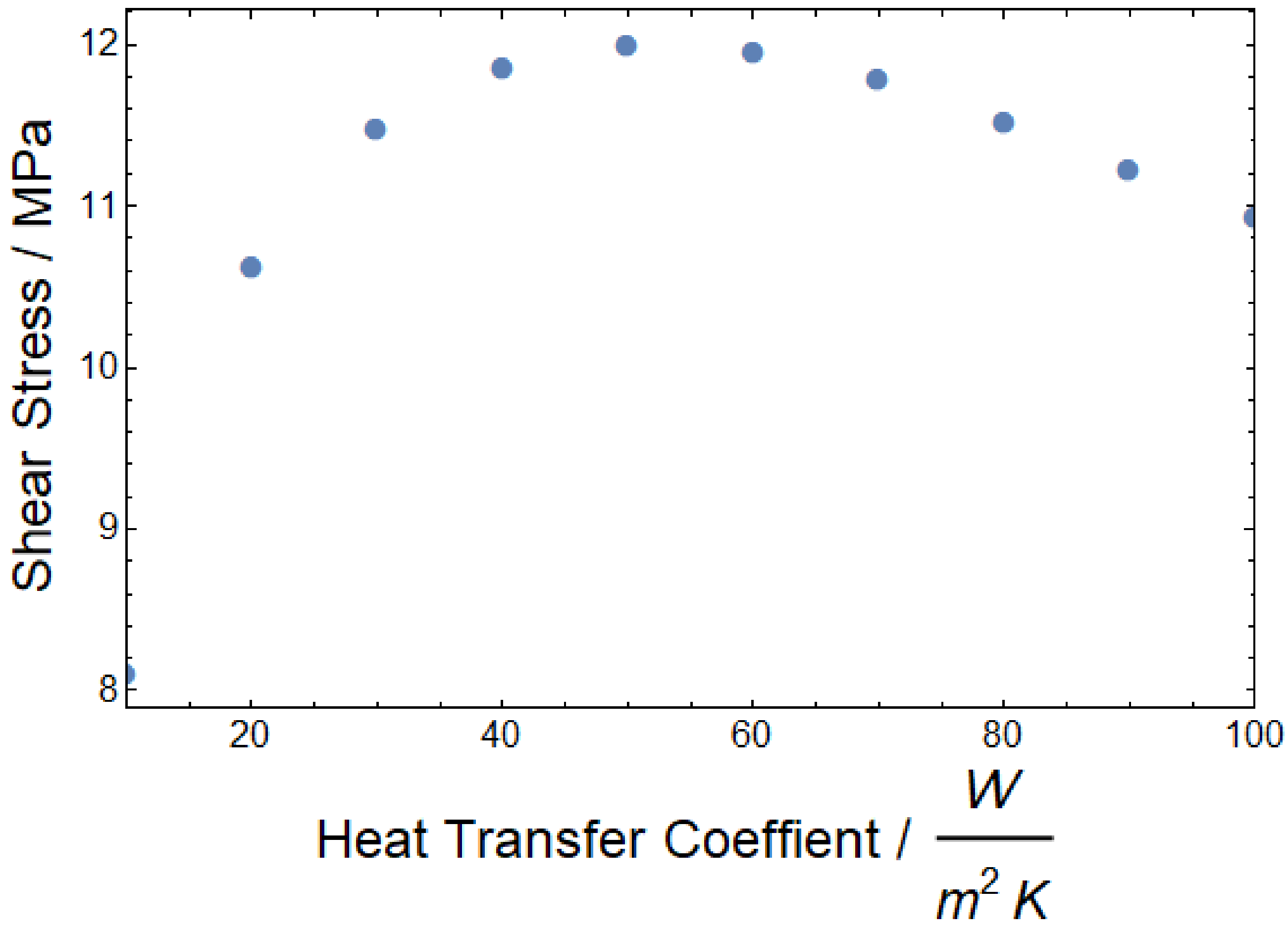

Fig. 4.32: Shear stress at the bottom of layer 1 as a function of heat transfer coefficient.

Fig. 4.33 shows the interaction between the environment temperature and the shear stress. The shear stress was lowest at higher environment temperatures as minimum temperature of the parts was higher. This effect was not as pronounced at low temperatures as the reduction in thermal contraction was counteracted by an increase in crystallinity. A similar trend can be seen in Fig. 4.34 between the shear stress and the bed temperature; though the effect was much weaker as the bed temperature only affected the bottom layers.

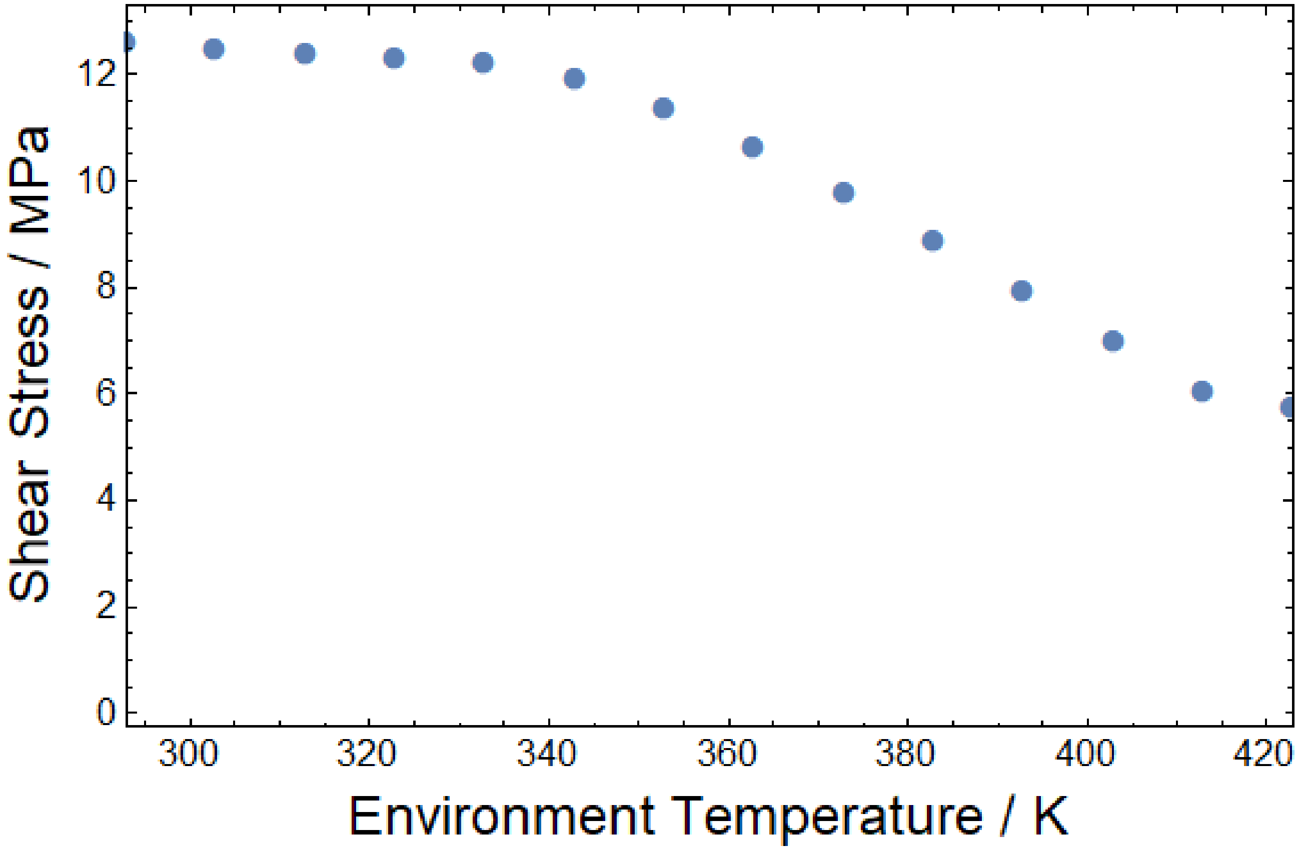

Fig. 4.33: Shear stress at the bottom of layer 1 as a function of environment temperature.

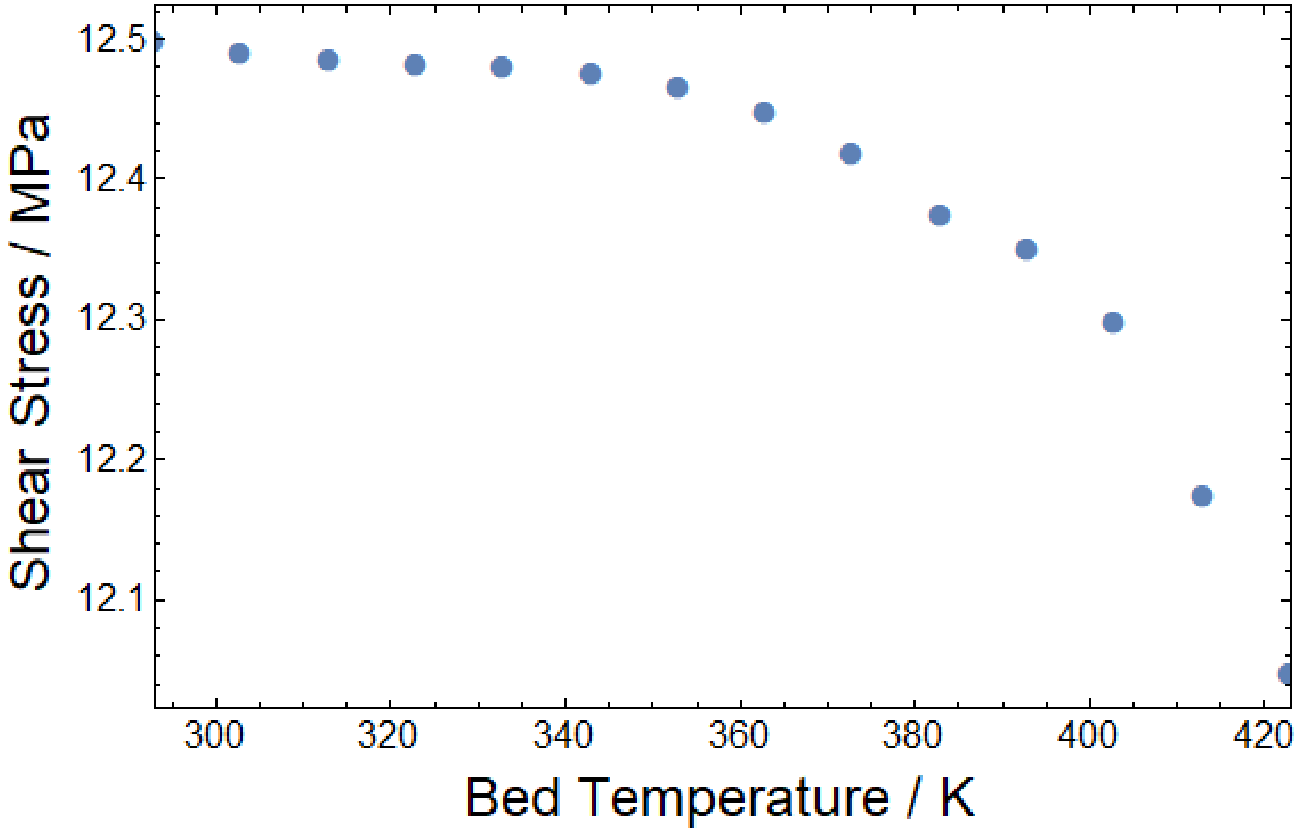

Fig. 4.34: Shear stress at the bottom of layer 1 as a function of bed temperature.

Fig. 4.35 displays the relationship between the deposition temperature and shear stress. The shear stress increased with deposition temperature, but only by 1 MPa or approximately 9% of the total stress. This increase is due to an increase in crystallinity.

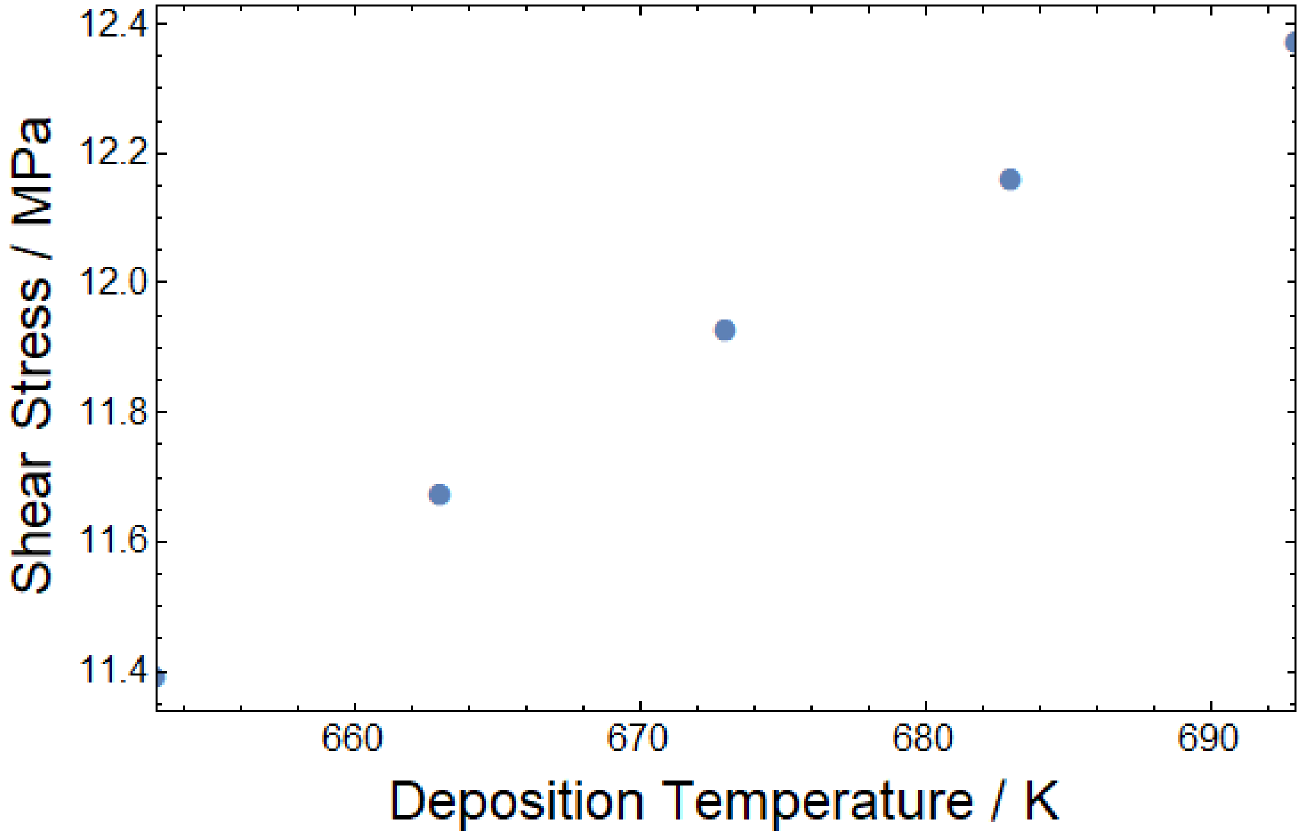

Fig. 4.35: Shear stress at the bottom of layer 1 as a function of deposition temperature.

Fig. 4.36 illustrates the relationship between the layer time and shear stress. A maximum was seen at around 7 s. At short layer times, each layer had less time to cool before another layer was printed which lowered the stress built up between layers. At longer layer times, there was a reduction in stress due to reduced crystallization. The reduction in stress at short layer times was much more significant, though achieving cooling times that low is difficult. Overall, the heat transfer coefficient and environment temperatures had the largest effect on the shear strain as they affect cooling of every layer for the entirety of the printing process.

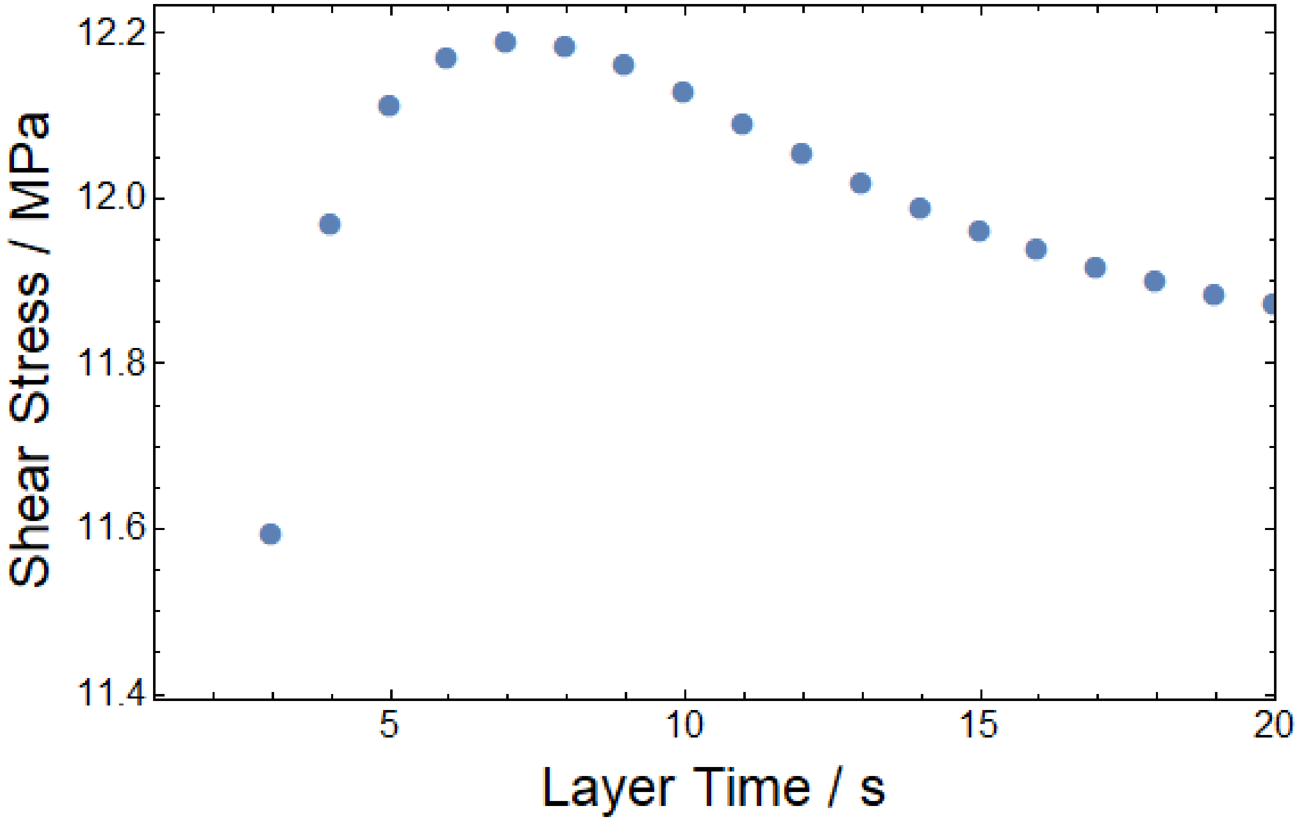

Fig. 4.36: Shear stress at the bottom of layer 1 as a function of layer time.

4.5 Sensitivity Analysis of Material Properties

In addition to the printing parameters, the effects of various material properties were studied to determine the significance of each. Simulations were run using the default values in Tables 4.1-3 and varying a single material property as shown in Table 4.5. To ensure that the temperature dependency of these factors was still accounted for, the property functions were multiplied by a factor ranging from 0.5x-2x. The effect of each property on crystallinity in layers 1 and 22, degree of healing at layers 1 and 22, and residual stress at layer 1 are shown in Figs. 4.37-45.

Table 4.5: Variables and levels used to analyze sensitivity of model results.

Variable	Min	Max	Step
c_p (J/K)	0.5x	2x	0.1x

k (W/mK)	0.5x	2x	0.1x
G/E	0.33	0.5	0.01

Figs. 4.37-40 display the effect of changes in the thermal conductivity and the specific heat on the crystallinity of layers 1 and 22. As with previous variables, neither property had a significant impact on the crystallinity of layer 1. The crystallinity of layer 22 diminished as the thermal conductivity was increased, with a maximum decrease in crystallinity of 9.2% at location 1. When the specific heat was increased by a factor of 1.3x or more the crystallinity at all locations was 25%. Below this value, they diminished significantly due to faster cooling rates. The minimum crystallinity was 3.1% at position 1.

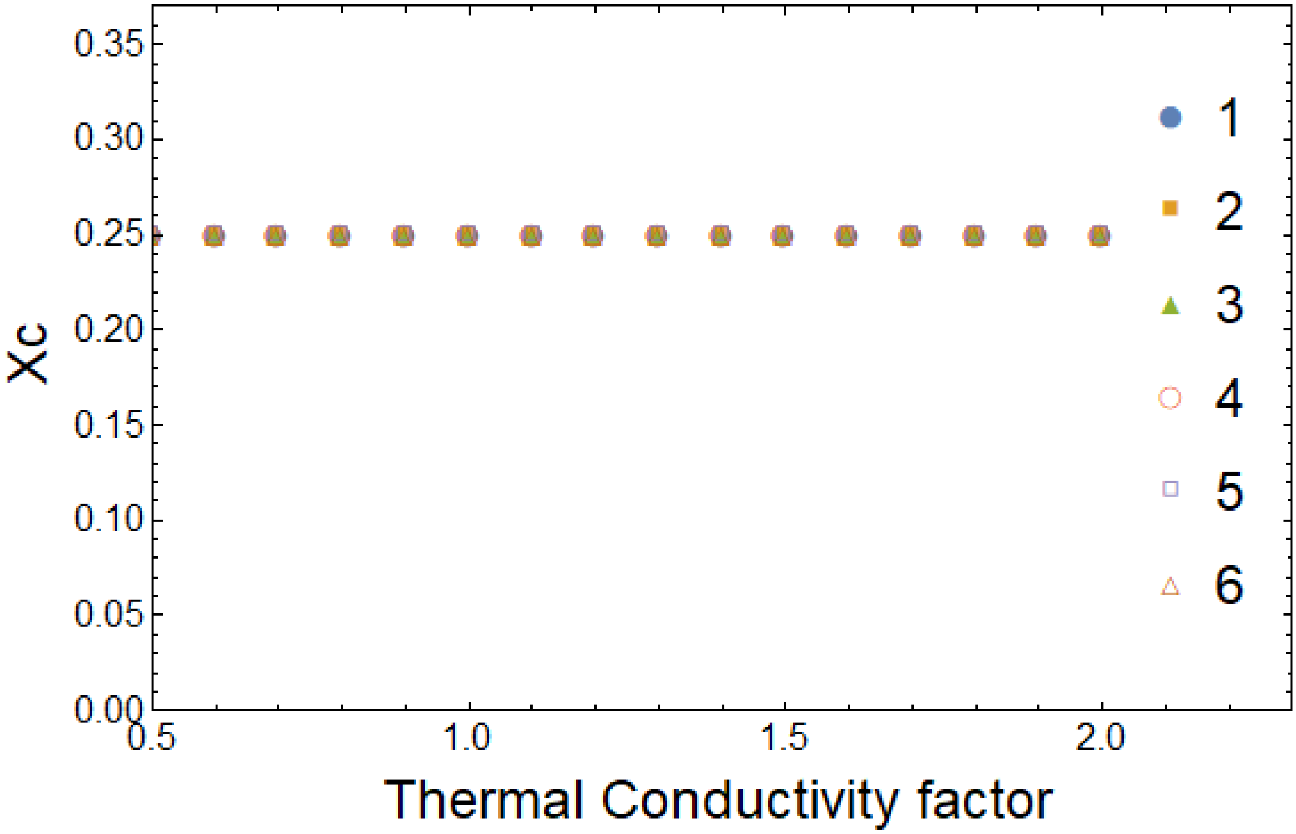

Fig. 4.37: Crystallinity throughout layer 1 as a function of thermal conductivity at various locations within a road as described by Fig. 4.4.

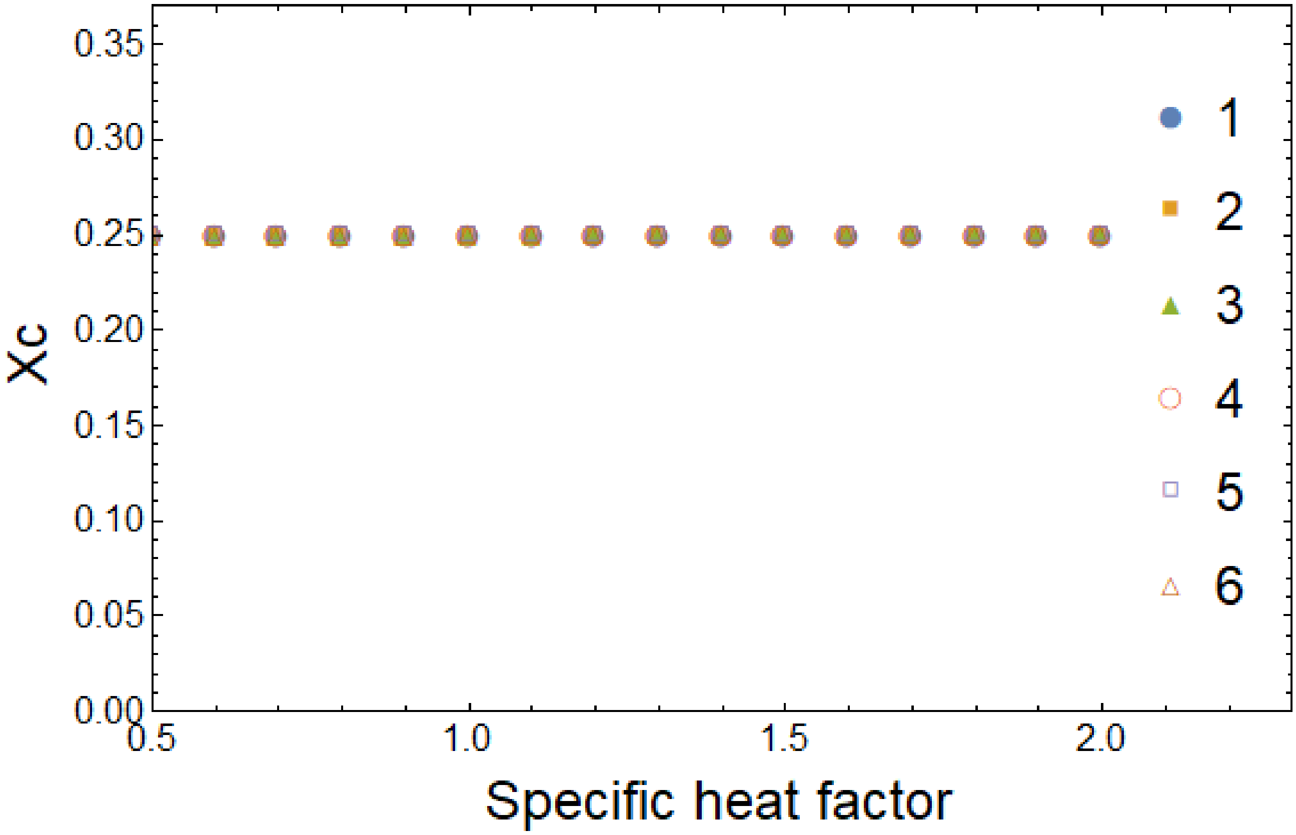

Fig. 4.38: Crystallinity throughout layer 1 as a function of specific heat at various locations within a road as described by Fig. 4.4.

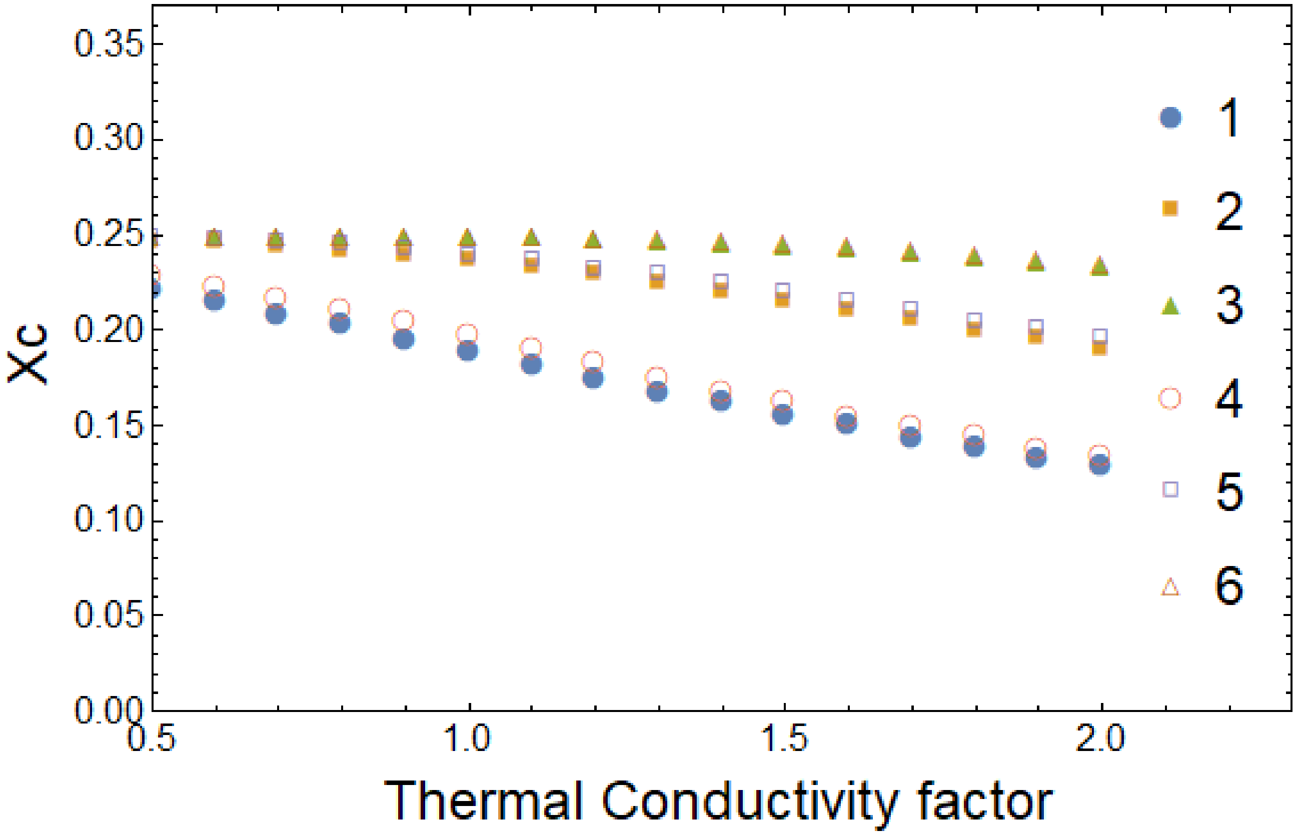

Fig. 4.39: Crystallinity throughout layer 22 as a function of thermal conductivity at various locations within a road as described by Fig. 4.4.

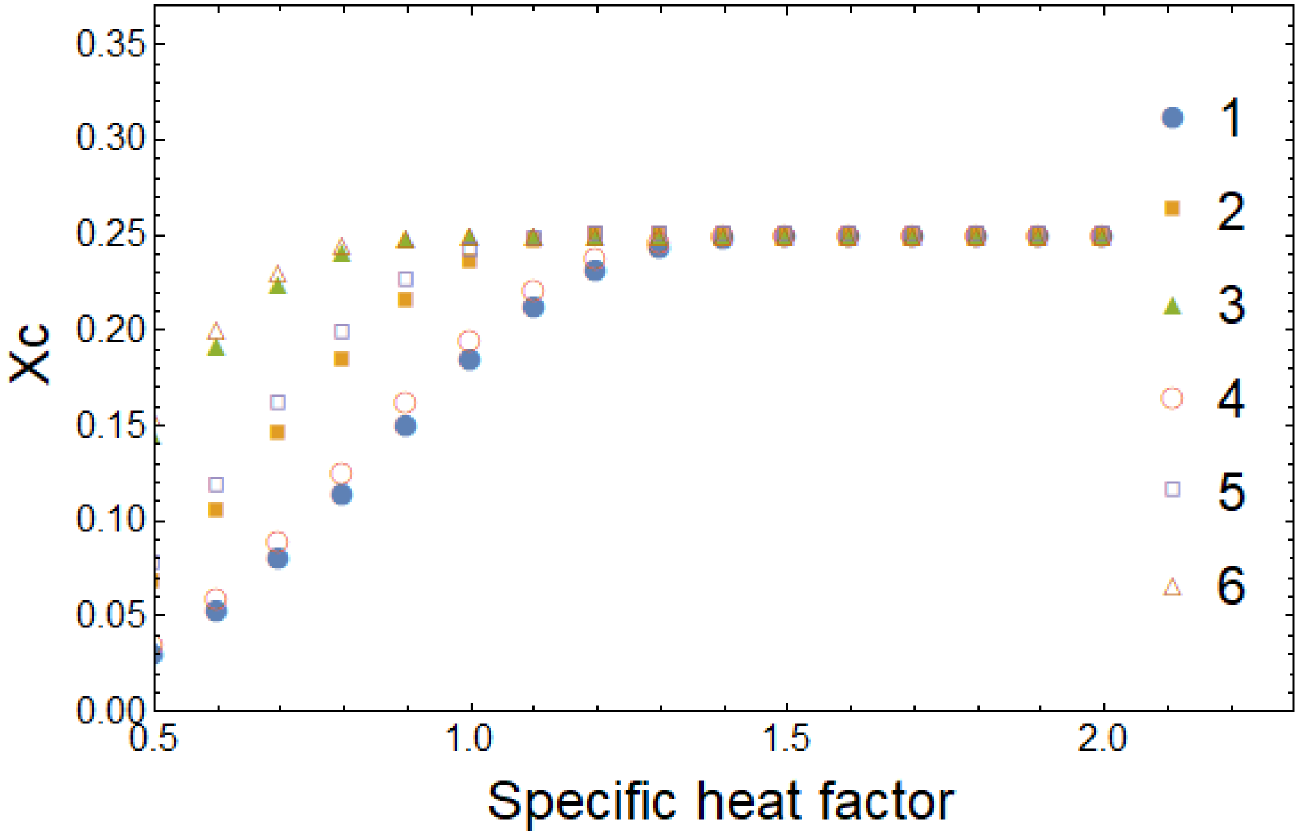

Fig. 4.40: Crystallinity throughout layer 22 as a function of specific heat at various locations within a road as described by Fig. 4.4.

The interaction between thermal conductivity and specific heat with the degree of healing are illustrated in Fig. 4.41-42. For layer 1, healing decreased by 0.05 as the thermal conductivity was increased. This was entirely due to faster crystallization as healing of layer 1 increased with thermal conductivity in the amorphous case. The opposite was seen in layer 22 which increased by 0.06 as the thermal conductivity was increased. This was also due to less crystallization as high thermal conductivity increased the cooling rate which would lower the degree of healing if nor for the reduction in crystallinity associated with it. As for the effect of the specific heat, healing in layer 1 increased by 0.12 while healing in layer 22 decreased by 0.13 initially, then increased by 0.03 at high specific heats. The initial decrease at layer 22 was due to the increase in crystallinity at those values while the later increase due to slower cooling rates.

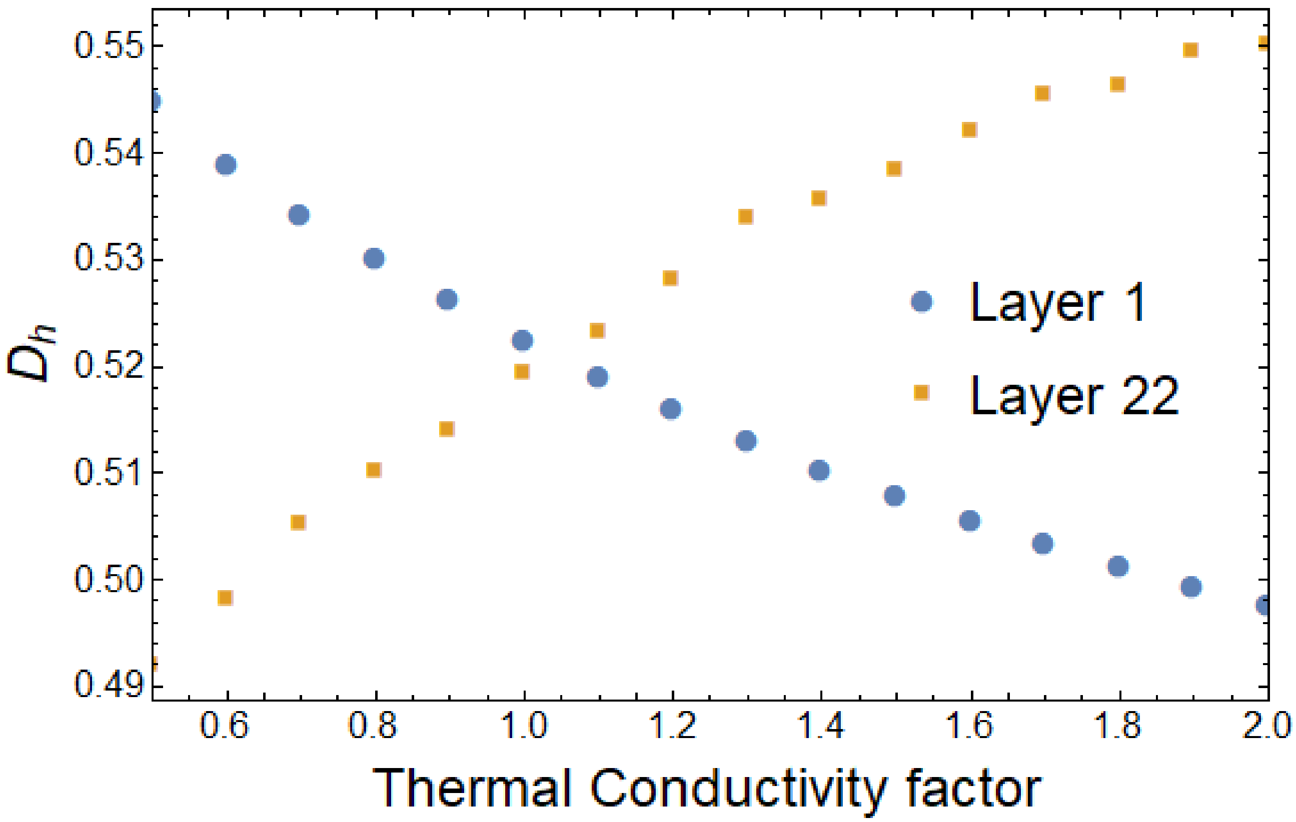

Fig. 4.41: Degree of healing of layers 1 and 22 as a function of thermal conductivity.

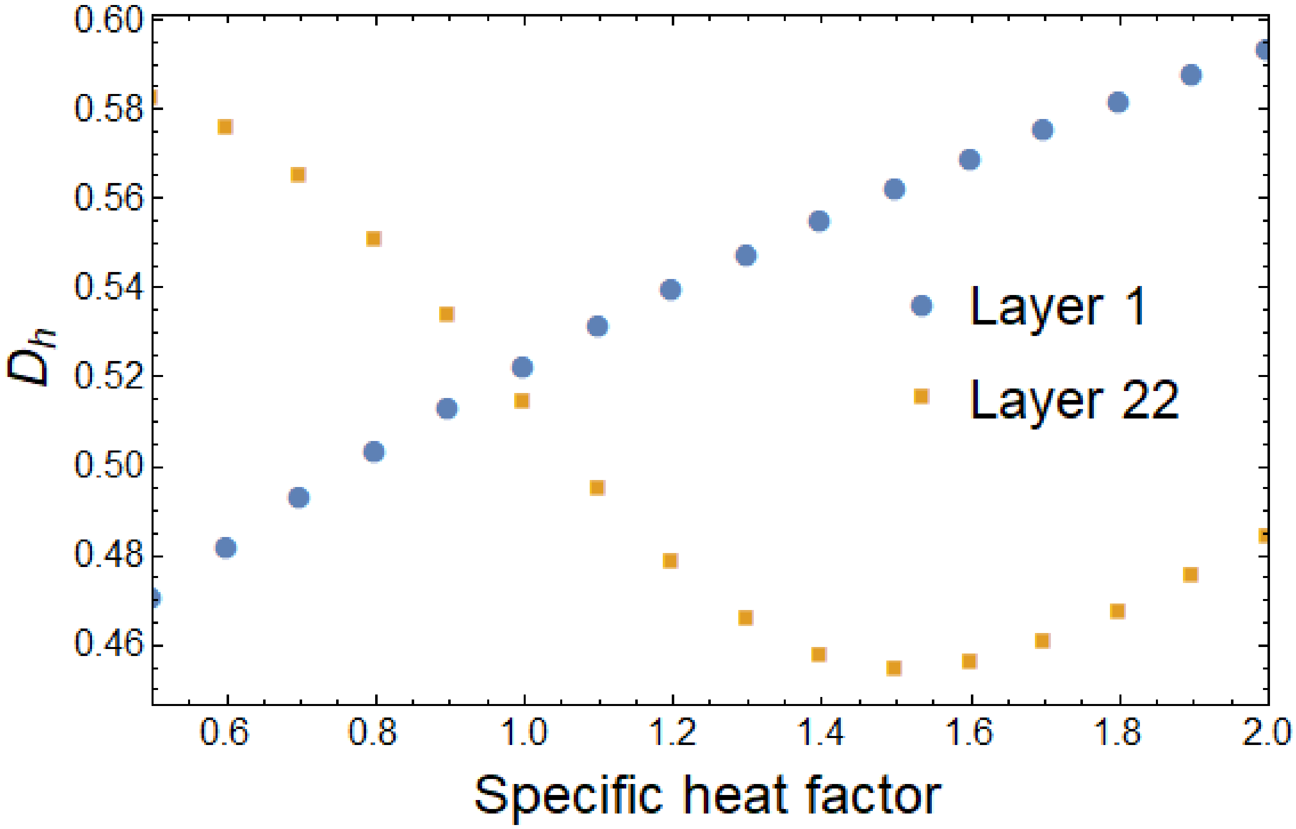

Fig. 4.42: Degree of healing of layers 1 and 22 as a function of specific heat.

Figs. 4.43-45 show the variation of the shear stress with material properties. Thermal conductivity and the ratio of G/E both showed a mostly linear relationship to shear stress, with thermal conductivity decreasing the stress by approximately 3% and G/E increasing the stress by approximately 1%. The most reasonable explanation for the stress reduction at high thermal conductivities is the heat from the bed conducts further into the part reducing thermal contraction. Varying the specific heat showed reduced stress at lower values due to reduced crystallinity and a smaller decrease at high values due to slower cooling. The decrease of each effect from the maximum were 21% and 2% respectively.

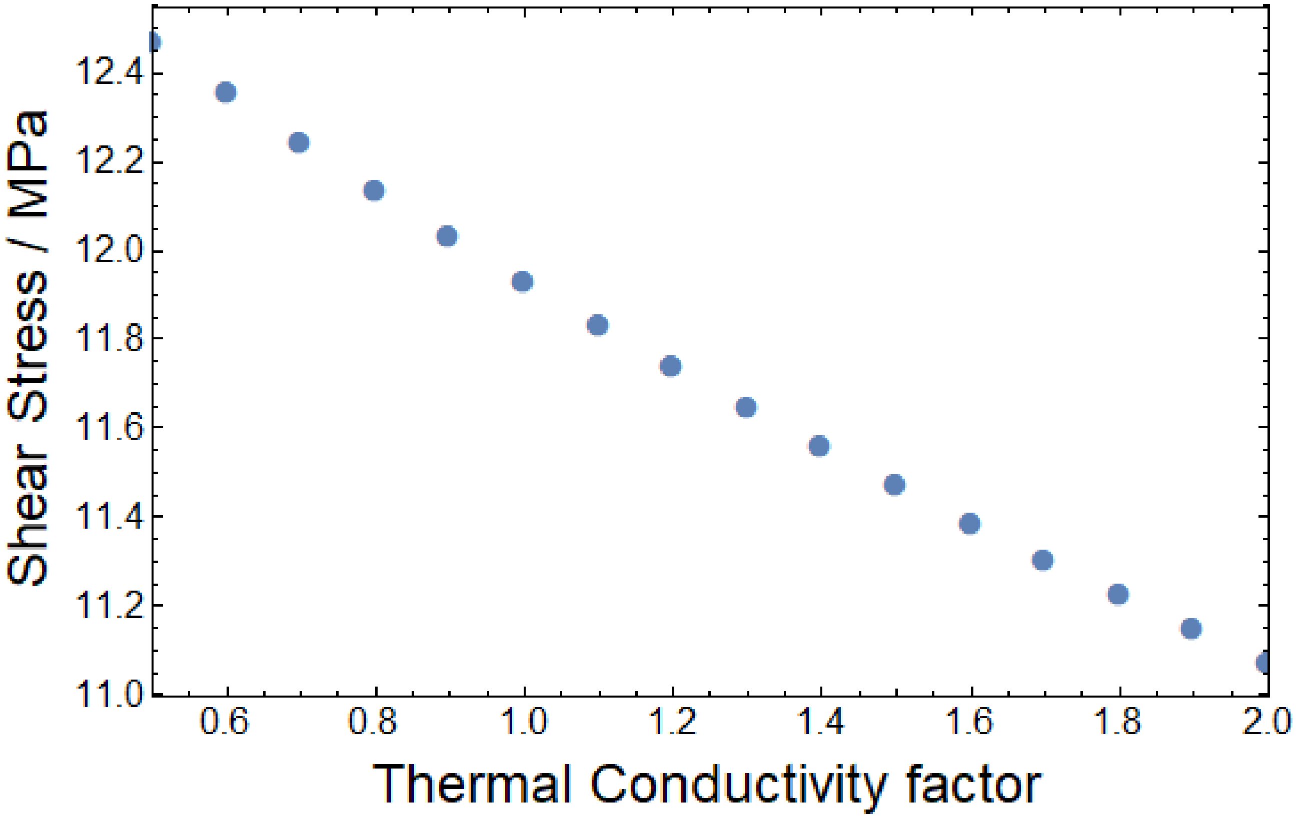

Fig. 4.43: Shear stress at the bottom of layer 1 as a function of thermal conductivity.

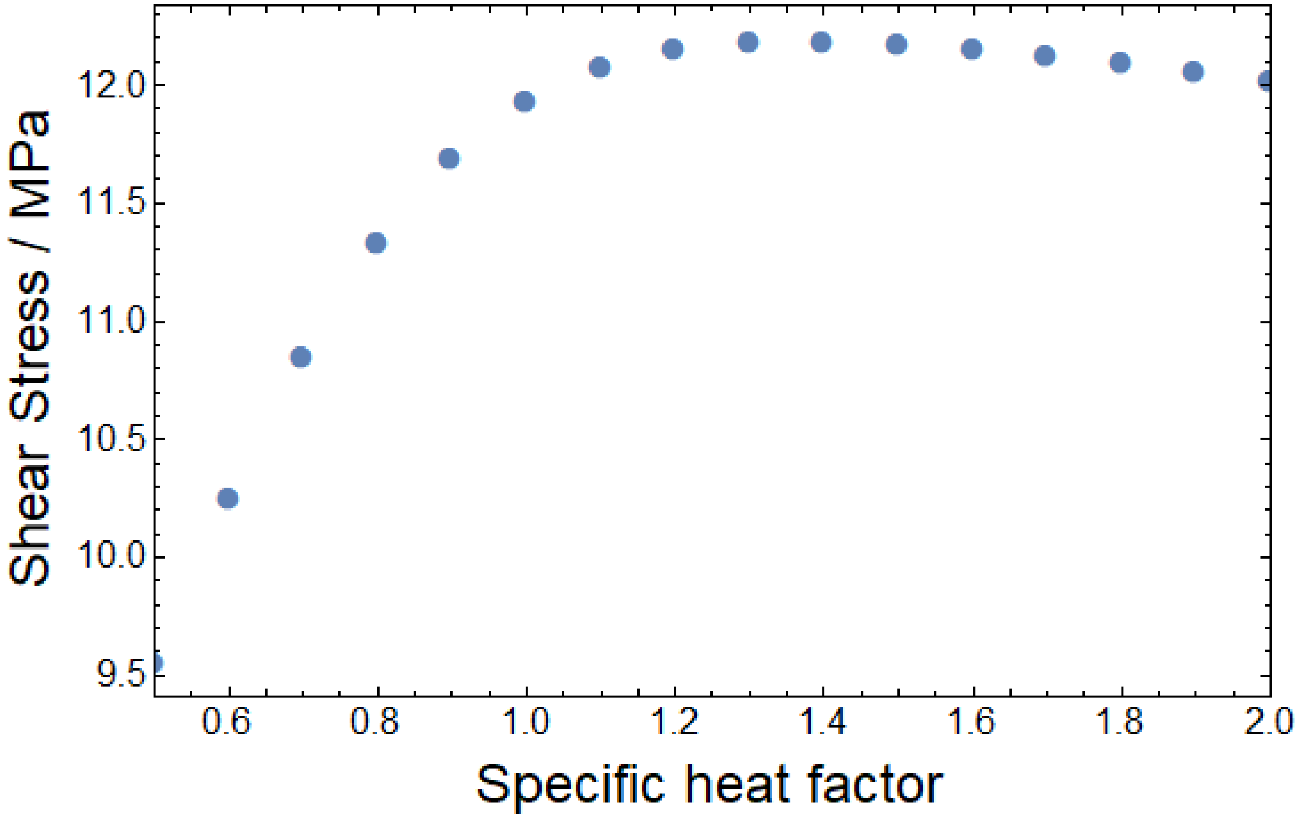

Fig. 4.44: Shear stress at the bottom of layer 1 as a function of specific heat.

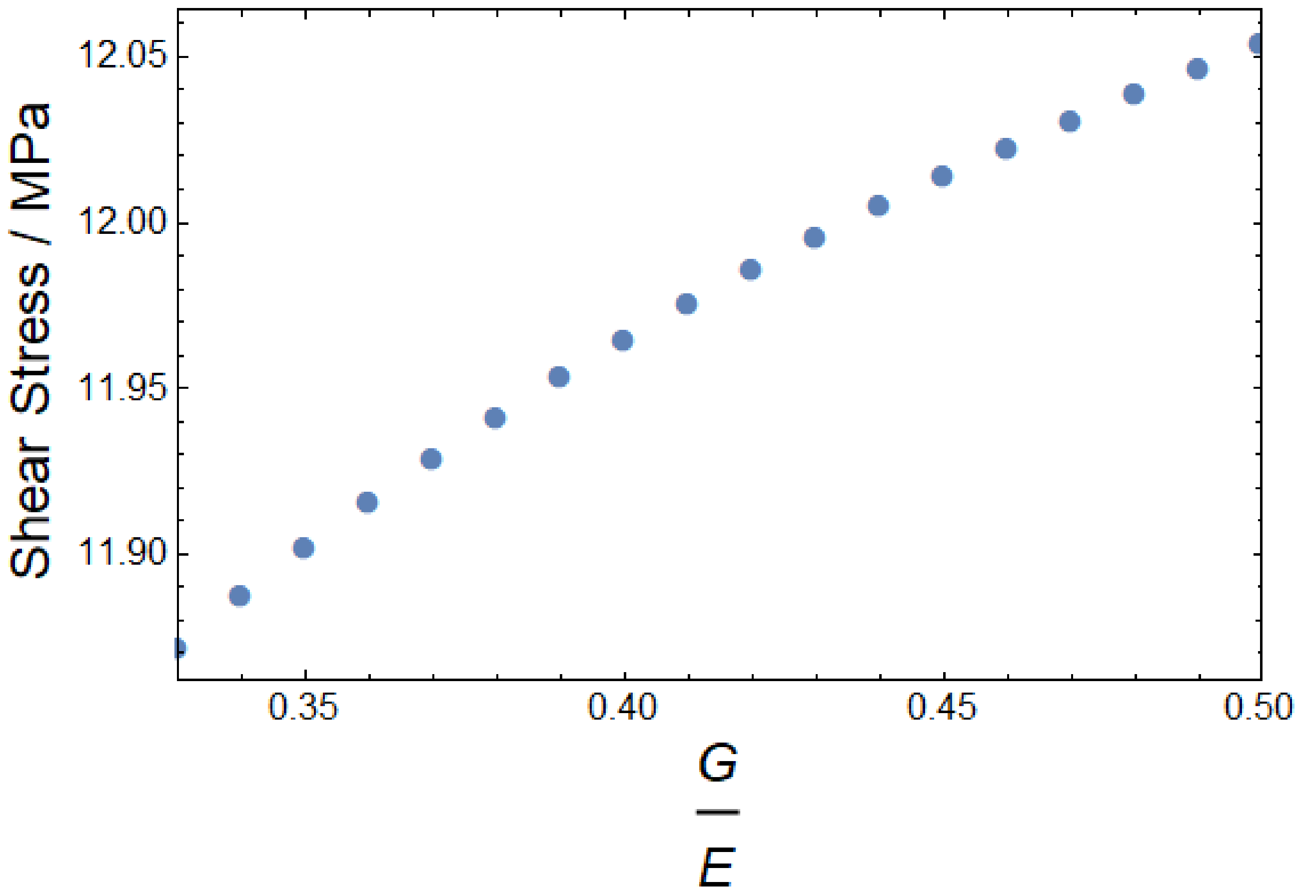

Fig. 4.45: Shear stress at the bottom of layer 1 as a function of G/E.

4.6 Summary and Conclusion

For the first time, a 2D finite difference heat transfer model was used to calculate the cooling behavior of FFF parts with minimal computational requirements. Existing crystallization models were combined to create a nonisothermal crystallization model that can account for any thermal history and multiple crystallization mechanisms. These models were then combined with novel healing models to estimate the bond strength with equally minimal requirements. This model was based on existing healing models for amorphous interfaces but were modified to account for the effects of crystallinity through multiple correction factors. To the authors knowledge, this is the first reported healing model which accounts for crystallinity and has applications for numerous processes besides FFF. A novel stress strain model was used to account for deformation and stress buildup between each deposited road for the first time. The deformation between layers significantly contributes to the total stress within FFF parts so being able to account for this should significantly improve the accuracy of stress predictions. The models showed an ability to account for changes in the properties of a print due to several different processing parameters. In the case of amorphous materials, it was found that long layer times; a low heat transfer coefficient; and high bed, nozzle, and deposition temperatures led to better part properties. Due to the interactions with crystallinity, however, there were exceptions to this. These models further highlighted the importance of further study of the effects of crystallinity on bond formation as there are currently no validated models for this interaction. To this extent, these models need to be validated for several materials to ensure their accuracy for general FFF applications. Furthermore, simulations of more complicated printing history need to be investigated including multiple layer thick walls and inconsistent layer time.

References

[1] S. Z. Cheng, M. Cao, and B. Wunderlich, "Glass transition and melting behavior of poly (oxy-1, 4-phenyleneoxy-1, 4-phenylenecarbonyl-1, 4-phenylene)(PEEK)," *Macromolecules,* vol. 19, no. 7, pp. 1868-1876, 1986.

[2] B. Brenken, E. Barocio, and A. J. F. R. B. Pipes, "Simulation of Semi-Crystalline Composites in the Extrusion Deposition Additive Manufacturing Process," in *Science in the Age of Experience*, Chicago, Il, 2017: Dassault Systemes.

[3] C. N. Velisaris and J. C. Seferis, "Crystallization kinetics of polyetheretherketone (peek) matrices," *Polymer Engineering & Science,* vol. 26, no. 22, pp. 1574-1581, 1986.

[4] A. Galeski and M. Psarski, "Morphology and kinetics of crystallization of polyethylene from chain disentangled melt," *Macromolecular Symposia,* vol. 104, no. 1, pp. 183-190, 1996.

[5] C. Frederix, P. Beauchene, R. Seguela, and J. M. Lefebvre, "Kinetics of the non-isothermal fusion-welding of unlike ethylene copolymers over a wide crystallinity range," *Polymer,* vol. 54, no. 11, pp. 2755-2763, 2013/05/09/ 2013.

[6] F. Yang and R. Pitchumani, "Healing of Thermoplastic Polymers at an Interface under Nonisothermal Conditions," *Macromolecules,* vol. 35, no. 8, pp. 3213-3224, 2002/04/01 2002.

[7] C. McIlroy and P. D. Olmsted, "Deformation of an amorphous polymer during the fused-filament-fabrication method for additive manufacturing," *Journal of Rheology,* vol. 61, no. 2, pp. 379-397, 2017.

[8] N. W. Tschoegl, W. G. Knauss, and I. Emri, "Poisson's ratio in linear viscoelasticity–a critical review," *Mechanics of Time-Dependent Materials,* vol. 6, no. 1, pp. 3-51, 2002.

[9] INTAMSYS. (2017, 10/6/2017). *INTAMSYS launches PEEK 3D Printer*. Available: https://www.intamsys.com/intamsys-launches-peek-3d-printer/

[10] S. F. Costa, F. M. Duarte, and J. A. Covas, "Estimation of filament temperature and adhesion development in fused deposition techniques," *Journal of Materials Processing Technology,* vol. 245, pp. 167-179, 2017/07/01/ 2017.

[11] J. G. Van Alsten, S. R. Lustig, and B. Hsiao, "Polymer Diffusion in Semi-crystalline Polymers. 2. Atactic Polystyrene-d Transport into Atactic and Isotactic Polystyrene," *Macromolecules,* vol. 28, no. 10, pp. 3672-3680, 1995.

[12] S. X. Lu, P. Cebe, and M. Capel, "Thermal stability and thermal expansion studies of PEEK and related polyimides," *Polymer,* vol. 37, no. 14, pp. 2999-3009, 1996.

[13] S. Z. Cheng and B. Wunderlich, "Heat capacities and entropies of liquid, high-melting-point polymers containing phenylene groups (PEEK, PC, and PET)," *Journal of Polymer Science Part B: Polymer Physics,* vol. 24, no. 8, pp. 1755-1765, 1986.

[14] N. Sombatsompop and A. K. Wood, "Measurement of thermal conductivity of polymers using an improved Lee's Disc apparatus," *Polymer Testing,* vol. 16, no. 3, pp. 203-223, 1997/06/01/ 1997.

[15] R. Pitchumani, S. Ranganathan, R. C. Don, J. W. Gillespie, and M. A. Lamontia, "Analysis of transport phenomena governing interfacial bonding and void dynamics during thermoplastic tow-placement," *International Journal of Heat and Mass Transfer,* vol. 39, no. 9, pp. 1883-1897, 1996/06/01/ 1996.

[16] F. O. Sonmez and H. T. Hahn, "Modeling of heat transfer and crystallization in thermoplastic composite tape placement process," *Journal of Thermoplastic Composite Materials,* vol. 10, no. 3, pp. 198-240, 1997.

[17] P. Cebe, "Application of the parallel Avrami Model to crystallization of Poly (Etheretherketone)," *Polymer Engineering & Science,* vol. 28, no. 18, pp. 1192-1197, 1988.

[18] G. Scherillo, M. Petretta, M. Galizia, P. Lamanna, P. Musto, and G. Mensitieri, *Thermodynamics of water sorption in high performance glassy thermoplastic polymers*. 2014, p. 25.

[19] A. Greco and A. Maffezzoli, "Polymer melting and polymer powder sintering by thermal analysis," *Journal of Thermal Analysis & Calorimetry,* Article vol. 72, no. 3, pp. 1167-1174, 2003.

[20] A. D'Amico and A. M. Peterson, "An adaptable FEA simulation of material extrusion additive manufacturing heat transfer in 3D," *Additive Manufacturing,* vol. 21, pp. 422-430, 2018/05/01/ 2018.

[21] Q. Sun, G. Rizvi, C. Bellehumeur, and P. Gu, "Effect of processing conditions on the bonding quality of FDM polymer filaments," *Rapid Prototyping Journal,* vol. 14, no. 2, pp. 72-80, 2008.

Chapter 5: Experimental Validation of FFF Models

This chapter addresses research objective 2 by presenting the initial validation of the models presented in Chapter 4.

5.1 Experimental Procedure

Model validation was done using Ultem 1010 (PEI). Filament was dried for 2 hours at 160 °C prior to printing. 76 x 76 x 25 mm hollow boxes were printed with single road thick walls. Printing was done using a modified Lulzbot printer [1]. Prior to printing, the bed was heated to 60 °C, cleaned, and 4 layers of Elmer's Disappearing Purple Glue Stick were applied to the bed. The chamber was allowed to equilibrate for 10 min at the testing conditions prior to each test. Levels tested were 345 °C and 375 °C for the deposition temperature, 175 °C and 200 °C for the bed temperature, and 15 mm/s and 60 mm/s for the printing speeds respectively.

The stress within the parts was determined by measuring the average degree of warping at the corners of each part. This was done by measuring the height at each corner of the part subtracting it from the total height of the part (25 mm). The average of at least 3 samples were taken for each set of conditions. Degree of healing was determined by measuring the tear strength of each part. 75 x 25 mm rectangular samples were cut from each side of the square boxes using a band saw and a 50 mm cut was made along the middle of the samples using a razor blade, as shown in Fig. 5.1. The samples were then tested according to ASTM standard D1938–14 [2]. The force for crack propagation was determined by averaging the force between the initial peak of the force displacement curve and the peak prior to complete tearing. At least 5 samples were tested for each set of conditions. Additionally, ANOVA analysis was done on the experimental results to assess the significance of each printing parameter.

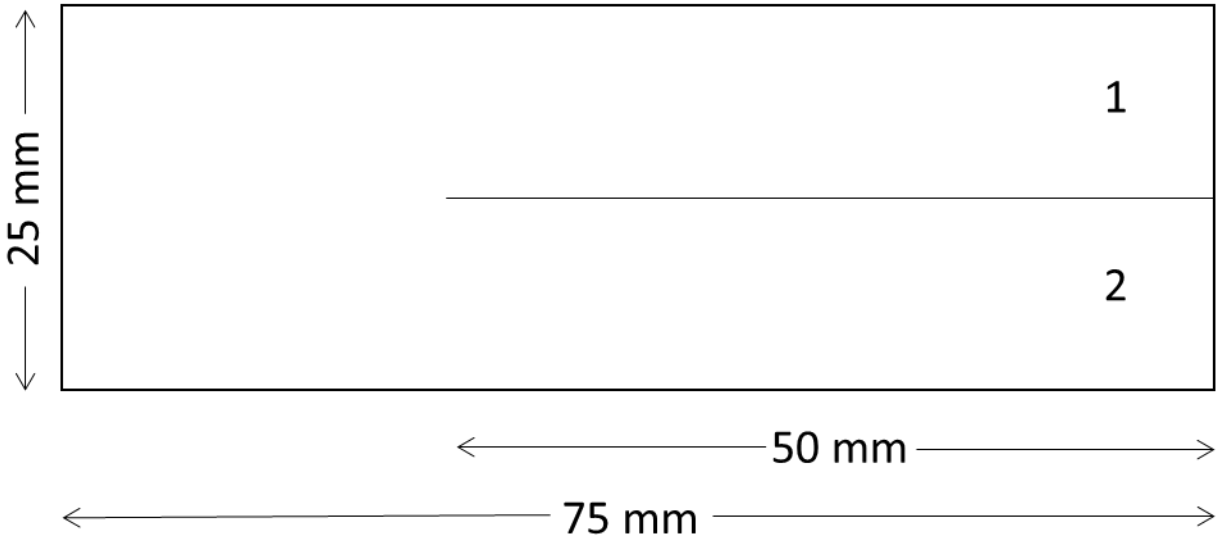

Fig. 5.1: Diagram of tear test samples.

5.2 Experimental Determination of Model Parameters

A baseline for the bulk material properties was obtained by pressing Ultem 1010 into 75 x 75 mm films and cutting samples from them. Multiple samples with thicknesses ranging from 166-434 µm thick were made and tested to determine the tear strength as a function of film thickness; shown in Fig. 5.2. The data did not fit a linear relationship, so a quadratic fit was used (Eq. 5.1).

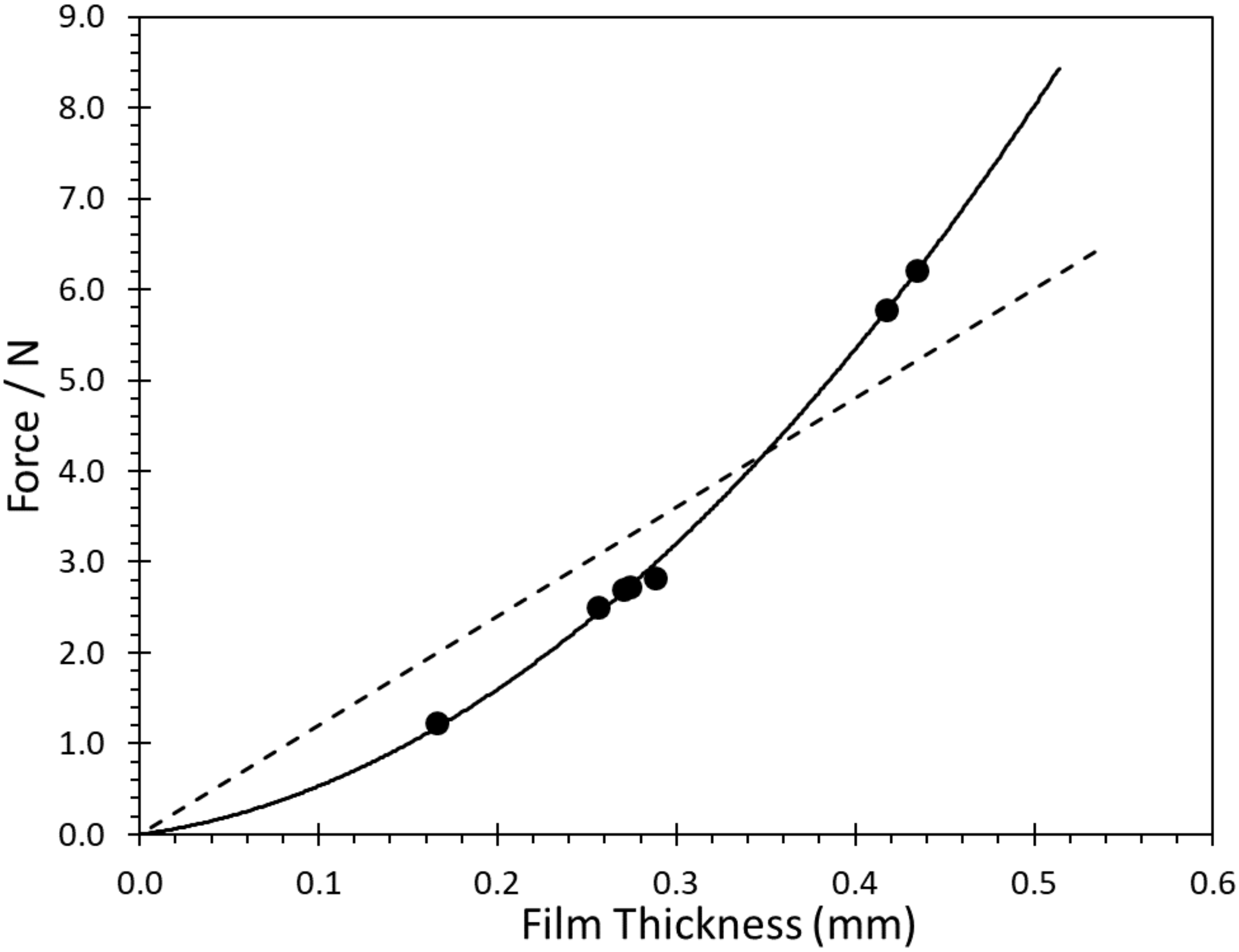

Fig. 5.2: Average tear force of pressed films as a function of film thickness. A linear (dashed) and quadratic (solid) fit are shown.

$$\tau = 26t^2 + 2.9t \tag{5.1}$$

where τ is the weld strength in N and t is the thickness in mm.

To account for differences in weld thickness, the weld thickness of each sample was determined using a Scanning Electron Microscope (SEM). Segments at the end of the tear region approximately 13 mm long were cut from the top part of each sample and coated with a 5 nm thick layer of Au/Pd using a Cressington sputter coater. The average weld thickness was calculated using measurements at the middle and both edges of the sample. An example is shown in Fig. 5.3. Each weld strength was then divided by the baseline weld strength (Eq. 5.1) assuming a thickness equal to the weld thickness to determine the degree of healing.

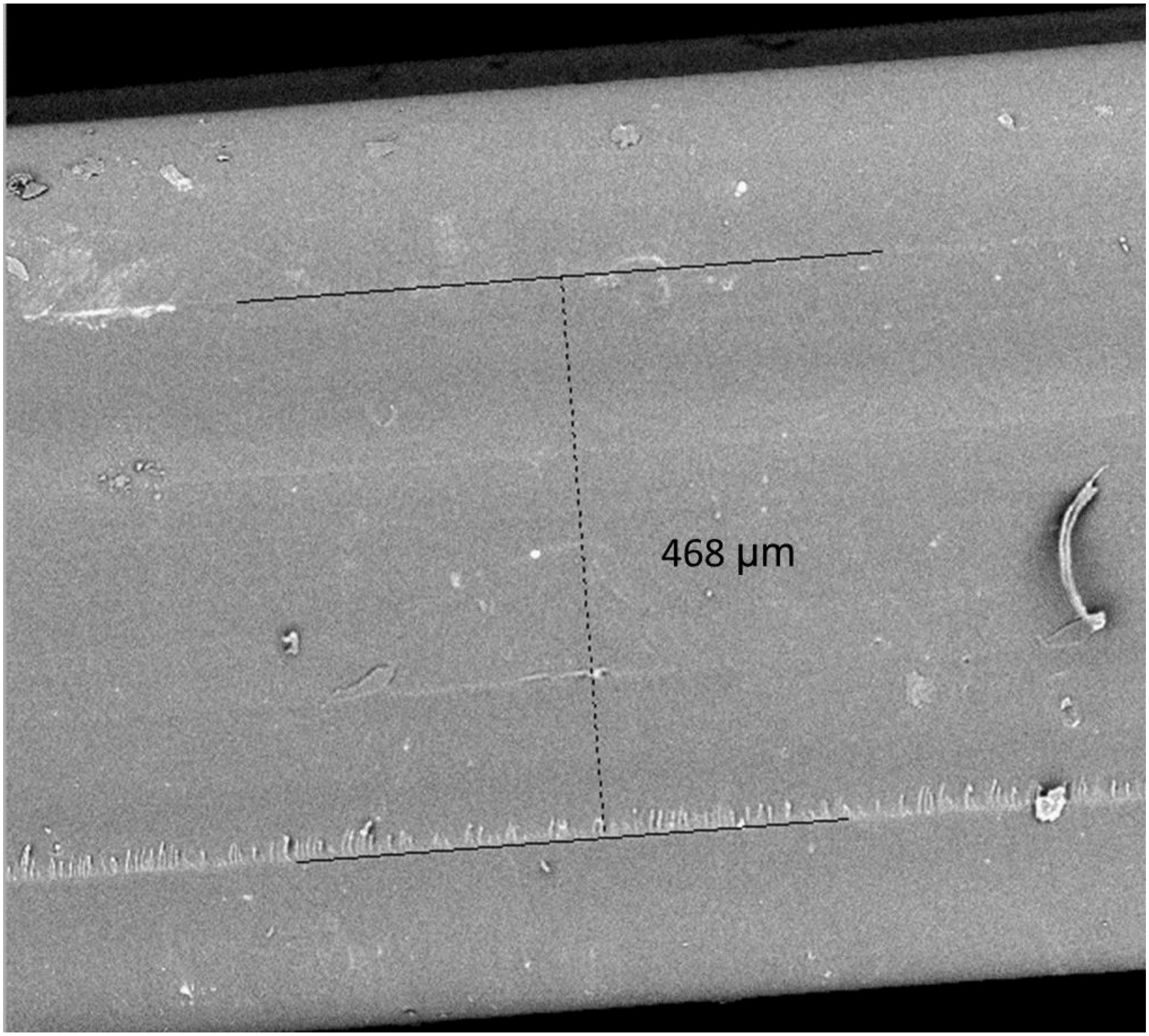

Fig. 5.3: SEM image of interlayer bond after tearing.

To ensure the models match the actual printing conditions as closely as possible, the experimental bed temperature, environment temperature, and heat transfer coefficient were measured experimentally. The bed and air temperatures were determined using Utilitech 60-ft Electrical Tape with an assumed emissivity of 0.95. A section of the bed was coated in one layer of the tape and the bed was allowed to sit for 10 minutes at 175 °C and 200 °C; as shown in Fig. 5.4. The average temperature of an 18 mm square was then taken using a FLIR camera. The bed temperatures were found to be 164.0 and 188.4 °C. The air temperature was found by placing a roll of the tape in the chamber on 20 mm thick fiber glass insulation and allowing the roll to equilibrate for 20 minutes. An 80 mm diameter PEI cylinder was placed around the part to ensure the lamps did not heat the black tape more than they would the PEI. This is also shown in Fig. 5.4. The air temperatures were found to be 97.1 and 100.4 °C for bed temperatures of 175 °C and 200 °C respectively.

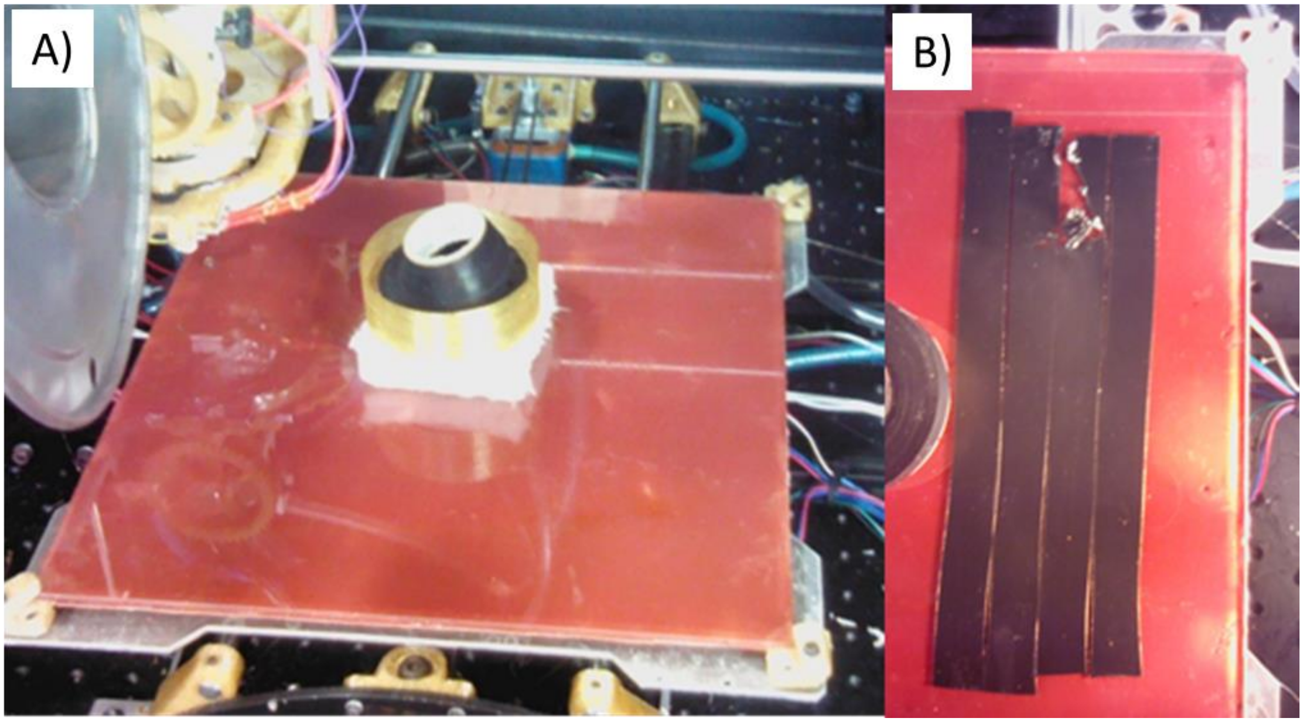

Fig. 5.4: Experimental setup for determination of environment temperature (A) and bed temperature (B) as a function of bed temperature. Values were determined using an IR camera. Emissivity of the tape was assumed to be 0.95.

The emissivity of the PEI was determined by adjusting the value until the temperature of a line of printed material matched the bed temperature and was found to be 0.87. Due to the small layer width, the cooling of individual lines could not be taken from the side. This was shown by the fact that the equilibrium temperature of a single printed line was found to be 150.8 °C when taken from the side but 174.6 °C when taken from above. Since the print head is above the part during printing, an alternative approach was used to determine the heat transfer coefficient.

A 0.7 mm wide PEI part was heated to 200 °C and allowed to equilibrate for 10 minutes. This part was then placed within the printing chamber on 20 mm thick fiber glass insulation and allowed to cool. The temperature profile of the part as it cooled was recorded with an IR camera. The heat transfer coefficient was then adjusted to best match the experimental data with the theoretical cooling, as determined by Eq. 2.13. A value of 29 W/m^{2}K was found and is shown in Fig. 5.5 along with the experimental data. This is comparable to the value of 62 w/m^{2}K found by Costa et al. [3]; especially given that they did not use an enclosed chamber which increases the heat transfer coefficient due to greater air flow.

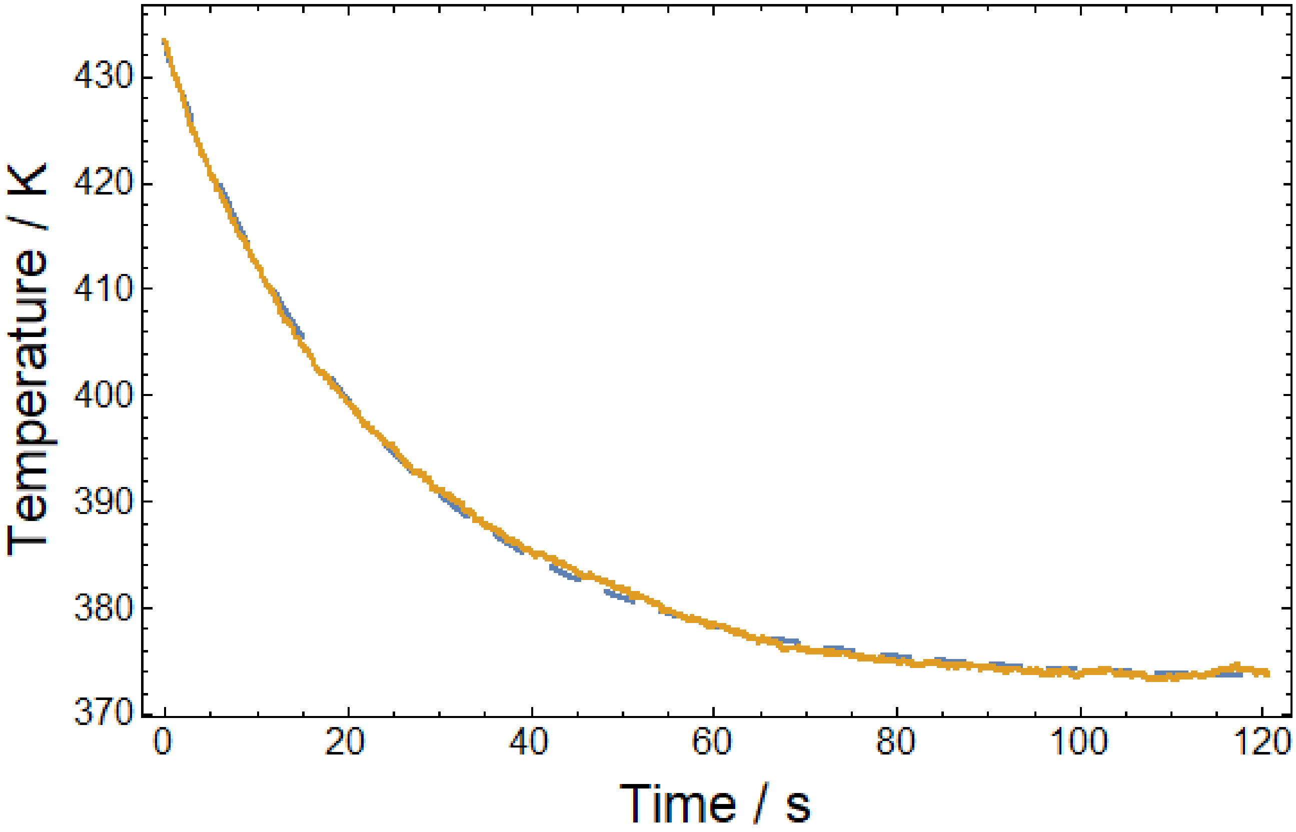

Fig. 5.5: Experimental (solid orange) and theoretical (dashed blue) cooling assuming a heat transfer coefficient of 29 W/m^{2}K.

5.3 Model Parameters

The other model parameters were obtained from literature or based on the capabilities of the printer, and are shown in Tables 5.1-2.

Table 5.1: Printing parameters for PEI simulations.

	Parameter	Symbol	Value
Printing parameters	Width of road	width	0.7 mm
	Height of road	height	0.4 mm
	Number of roads in a layer	rows	1
	Number of layers	layers	24
	Time between printing each layer	t_{layer}	5-20 s
	Air temperature while printing	T_{air}	97.1-100.4 °C
	Temperature of the printing bed	T_{bed}	164.0-188.4 °C
	Temperature of the extruded material	T_{dep}	345-375 °C
	Heat transfer coefficient	h	29 W/m^{2}K
User defined values	Number of elements per road in the x direction	nx	7
	Number of elements per road in the y direction	ny	7
	Factor for determining dt	factor	0.2

Table 5.2: Ultem 1010 properties.

Material Property	Symbol	PEI
Shear modulus	G	1.0 GPa [4]
Young’s modulus	E	2.9 GPa [4]
Thermal expansion coefficient	α	55.8 μm/mK [5]
Density	ρ	1.27 g/cm^3 [5]
Specific heat	cp	$T < 215$°C: 1582 J/(kg*K) $T > 215$°C: 1907 J/(kg*K) [6]
Thermal conductivity	k	0.22 W/(mK) [4]
Activation energy of diffusion	E_a	59.7 kJ mol^{-1} [7]
Reptation time at reference temperature	τ_r^*	0.62 s [7]
Reference temperature	T_{ref}	295 °C [7]
Glass transition temperature	T_g	215°C [6]

5.4 Results and Discussion

Fig. 5.6 shows a representative plot of the force required for tear propagation of the PEI samples. Each line shows a different side of the same part. The large variation in the average tear force shows the significant variation in the tear strength of the specimens even within a single part.

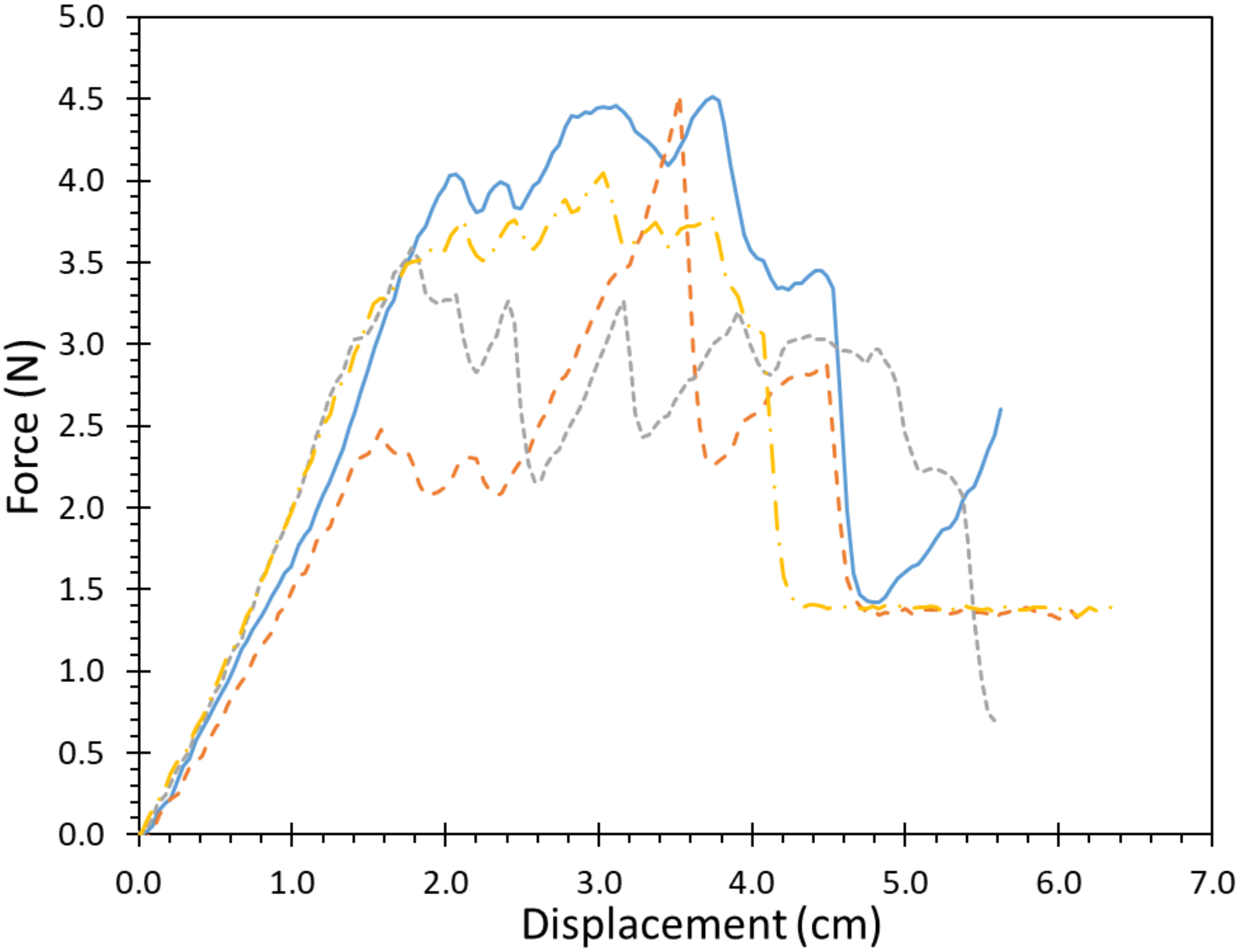

Fig. 5.6: Representative plot of trouser tear test results.

Fig. 5.7 shows the degree of healing of the printed parts as a function of the predicted degree of healing. Overall, the measured degrees of healing were between 15 and 36%; which are within the theoretical range of 0-100% healing. The experimental degree of healing had high deviations which makes determining the significance of each variable difficult. ANOVA analysis showed the deposition temperature had a potential effect on healing with a p-value of 0.07. The predictions showed a small increase in healing with bed temperature while the experiments showed no significant effect (p = 0.55). Printing speed was found to have a significant detrimental effect (p = 0.03) on healing, which is the opposite of the predicted increase. This is likely because heat transfer from the nozzle to the part was not accounted for. As the print speed increased, the nozzle moved from the deposited material quicker shortening the time at which the nozzle could heat the deposited material. Additionally, it is very possible that at the higher print speeds, the temperature of the deposited material is lower due to insufficient heating from the nozzles. Further study needs to be done to quantify the effect of both those phenomena and determine if heat transfer from the nozzle takes place primarily through radiation, convection, or conduction along the filament. The exact degrees of healing are shown in Appendix E. No significant interactions between these parameters were seen.

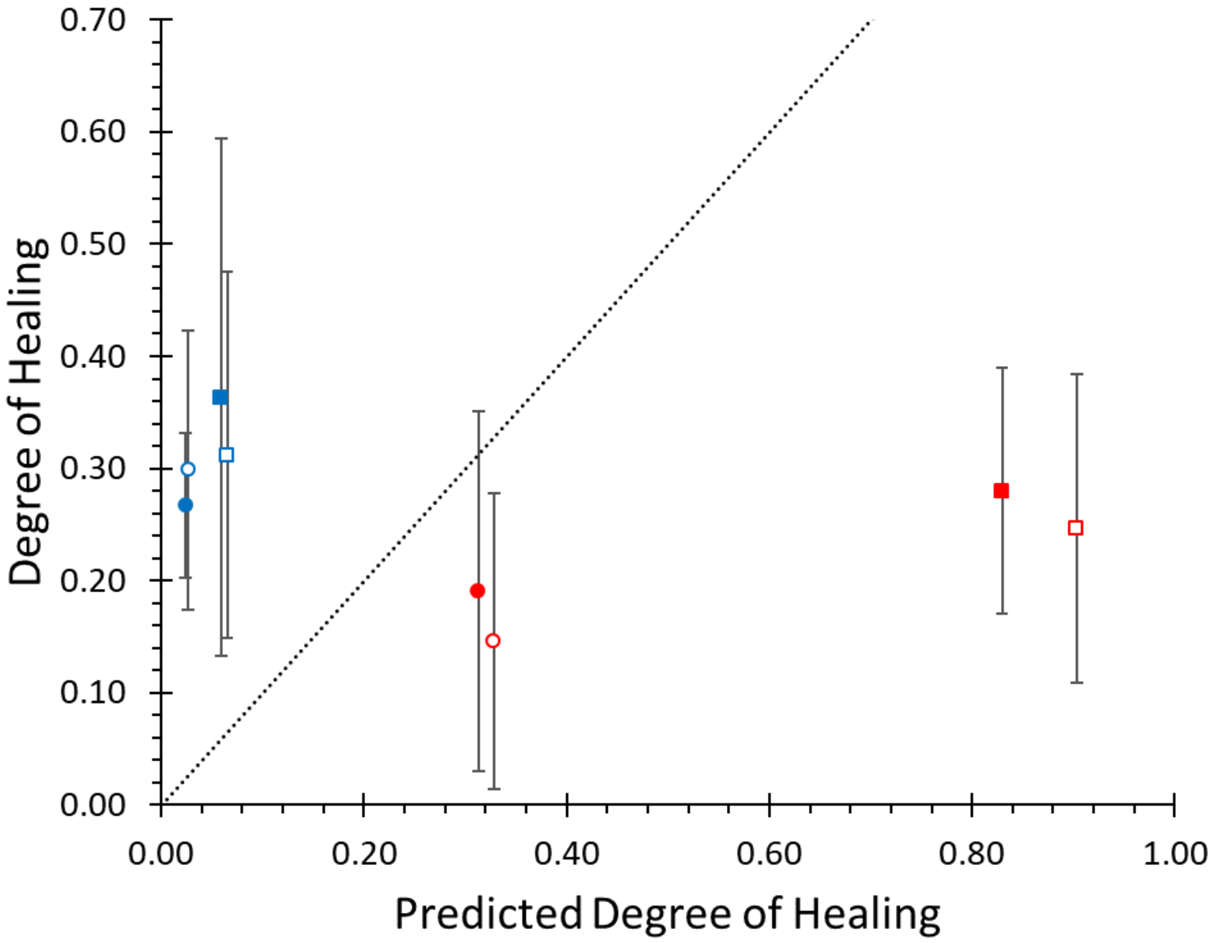

Fig. 5.7: Experimental versus predicted degree of healing. Deposition temperatures were 345°C and (●) 375 °C (■). Bed temperatures were 175 °C (Solid) and 200 °C (Open). Print speeds were 15 mm/s (Blue) and 60 mm/s (Red). Error bars show one standard deviation. Line y = x is shown for comparison.

Fig. 5.8 shows the warpage due to thermal contraction of each set of printing conditions as a function of the predicted stress. The results had high deviations but showed a statistically significant ($p < 0.001$) increase in warpage with stress as expected. Each printing parameter and two factor interaction were found to have a significant effect at the 95% confidence level with the exception of the interaction between deposition temperature and printing speed. We found that part failure occurred at high degrees of warpage (approximately 2.6 mm). This marks the upper limit for the shear stress for this set of printing conditions. The exact predicted stress and warpage values are shown in Appendix E.

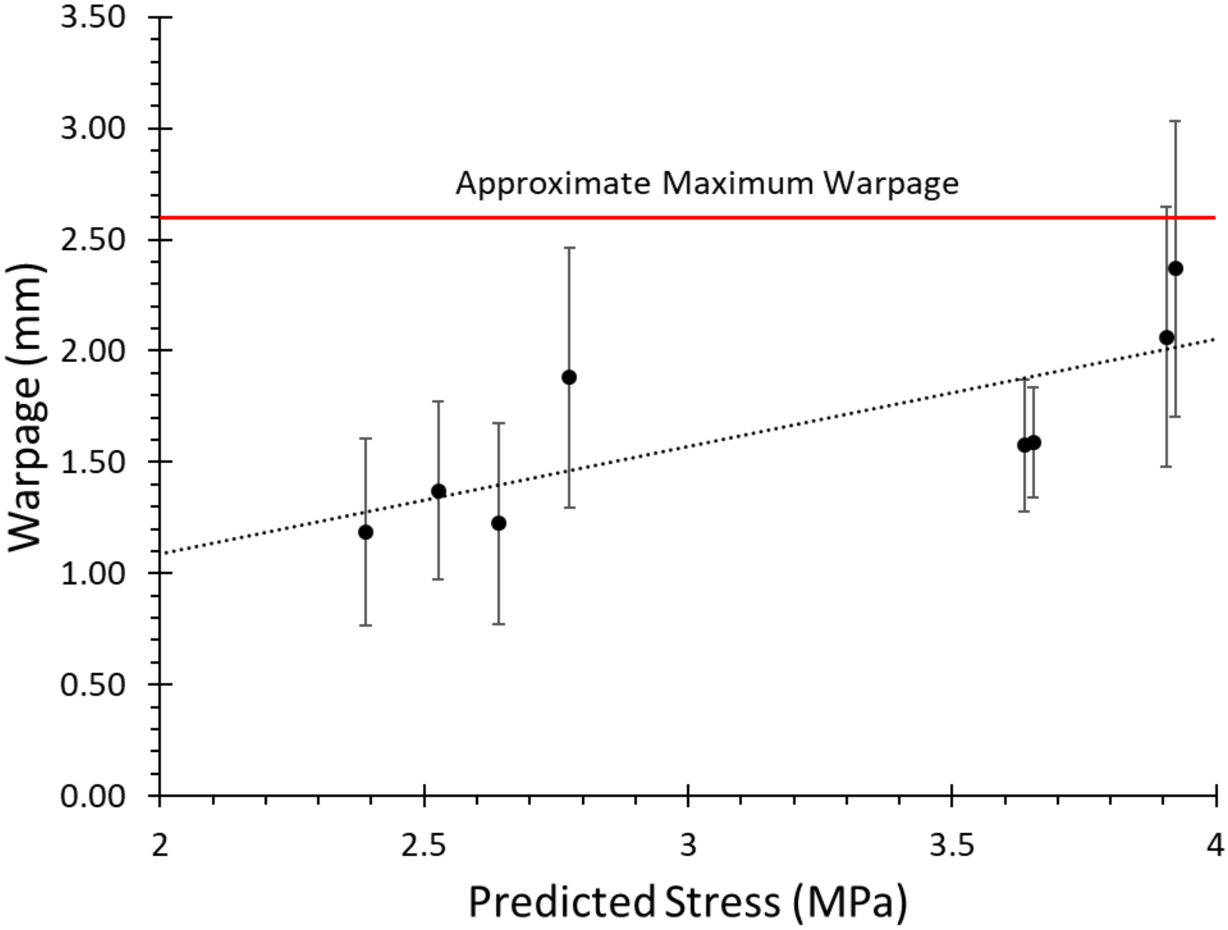

Fig. 5.8: Average warpage at the corners of each part vs predicted shear stress at the bottom of layer 1. Error bars show one standard deviation. A linear fit of the data is included.

5.5 Summary and Conclusion

Experimental validation of the predictions of the properties of FFF prints was conducted. Experimental values of the warpage showed a positive relationship with the predicted shear stress as expected. Experimental measurements of the bond strength were within the theoretical limits of the healing model but did not accurately account for the effects of bed temperature and print speed. Further work will need to be done to determine how the models can be adjusted to better account for these parameters. Additionally, a mechanical model should be developed to determine the predicted relationship between residual shear stress and warpage for better comparison with experimental results. More materials will need to be tested to demonstrate the validity of the models for a wide variety of materials. This includes testing of semi-crystalline materials to verify the accuracy of the crystallinity models and their effect on diffusion and residual stress.

References

[1] J. M. Gardner, C. J. Stelter, E. A. Yashin, and E. J. Siochi, "High Temperature Thermoplastic Additive Manufacturing Using Low-Cost, Open-Source Hardware," 2016.

[2] A. D1938-14. (2014). *Standard Test Method for Tear-Propagation Resistance (Trouser Tear) of Plastic Film and Thin Sheeting by a Single-Tear Method*. Available: https://www.astm.org/Standards/D1938.htm

[3] S. F. Costa, F. M. Duarte, and J. A. Covas, "Estimation of filament temperature and adhesion development in fused deposition techniques," *Journal of Materials Processing Technology,* vol. 245, pp. 167-179, 2017/07/01/ 2017.

[4] AZoM. (2003, 5/23/2018). *Supplier Data - Polyetherimide (PEI) (Goodfellow)*. Available: https://www.azom.com/article.aspx?ArticleID=1883

[5] Sabic. (2003, 7/26/2018). *ULTEM 1010 Americas: COMMERCIAL*.

[6] F. Biddlestone, A. Goodwin, J. Hay, and G. Mouledous, "The relaxation spectrum and physical ageing of polyetherimide," *Polymer,* vol. 32, no. 17, pp. 3119-3125, 1991.

[7] L. Bastien and J. Gillespie, "A non-isothermal healing model for strength and toughness of fusion bonded joints of amorphous thermoplastics," *Polymer Engineering & Science,* vol. 31, no. 24, pp. 1720-1730, 1991.

Chapter 6: Recommendations

1) In-situ measurements should be taken over a wide variety of printing conditions to quantify the effect of each on the nozzle temperature and pressure. Additionally, tests should be performed using a variety of materials to further validate the system and theoretical pressure models. In particular, composite materials should be run to explore the relationship between pressure and particle alignment.
2) From the experimental model validation, it is apparent that faster printing had a detrimental effect on the part strength rather than the predicted increase. This will need to be further studied to determine if this is due to a reduction in heat transfer from the nozzle, a change in road geometry, or some other unknown cause. This effect will then need to be added to the models.
3) For this work, only the simplest case of a single road wall was simulated and tested. Further work needs to be done on more complicated part geometries; especially multiwalled builds. This will validate the effectiveness of the models for real parts and enable more detailed investigations into how part geometry impacts mechanical properties. Similarly, experimental validation was only done on amorphous materials and will need to be performed on crystalline materials once the models are further improved.
4) While a positive relationship was observed between the shear stress and warpage, this interaction should be further modeled to determine the theoretical relationship between them. This would entail determining the minimum shear stress required for delamination and the expected amount of bending for a given shear stress. Results of these models could then be used to assess the accuracy of the residual stress model.

5) While stress accumulation above the Tg should be minimal, it is possible that the fast cooling time would prevent stress relaxation above the Tg and lead to additional stress in the part. As such, further study should be done to verify the amount of stress relaxation that occurs during cooling.

6) The effects of crystallinity on healing have not been fully explored and can likely be greatly improved. The most critical need is for thorough experiments on the effect of crystallinity of either side of the interface on the rate of healing; especially at temperatures relevant to the FFF process. These tests would need to be done for symmetric and asymmetric crystalline interfaces as well as at isothermal and nonisothermal conditions. These tests could be done using welding experiments to simplify the process.

7) While a single value was used for the bed temperature, environment temperature, and heat transfer coefficient, these values vary with both location and time. Currently, no standard method exists to measure or accurately model these fluctuations. As such, standardized methods to quantify these fluctuations are needed and the results should be factored into the models to calculate their effect on part properties.

8) Similarly, while a constant road width and height was used, the printing parameters greatly affect these dimensions. Several researchers are currently investigating this topic through current models are still computationally intensive. As these models are simplified, the road geometry’s dependence on the printing parameters should be included.

Appendix

Appendix A: Nozzle Design

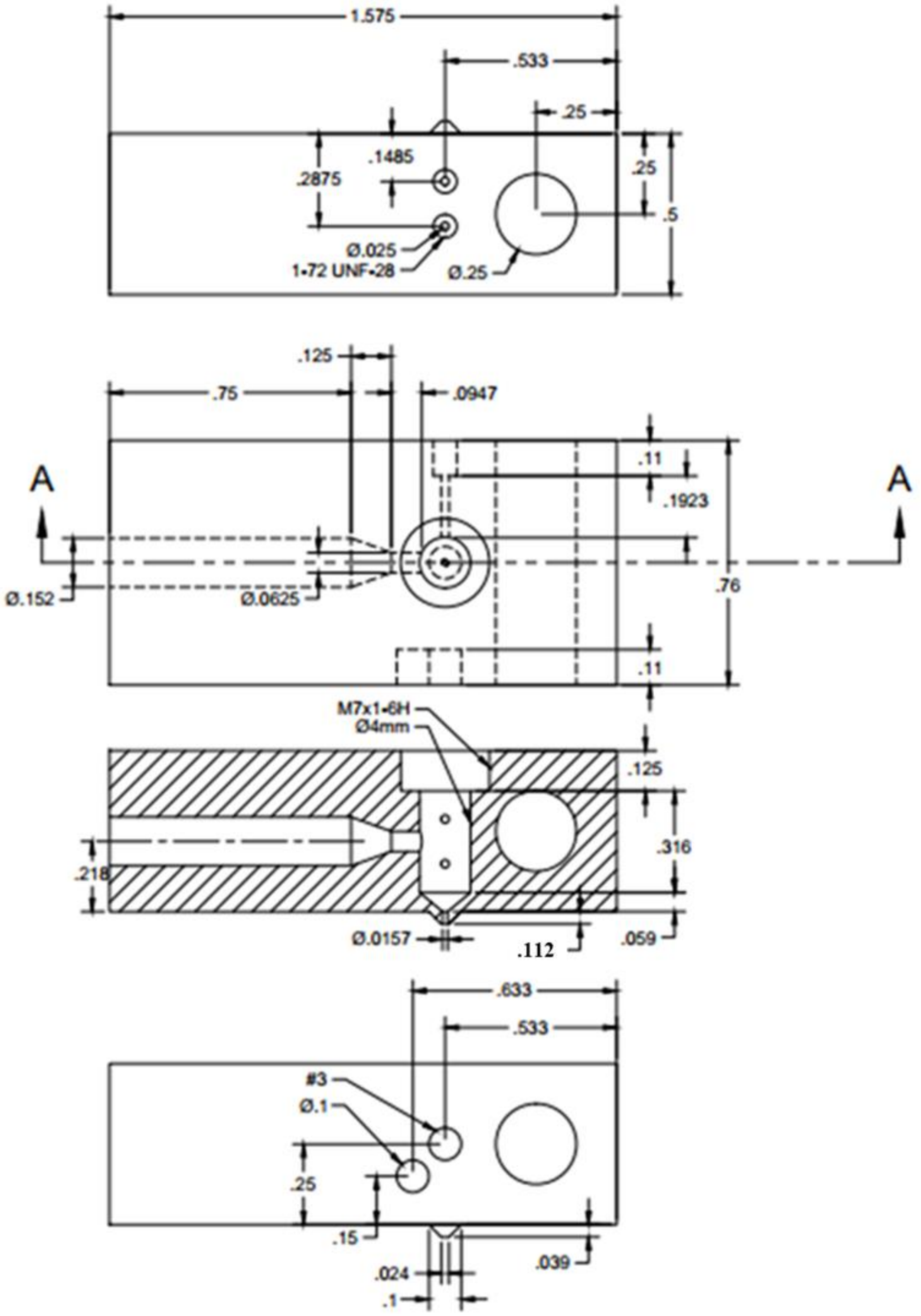

Fig. 0.1: Dimensions of modified nozzles. Dimensions are in in unless otherwise specified.

Appendix B: Nozzle Design Calculations

Several calculations were performed to ensure proper integration of the sensors into the nozzle and minimize the impact of these sensors on the printing process. The difference between the coefficients of thermal expansion of the nozzle and sensors were calculated to ensure that heating the nozzle would not cause any significant stresses. The difference was less than 0.1%.

Additionally, we calculated the pressure loss due to friction around the sensors at 230 °C and 0.75 mm^3/s using stokes law, shown in Eq. 3.7 [1]:

$$Drag\ Force = \frac{6\pi\mu d_{sensor}}{2v} \qquad (0.1)$$

When this force is divided by the cross-sectional area of the sensor, the drag caused by the thermocouple was 1.1 kPa; which is negligible compared to the expected pressure drop of 1100-2700 kPa [2-4]. Furthermore, the impact of the thermocouple on filament flow at varying length scales was estimated to ensure that the transducer is far enough from the thermocouple that the flow has returned to steady state. To do this, the change in the velocity at the center of the nozzle was found for two cylinders with the same length but a difference in volume equal to the volume of the thermocouple. By changing the length of the cylinder, the significance of the sensor could be estimated at varying length scales. The graph of the results is displayed in Fig. 7.2. The data in Fig. 7.2 suggests that within 1mm of the sensor, the flow velocity has significantly recovered with approximately 0.26% difference from the steady state velocity.

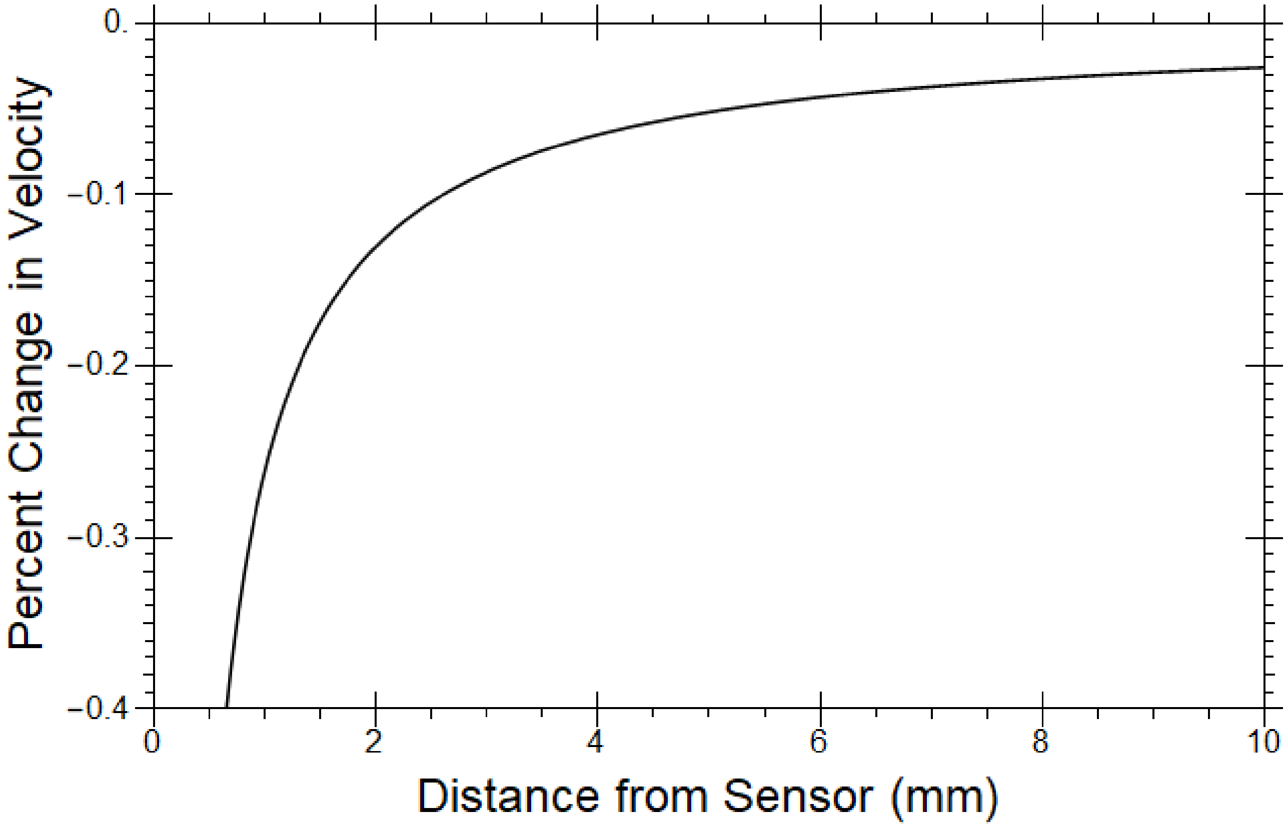

Fig. 0.2: Percent change in flow velocity at center of flow versus length from volume element.

These theoretical calculations were experimentally validated by comparing the flow rates of each nozzle configuration. Fig. 7.3 provides the average flow rate for each nozzle configuration after adjusting the PID and motor tightness. The addition of the thermocouple reduced the flow rate by less than 2% and the addition of the transducer reduced the flow rate by approximately 6%. The decrease in flow rate seen in the transducer nozzle is likely due to a decrease in the tightness of the motor as suggested by the higher deviations. Overall, the change in flow rate is small compared to the deviations of the measurements, strongly supporting the theoretical calculations.

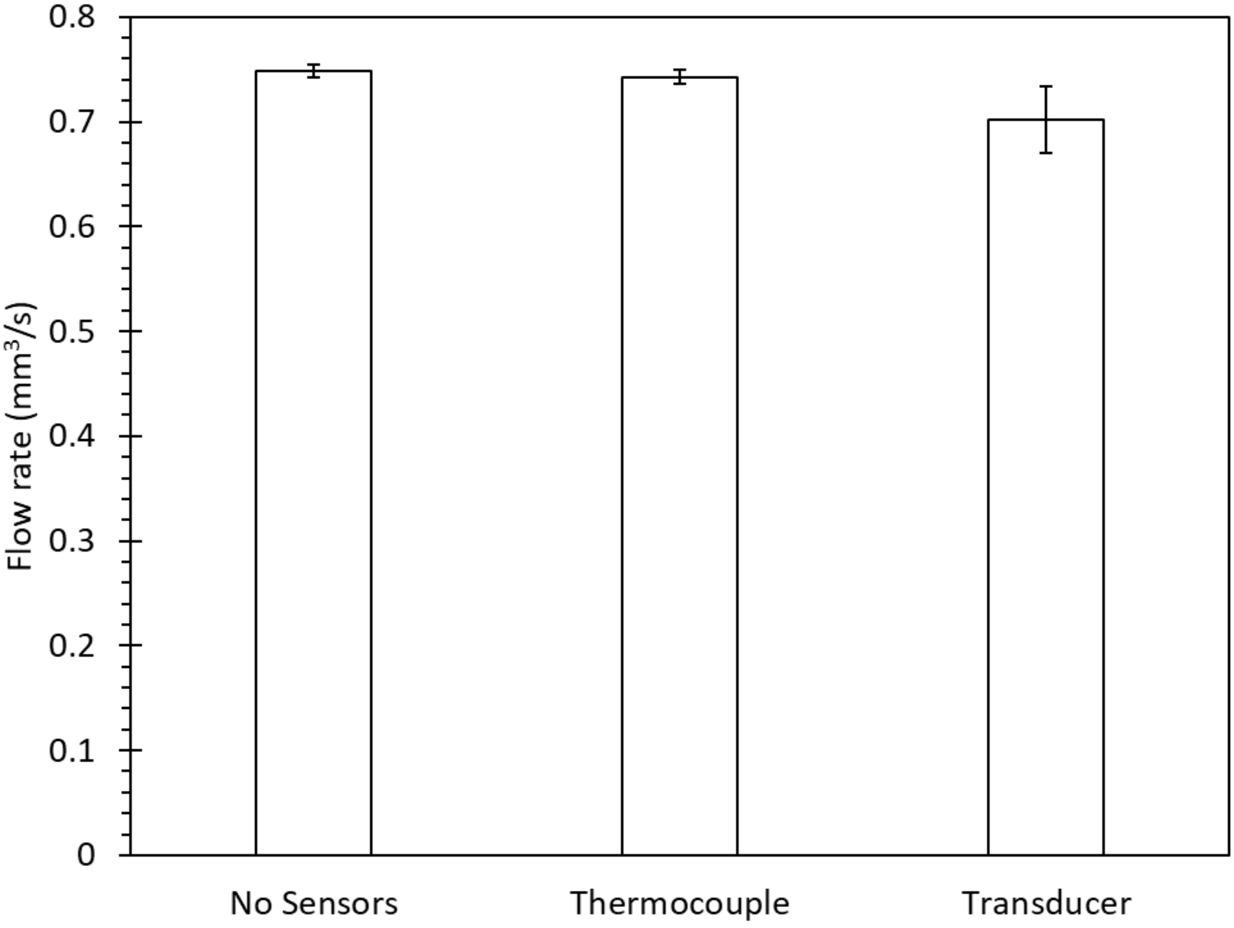

Fig. 0.3: Flow rate for each nozzle configuration during extrusion.

Appendix C: Two-dimensional Assumption Validation

For the assumption that $\frac{\partial^2 T}{\partial z^2} = 0$ to be valid, it must be sufficiently smaller than $\frac{\partial^2 T}{\partial y^2}$ such that it will not significantly change the cooling behavior. The same equations can be used for heat transport in the z direction as those used for the x and y directions (Eq. 4.48).

$$\frac{dT}{dt}_{front/back} = \frac{K}{\mu\rho}\left(\frac{T_r + T_l - 2T}{dz^2}\right) \qquad 0.2$$

The temperature of the adjacent elements can be estimated from the temperature profile of 2D simulations. Under the assumption of little change in heat flow in the z direction, the temperature profile of elements at the same x and y coordinates will be the same except offset by some amount of time due to the change in deposition time. This offset can be calculated for any given printing speed using the z dimension of the elements (dz). For simpler comparison dz will equal dy. Using a very slow print speed of 4 mm/s and a dz of 0.05 mm the change in time would be 0.0125 s. To further simplify comparison with the simulation data, we will express time in terms of steps where one step is dt (0.0048 s) so the change in time is 1.0475 steps. Using interpolation of the temperature profile, the change in temperature due to heat flow in the z direction in layer 1 at position 4 was calculated; as this location had the highest cooling rate. Aside from a small instability upon printing of the next layer and the initial print, the change in temperature was found to be insignificant. For the first few times steps of the print, the temperature would decrease slightly slower but considering that these timesteps are when the temperature change is the most extreme the difference is negligible. Furthermore, increasing the print speed would reduce this effect making it even more negligible. Therefore, the neglection of heat flow in the z direction is a reasonable assumption.

Appendix D: Effect of Crystallinity on Interlayer Healing

While the results of Boiko et al. [5] and Agawa et al.[6] were limited and not intended to determine the degree of healing as a function of crystallinity, they can nonetheless be used to assess the feasibility of the interlayer healing model. Two conditions have been studied, symmetric interfaces and nonsymmetric. Fig. 7.4 shows the shear strength of symmetric crystalline interfaces relative to amorphous interfaces as a function of crystallinity while Fig. 7.5 shows the relative strength of asymmetric (amorphous/crystalline) interfaces. As can be seen, the model predictions work well for the symmetric data of PET but significantly underpredicted the strength of the asymmetric PET and the symmetric PEEK. Also included is a plot of $(1-X_{c1})$ $(1-X_{c2})$ which proved to be a good fit to the asymmetric PET and the symmetric PEEK data. Both tests were done at relatively low temperatures, so it is possible that the amorphous regions of the crystalline samples were able to diffuse without restriction as the diffusion length would have been very small. This would explain the fit of the ($1-X_{c1}$) ($1-X_{c2}$) relationship which equals the model in the case of $X_{vc\infty}$ = 1 or the amorphous regions are entirely unrestricted. This will need to be further tested especially at higher temperatures to verify the applicability of this data to FFF conditions.

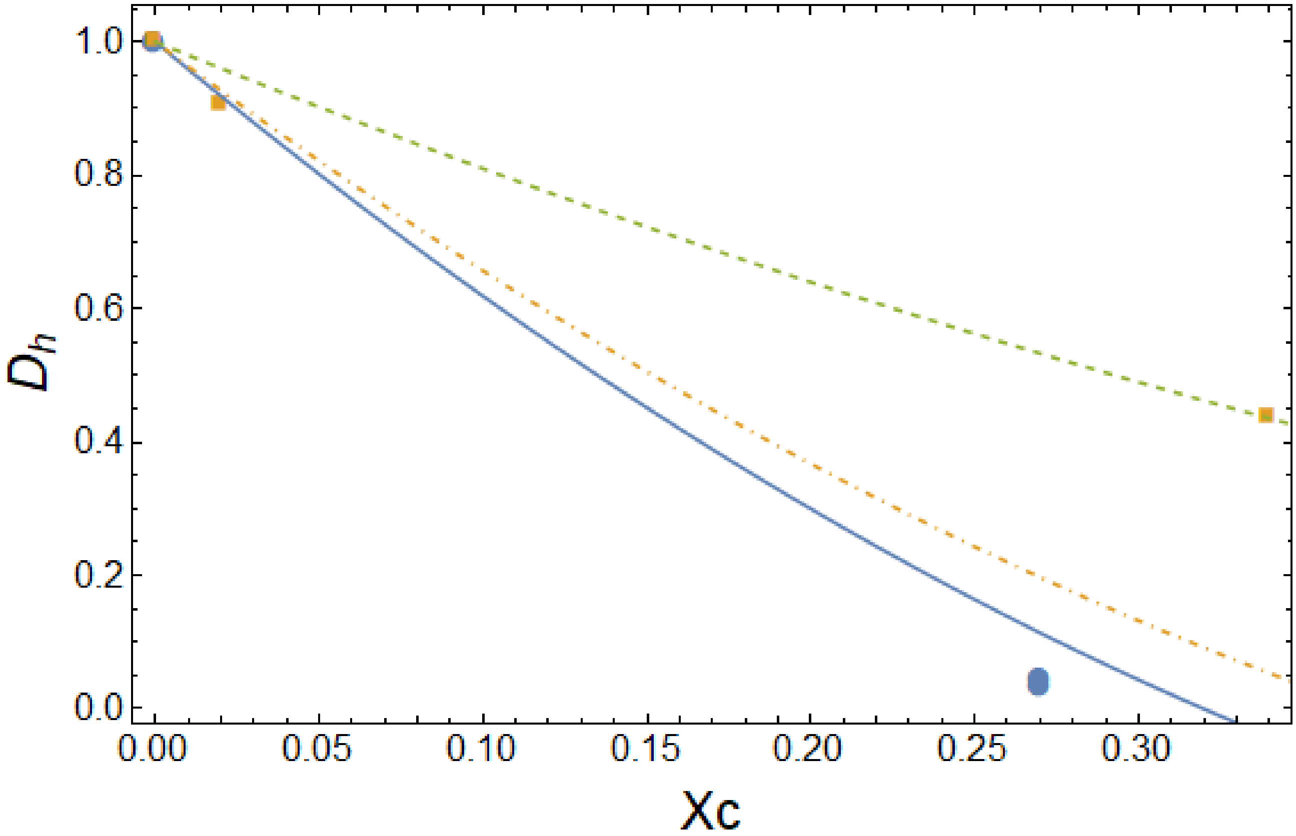

Fig. 0.4: Degree of healing of symmetric crystalline interfaces versus crystallinity. Data on PET collected by Boiko et al. [5] is shown with blue circles and data on PEEK collected by Agawa et al. [6] is shown with orange squares. The predictions from the diffusion model are included using $X_{vc\infty}$ values of 0.32 [7] and 0.37 [8] for PET (-) and PEEK (-●-) respectively. The plot of ($1-X_{c1}$) ($1-X_{c2}$) is also included (- -).

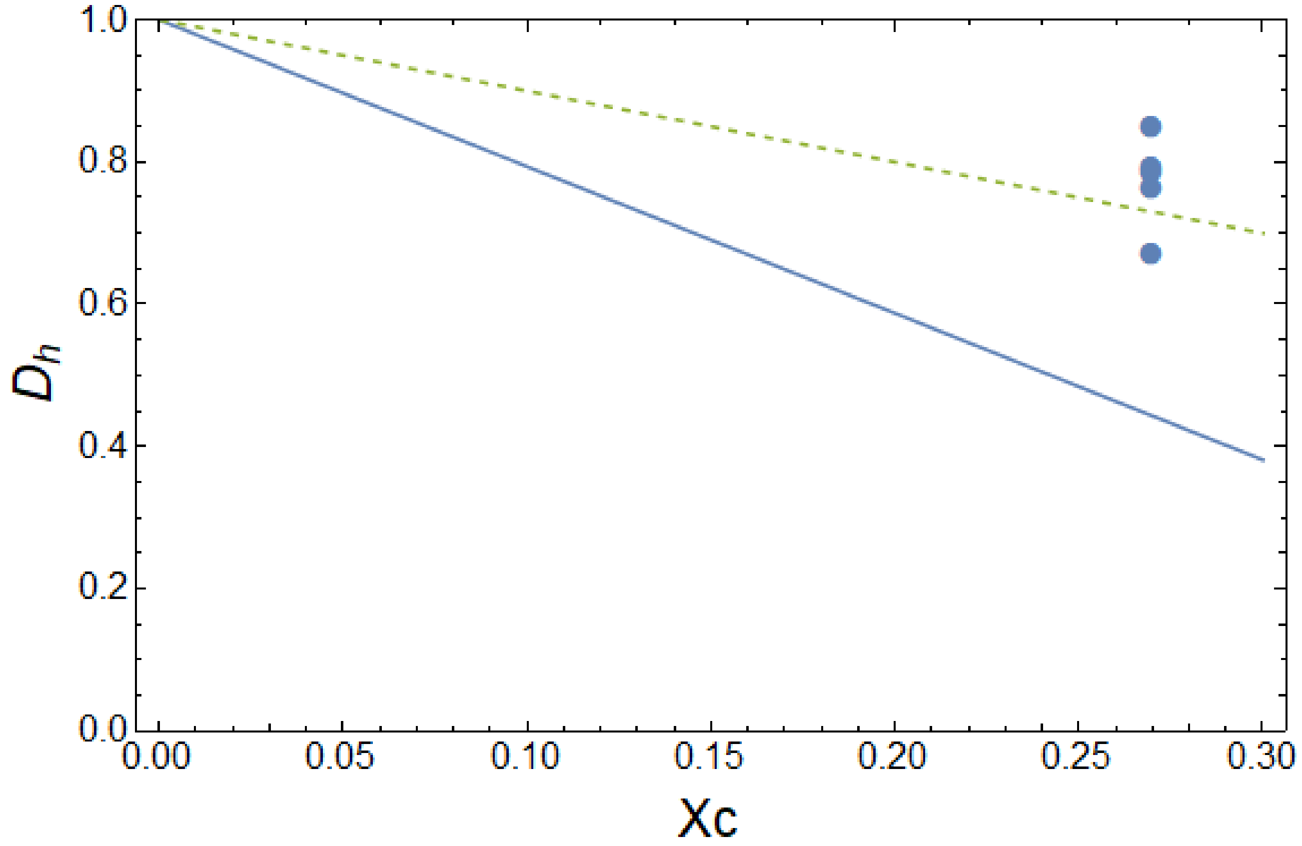

Fig. 0.5: Degree of healing of amorphous/crystalline PET interfaces versus crystallinity. Data was collected by Boiko et al. [5] The predictions from the diffusion model is included using $X_{vc\infty}$ values of 0.32 [7] for PET (-). The plot of (1-Xc1)(1-Xc2) is also included (- -).

Appendix E: Table of Experimental and Predicted Part Properties

Table 0.1: Predicted and experimental shear stress and degree of healing for each set of printing parameters.

Nozzle Temperature (°C)	Bed Temperature (°C)	Layer Time (s)	Predicted Shear Stress (MPa)	Warpage (mm)	Predicted Degree of Healing	Experimental Degree of Healing
345	175	15	3.9	2.37	0.02	0.27
345	175	60	2.8	1.88	0.31	0.19
345	200	15	3.7	1.59	0.03	0.30
345	200	60	2.5	1.37	0.33	0.15
375	175	15	3.9	2.06	0.06	0.36
375	175	60	2.6	1.22	0.83	0.28
375	200	15	3.6	1.57	0.07	0.31
375	200	60	2.4	1.19	0.90	0.25

References

[1] Y. L. Qi Zhang, Randy Switt, Sameer Matta, Dr. Chang-Yu Wu. (3/30/18). *Aerosol Transport – Inertia*. Available: https://aerosol.ees.ufl.edu/credits.html

[2] H. S. Ramanath, C. K. Chua, K. F. Leong, and K. D. Shah, "Melt flow behaviour of poly-ε-caprolactone in fused deposition modelling," *Journal of Materials Science: Materials in Medicine,* journal article vol. 19, no. 7, pp. 2541-2550, 2007.

[3] N. Mostafa, H. M. Syed, S. Igor, and G. Andrew, "A study of melt flow analysis of an ABS-Iron composite in fused deposition modelling process," *Tsinghua Science and Technology,* vol. 14, no. S1, pp. 29-37, 2009.

[4] B. N. Turner, R. Strong, and S. A. Gold, "A review of melt extrusion additive manufacturing processes: I. Process design and modeling," *Rapid Prototyping Journal,* vol. 20, no. 3, pp. 192-204, 2014.

[5] Y. M. Boiko, G. Guérin, V. A. Marikhin, and R. E. Prud'homme, "Healing of interfaces of amorphous and semi-crystalline poly(ethylene terephthalate) in the vicinity of the glass transition temperature," *Polymer,* vol. 42, no. 21, pp. 8695-8702, 2001/10/01/ 2001.

[6] F. Awaja and S. Zhang, "Self-bonding of PEEK for active medical implants applications," *Journal of Adhesion Science and Technology,* vol. 29, no. 15, pp. 1593-1606, 2015.

[7] T. Chan and A. Isayev, "Quiescent polymer crystallization: modelling and measurements," *Polymer Engineering & Science,* vol. 34, no. 6, pp. 461-471, 1994.

[8] C. N. Velisaris and J. C. Seferis, "Crystallization kinetics of polyetheretherketone (peek) matrices," *Polymer Engineering & Science,* vol. 26, no. 22, pp. 1574-1581, 1986.